Refractive Index Distribution of Single Cell and Bacterium Usingan Optical Diffraction Tomography System

Yang Patricia Liu

UNIVERSITÉ PARIS-EST

Ecole Doctorale

Mathématiques, Sciences de l'Information et de la Communication (MSTIC)

THÈSE

pour obtenir le grade de

Docteur de l'Université Paris-Est

Spécialité : Electronique, Optronique et Systèmes

Présentée et soutenue publiquement par

Patricia Yang LIU

Le 14 Novembre 2016

Etude de propriétés biophysiques de cellules bactériennes par réfractométrie optofluidique

Refractive Index Distribution of Single Cell and Bacterium Using an Optical Diffraction Tomography System

Jury

Yong CHEN, Professeur, ENS-Paris (Rapporteur)
Isabelle LEDOUX-RAK, Professeur, ENS-Cachan (Rapporteur, Présidente du jury)
Yamin LEPRINCE-WANG, Professeur, ESYCOM, UPEM (Directrice de thèse)
Tarik BOUROUINA, Professeur, ESYCOM, ESIEE Paris (Directeur de thèse)
Wee SER, Associat Professor, NTU, Singapore (Co-Encadrant de thèse)
Lip Ket CHIN, Research Fellow, NTU, Singapore (Examinateur)

Devote to my dearest grandmother, Tian Bin,

who had always been there for me in every stage of my life.

ACKNOWLEDGMENTS

I would like to express my profound gratefulness to my supervisors: Professor Yamin Leprince-Wang, Professor Wee Ser and Professor Tarik Bourouina, who offered me invaluable guidance and encouragement throughout the entire PhD candidature period not only in the academic research area but also in my personal development.

I would like to express my heartfelt appreciation to Professor Kuan Wang, visiting professor in Nanyang Environmental & Water Research Institute, Nanyang Technological University (NTU), Singapore, for his strong support, guidance and training. I would also like to express my deep appreciation to Dr Lip Ket Chin, School of EEE, NTU, Singapore, for consistent advices and training. I would like to express special thanks to my team partner Mr Chao-Mao Chieh and Mr Hongfu Chen for their great contribution in development of the optical diffraction tomography system. I would like to thank Dr Lei Lei and Dr Sha Xiong for their advices and in-depth discussion when we are working on water quality inspection.

I would also like to thank Mr Haitao Zhao, Mr Qinghua Song and Mr Yuzhi Shi for their friendship and help in many aspects. I would like to express my deep appreciation to Dr Ran Ding for his consistent encouragements, support and great help. I would like to thank Miss Eileen Ng for her warm friendship. Their accompany makes my campus life more joyful and colorful.

I am lucky to be a member of such a knowledgeable, experienced and enthusiasm research team. This environment speeds up my learning and research process greatly.

Lastly but greatly, I would also like to express my sincere appreciation to ESIEE-Paris, Université Paris-Est and VALENS Center, School of EEE, Nanyang Technological University for supporting of this PhD project and providing me with excellent platforms and working environments.

Summary

Refractive index is one of the most important physical parameters governing the light-reaction behaviors of cells and other microorganisms. Its significance lies in the fact that it can be used to determine or correlate with other important biophysical parameters such as dry mass, wet mass, elasticity and used to study dynamic cell activities. The main objective of this research is to study and measure refractive indices of single bacterium and cell as well as cell's response to microenvironment stimulations.

The experimental study includes two approaches. One approach is the development of an integrated microfluidic immersion refractometer platform to measure the biophysical parameters (the size, shape and refractive index) of three bacteria species, namely *Echerichia coli, Shigella flexneri* and *Vibrio cholera*. These parameters could provide biophysical signatures of the targeted bacteria. The significance of this research work lies in establishing a rapid, label-free and low-cost system for detection of minute amount of harmful waterborne bacteria in drinking water.

The other experimental approach is to obtain the 3D refractive index mapping of a single cell with the focus on studying intracellular lipid droplets and their response towards microenvironmental stimulation using an optical diffraction tomographic system integrated with fluorescence imaging. The investigation of refractive indices of cellular lipid droplets initiates a novel approach for deeper understanding of lipid droplets and their critical roles in metabolism and related diseases.

Résumé

L'indice de réfraction est l'un des paramètres physiques les plus importants qui régissent les comportements à la lumière de cellules et d'autres micro-organismes. Son importance réside dans le fait qu'il peut être utilisé pour déterminer ou mettre en corrélation avec d'autres paramètres biophysiques importants de la cellule tels que la masse sèche, la masse humide, l'élasticité et est utilisé pour étudier les activités dynamiques cellulaires. L'objectif principal de cette recherche est d'étudier et de mesurer les indices de réfraction de bactérie et de cellules unitaires ainsi que leur réponse à des stimulations micro-environnementales.

Notre étude expérimentale comprend deux approches. La première consiste en une plate-forme microfluidique intégrée de réfractomètrie par immersion pour mesurer les paramètres biophysiques (taille, forme et indice de réfraction) de trois espèces de bactéries, à savoir *Escherichia coli*, *Shigella flexneri* et *Vibrio cholerae*. Ces paramètres peuvent fournir des signatures biophysiques des bactéries ciblées. L'importance de ce travail de recherche réside dans l'établissement d'un système rapide, sans label fluorescent et à bas coût pour la détection d'une quantité infime de bactéries nocives dans l'eau potable.

L'autre approche consiste à obtenir la distribution de l'indice de réfraction au sein d'une seule cellule avec l'accent mis sur l'étude des gouttelettes lipidiques intracellulaires ainsi que leur réponse à une stimulation micro-environnementale. A cet effet, nous avons recouru à un système de diffraction tomographique optique intégré avec imagerie par fluorescence. Ce type d'étude sur l'indice de réfraction de gouttelettes lipidiques cellulaires initie une nouvelle approche pour une meilleure compréhension des gouttelettes lipidiques et leurs rôles essentiels dans le métabolisme cellulaire.

Contents

Nomenclature

$A(x, y)$	Background intensity of an interference fringe pattern
$B(x, y)$	Intensity modulation of an interference fringe pattern
C	Mass density of the protein
c	Velocity of light propagating in vacuum
I(x, y)	Intensity of the coherent addition of the reference and object beams
i	Frame index of a stack of images
M_{dry}	Dry mass
M_{water}	Water mass
M_{cell}	Total mass of a cell
N	Total number of a stack of image frames
n	Refractive index of a substance
n_{bac}	Refractive index of the bacterium
n_0	Refractive index of liquid/culture medium

Nomenclature

OPD	Optical path difference
ODT	Optical diffraction tomography
t_{bac}	Thickness of the bacterium
V	Cell volume
v	Velocity of light propagating in a specific medium
ψ	The phase difference between the reference and object beams
α	Specific refraction increment of a protein or intracellular constituent
δ_i	One step of phase shift step in phase shifting interferometry
$\varphi(x, y)$	Angular phase difference distribution of an interference pattern
Ur	Complex amplitude field of the reference beam
u_r	Constant amplitude of the complex field of the reference beam
Uo	Complex amplitude field of the object beam
$u_o(x, y)$	Amplitude of the object beam
ρ	Mass density of a cell
ρ_0	Density of water

List of Figures

List of Figures

Chapter 1 Introduction

Biophysical properties of cell are the important linkages between biology and physics, which can be used to analyse and understand the pattern of intracellular organelles and the dynamic of the cell life [1]. Due to recent advancements in MEMS and microfluidic technology, detections of cell biophysical properties with portable, real-time and low cost platforms have had rapid developments, which allow quick and more accurate characterization of cell properties such as its refractive index. On the other hand, owing to rapid innovations in microscopic technologies, remarkable improvements in speed, sensitivity and resolution of photonic recording media and optical components, full-field intracellular and intercellular microscopic imaging and refractive index measurements become feasible, crucial and also fruitful.

1.1 Motivation

This PhD research work is motivated by the potential significance of biophysical properties of cells and their strong ties with numerous cellular functions and dynamic processes. Many biophysical models and theoretical ideologies are developed to achieve in-depth comprehension and investigation into cell biophysical properties, such as electrical, thermal and optical properties as well as patterns of cell life.

A single cell is an electrified system, where there is electrical conductivity, generating electromotive forces and possessing impedance, while the cell membrane can act as an insulator. These properties are useful in studying activities of cell growth in cell culture and brain activity via neural networks in electrical synapse propagation. The mechanical properties of cells involve deformation, mechanical signal transduction and elasticity that allow cells to survive in the physiological environment along with other mechanical forces occurring within and outside of cells. When light propagates through cells, the optical properties, namely, contrast, scattering and absorbance are attributed to their intracellular mass distribution and optical density variation, as well as the cell thickness. Based on understanding of these biophysical properties of cells, we can gain deeper

understanding on how they build biophysical profiles and react towards environmental changes. This comprehensive knowledge would enable us to unveil significant correlation between biophysical properties of cells and severe diseases and therefore to provide great insight for disease models and their unimpeded rapid development, as well as early stage detection and diagnosis of diseases.

The rapid achievements and insights in biology and life sciences in the last century can be attributed to rapid development of modern microscopy combined with fluorescence imaging. Microscopic imaging has always been a dominant tool in biological and biomedical sciences and applications, while fluorescence labeling and specific immune conjugation play significant roles in specific investigations of intracellular and intercellular mechanism and identification of different organelles inside microorganisms. Nevertheless, there have been tremendous efforts on investigation and development of label-free detection and visualization of microorganisms by various optical microscopic methodologies.

One of the most important physical property governing the image quality and light-reaction behaviors of cells and other microorganisms is the refractive index. It can also be used to determine or correlate with other important biophysical parameters such as dry mass, wet mass, elasticity, as well as cell metabolic activities such as infection and different stages of the cell cycle. Significant changes in protein or fatty acid composition can also be detected by changes of the refractive index.

Such changes could be related to cell abnormality and dysfunction, revealing the intrinsic dynamics in cells and other microorganisms. As most governing equations/biophysical models in related research areas have refractive index as a parameter, without knowing the value of it, a biophysical model or quantitative analysis is hardly complete.

In initial studies and measurements of refractive indices of cells in 1950s, scientists treated the cell as a whole to have one average refractive index value. Barer [2] developed immersion refractometry to measure refractive index of a group of cells using phase contrast microscopy. The refractive index of the extracellular medium was adjusted from low to high while the brightness of cell under microscope would change from dark to bright. At a specific point when refractive index of the medium and the cell are matched, the cell will be invisible in the medium. However, restrictions of the technology at that time include the absence of precise control for smooth variation of the medium's refractive index, and the lack of non-contact cell trapping. These limitations can be overcome by using microfluidic technology, which provides microfluidic manipulations for cell delivery and mixing, as well as smooth variation of refractive index of the medium. With better stability and accuracy, measurements of single cell and integration of other functionalities such as cell culture and drug delivery becomes highly feasible.

On the other hand, alongside the intensive developments of submicron microscopic technologies, scientists are also interested in studying the refractive index distributions of intracellular organelles and the dynamic changes among different cell types, including healthy and dysfunctional ones. One of critical applications is the study of cellular lipid droplets which have generated strong interests in recent years as researchers identify their importance in many metabolic pathways and contribution to several modern-time diseases. There is still much unknown about lipid droplets and various effects they may have on cellular pathways and numerous tissues. Hence it is imperative to learn more about the refractive index of lipid droplets and their reactions towards external stimulations such as increasing fatty acids concentration.

With such huge demands for advanced sub-micron inspection technologies, and the availability of innovative laser sources and high sensitivity CCD, CMOS photodetectors, 2D and 3D full-field imaging and quantitative refractive index mapping technologies have been developed rapidly. With corresponding unwrapping/reconstruction algorithms, refractive index mapping for transparent cells is achieved by quantitative phase imaging (QPI) [3, 4], diffraction phase imaging [5] and optical diffraction tomography (ODT) [6, 7], which is also referred as digital holographic tomography. Technologies employing refractive index as the contrast source for imaging and monitoring of cells and other microbes are still in their early stage, considering the vast and highly complicated

bio-organisms, their growing nature and their behaviors in modern industrialized environments. There would be ample space for visualization, timely monitoring and in-depth investigations with innovated devices and nano-systems.

1.2 Objective and Scopes

The main objective of this PhD research is to study and determine refractive index of a single cell and bacterium from the effective value of the refractive index extends to quantitative 3D refractive index mapping. Essential biophysical parameters of waterborne bacteria, i.e. size, shape and effective refractive index, are required to be measured, which is highly crucial in water monitoring industry. On the other hand, the refractive index maps of cells the 3D distribution of lipid droplets in an individual cell are required to be studied for correlation between the refractive index of lipid droplets and the metabolic process and diseases, as well as reactions towards micro-environmental stimulations.

The first objective is to develop and demonstrate the performance of an integrated microfluidic platform, a Lab-on-Chip device, to manipulate the targeted bacteria and measure their effective refractive indices. Based on the conventional immersion refractometry [2], the microfluidic platform will integrate different

microfluidic functions into a single chip to facilitate sample manipulations including buffer modulation, mixing and cell trapping. The primary target is to develop a user-friendly, time-saving and low cost platform, which can provide quick refractive index measurement of bacteria with better sensitivity and precision, as compared with measurements obtained from suspension cells in culture medium. The research investigations include the optimal microfluidic structure design, fabrication process development and experimental studies on refractive index of individual bacteria as well as their physical dimensions. Such microfluidic platform has potential to be extensively employed by biophysicists and bioengineering scientists to do a quick measurement provides that them with necessary database for further biophysical studies.

The second objective is to measure the 3D refractive index map/distribution of individual cells and the refractive index range of intracellular lipid droplets using an optical diffractive tomography (ODT) system with integrated function of fluorescence imaging. The experimental work includes ODT system calibration with polystyrene bead and oil droplets, interferogram capturing and reconstruction of the 3D refractive index distributions with existing program codes, as well as the analysis of the refractive index values-range of lipid droplets. The research findings would provide in-depth knowledge of cellular lipid droplets and their reactions towards micro-environmental stimulants of increasing fatty acid concentration, which is critical for disease studies such as obesity, fatty liver etc.

1.3 Major contributions

The major contributions of this PhD dissertation lie in three aspects. The first contribution is the development of an integrated microfluidic immersion refractometric device and platform, and the fulfillment of the calibration, measurements and data analysis. The research impact is demonstrated with a working prototype of the microfluidic chip. The work includes the optimal structure design, microfabrication processes, and system integration and calibration. Effective refractive indices of three bacteria species, i.e. *Echerichia coli, Shigella flexneri* and *Vibrio cholera* are determined, including their physical/geometrical lengths, widths and aspect ratios. The significance of this research work lies not only in establishing a rapid, label-free and low cost platform for detection of single bacteria in drinking water, but also providing a database of dimensions and refractive indices of the bacteria species for further biophysical studies. For example, bacteria detection by optical scattering patterns, where the refractive index and the size of a microbe govern the optical scattering intensity profile/fringe pattern. The measured biophysical parameters of the bacteria have been used as part of its database by a prototype system for drinking water inspection and early-warning aimed to be broadly utilized by the water monitoring industry.

Secondly, 3D refractive index mapping/distribution of individual cells is studied, with focusing on measurements of refractive index of intercellular lipid droplets and their responses towards micro-environmental stimulation by increasing fatty acid culture medium. Locations of different organelles are verified by compliment fluorescence imaging of them with corresponding dyes, e.g. lipid droplets with BODIPY dye measured by the optical diffraction tomography system. Thus the refractive index values of different organelles can be confined precisely. The refractive index range of intracellular lipid droplets are monitored under the presence of oleic acid of different concentration,

To the best knowledge of the author, such innovative 3D biophysical study of lipid droplets in a whole cell has not been reported before. The research findings may offer in-depth knowledge of cells containing lipid droplets and their reactions towards external stimulants of increasing fatty acids concentration. It also provide significant meaning in studies of metabolic disease, such as obesity and fatty liver, etc... Further research may reveal the benchmark of refractive index of lipid droplets in cell dysfunction and metabolic problems. This measurement methodology is ready for in-depth study of 3D refractive index distributions of many other microorganisms and intercellular organelles.

Thirdly, the extensive study of refractive index measurement methodologies and findings related to its correlation with biological and biomedical behaviors of

various cell lines and malfunctioned cells and disease diagnosis have been explored. Specifically, the size, shape and refractive index of single bacteria have been measured. In disease diagnosis related studies, refractive index of various cells and intercellular organelles have been studied. The extensive information could enrich the study of the refractive indices of cells and bacteria.

1.4 Organization of Thesis

This dissertation is organized into five chapters. The introduction covers the motivation, the objective and scopes, and major contributions as presented in this chapter. The motivation section explains why this PhD research project is carried out. The objective and scopes section states the main focus and tasks of this research project, and the major contribution section highlights the innovations and significant findings in three aspects.

In Chapter 2, an extensive literature survey on the background knowledge related to this PhD project is presented. It firstly presented the cell refractive index models developed and commonly used in measurements and applications. Then, it provides rich information on the important role of the refractive index played in identifying various diseases and determining pathogens, such as in cell biology, pathology and hematology. Next, it introduces various refractive index measurement techniques, including optical densitometry, light scattering,

immersion refractometry, optical resonators and quantitative phase imaging and optical diffraction tomography for 2D and 3D refractive index maps respectively. In addition, the recent developments of micro-optofluidic chips/devices are also presented.

Chapter 3 elaborates the complete development of a microfluidic device and the platform based on immersion refractometry for the detection of refractive index and geometrical dimensions of single bacterium/cells. Firstly, the working principle of the platform is introduced. Subsequently, the design of the multi-functional microchip, the fabrication process and sample preparing protocols are presented. Finally, the experimental system and testing conditions are described followed by reporting and discussion of the experimental measurements of three parameters, namely size, shape and refractive indices of three bacterial species.

In Chapter 4, firstly related principles of optical tomography diffraction are elaborated to provide in-depth knowledge of the technology. Secondly, physiology of lipid droplets and their important function in metabolic related diseases are briefly introduced. Next, the system of ODT and the experimental methodology for obtaining quantitative 3D refractive index distribution of single cells are elaborated. Variation towards external changes using an optical diffraction tomography system with fluorescence imaging is discussed. Subsequently, the experiment work is presented in details starting from system calibration with refractive index

measurement of polystyrene bead and several types of household oil droplets. Then, extensive experiment results with 2D refractive index distributions, which are cross-section slices obtained from the 3D distribution of a single cell, and the distribution profiles of lipid droplets in 3T3-L1 cells are presented and discussed. To mimic the effects of excessive fatty acid in cells, fatty acid of different concentrations was added to the culture medium of 3T3-L1 cells in increasing order and the refractive index profile of lipid droplets in whole cells are measured for possible changes in the refractive index profile in reaction with micro-environmental stimulation by fatty acids.

Chapter 5 summarizes the major research work of this dissertation and highlights some of the interesting findings along with conclusions, and followed by recommendations for future work. With a wide variety of species and the complicity of microorganisms, much more feasible and meaningful research works could be initiated from the literature study and the experimental demonstrations reported in this dissertation.

Chapter 2 Literature Survey

This chapter presents the literature survey in the field of cell refractive index studies and measurement techniques, which are related to the research area of this PhD research work. Section 2.1 introduces popularly used models of cell refractive indices, and the important applications of refractive index in cell biology and disease diagnoses. Section 2.2 briefly introduces different refractive index measurement techniques, including light scattering and interferometry, resonant cavities and microscopic techniques. Section 2.3 introduces optofluidic technology, which provides the capabilities in liquid mixing and cell manipulation. Section 2.4 summarizes the trends of refractive index research and highlights the important issues in cell refractive index applications.

2.1 Cell Biophysical Studies and Disease Diagnosis

Many physical models and theoretical principles are developed to understand and study cell biophysical properties, such as electrical, mechanical and optical properties. Electrical parameters such as impedance, electromotive force and conductivity are very useful in studying activities of cell grown in cell culture and brain activity via neural networks in electrical synapse propagation. While mechanical properties such as speed, elasticity and adhesive forces help monitor physiological status of cell and how it responds to different forces. Optical properties such as contrast, scattering and adsorption etc. determine how light transmits through cells. These parameters strongly relates with intracellular mass and cell thickness. One important biophysical property is the refractive index profile in a single cell. It has been first studied and measured since 1950s. The cell refractive index can be used to determine or correlate with other important biophysical parameters such as dry mass, wet mass, elasticity etc., and study cell metabolic activities such as cell infection and different stages of the cell cycle.

2.1.1 Models of Cell Refractive Index

Several different models of cell refractive index have been established in the past 50 years based on different measurement techniques, which can be classified into three models as described in bellow.

The simplest model is the average refractive index of cell population suspended in a medium [8]. In this model, the suspended cells are assumed to be homogeneous with the same refractive index, the average cell refractive index are measured by applying either the principle of optical densitometry to compare the optical densities of the sample cell population and the medium with optical densitometry, or the principle of interference refractometry. The main drawback of this model is its simplicity without any in-depth refractive index information provided. The large variation of cell refractive index within the same cell type cannot be measured and analyzed.

In early 50s, R. Barer [2, 9] proposed a new effective refractive index model for a single cell, which is defined as $n_{cell} = n_0 + \alpha C$ where n_0 is the refractive index of the medium, α is the specific refraction increment and C is the mass density of protein in g/dL. This model is based on the concept that cell is largely comprised of proteins and cytoplasm inhabiting the largest proportion of cell solids. It is

assumed that a single cell is like an entity filled with protein solution. Hence, the effective refractive index is linearly proportional to the concentration of the proteins in the cell.

Barer showed [2] that by measuring several unconjugated proteins, the specific refraction increment for proteins is $(1.85 \pm 0.02) \times 10^{-3}$. For every one percent increase in concentration, the refractive index of a protein solution increases by 1.85×10^{-3}. The specific refraction increments of some intracellular constituents are listed in Table 2.1 [2].

Table 2.1 Specific refraction increments (α) of intracellular constituents [2]

Constituents	**Specific refraction increment (α)**
Human serum albumin	0.00185
Human gamma globulin	0.00188
Human serum globulin	0.00186
Human α2 globulin	0.00183
Human β1 globulin	0.00185
Human euglobulin	0.00183
Human pseudoglobulin	0.00181
Lactoglobulin	0.00182
β lactoglobulin	0.00182
Peptone	0.00183
Glycine	0.00179

Even though carbohydrates and lipids exist in the cytoplasm but they exist as complexes, which behave similarly and have specific refraction increments as proteins. Barer also investigated the impact of pH values on the specific refraction increments of proteins [9]. It was shown that the pH effect is small and negligible. Between the temperature of 0.5°C and 25°C, it was shown that the effects of temperature on specific refraction increment is also small, amounting about 0.5%. The influence of salt concentration is also marginal and not more than 2% on the specific refraction increment. The refractive index of proteins increase significantly as the wavelength is shortened, the specific refraction increment of pigmented proteins is significantly higher than that of unpigmented proteins. Between these two models, the effective refractive index of a single cell is more accurate than the average refractive index of cell population. The main drawback of this model is the assumption of a single living cell as a spherical object filled with a protein solution. In reality, cells exist in different shapes and other organelles exist in the cell especially cell nucleoli that is denser than the cytoplasm. In most cases, minor changes in the concentration and the abundance of various intracellular organelles are not reflected in the effective refractive index. Therefore, the study of effective refractive index does not provide many details to understand sophisticated cell biological processes. Neither provides sufficient data and information for biological applications based on a single refractive index value to characterize a whole cell. The effective refractive index of a single cell is more

precise as compared to the average refractive index of a cell population. However, both models are limited in providing sufficient information for biological applications with only a single refractive index value to represent a cell.

In recent years, instead of being a homogeneous entity, the cell is viewed as an entity with spatial refractive index distribution. The third model is refractive index map or distribution profile of a single cell. Such a map/profile provides detailed information on refractive index distribution and changes in intracellular scale [10-12]. Since cell refractive index is linearly proportional to the protein concentration, the dry mass density of the cellular matter, $\sigma(x, y)$, can be determined as $\sigma(x,y)=\frac{\lambda}{2\pi\alpha}\Delta\phi(x,y)$ where α is the specific refraction increment in ml/g [11]. With such enrich information pertaining to refractive index of individual cells, biologists and medical researchers can choose to study one cell or a group of cells that is disease related or to investigate cellular functions.

2.1.2 Cell Refractive Index for Cell Biology and Disease Diagnoses

With the development of various refractive index models, it is possible to measure the single cell refractive index. Based on this, researchers can study the other aspects of the cell and how the refractive index is related to them. Originally, the refractive indices of biological samples from cells, tissue to bacteria and viruses

were measured. Next, the refractive index of abnormal cells is compared to normal cells to look for their difference and the link to diseases such as malaria, cancer, and bacterial or virus infection. Here, several applications for refractive index in three different research fields are discussed; including cell biology, hematology and pathology.

Applications in cell biology

Due to rapid improvement in technology, there has been remarkable progress in refractive index measurement techniques and systems. Researchers were able to measure different organelles of a cell, e.g. cytoplasm and nucleus. HeLa cells were also measured [12] whereby the refractive index of the nucleus is between 1.355-1.365 RIU, and the refractive index of the cytoplasm is 1.360-1.390 RIU, while the cell nucleoli have the highest refractive index at 1.375-1.385 RIU. Table 2.2 shows the typical refractive index value of numerous cell organelles [12-14].

Table 2.2 Refractive indices of different cell organelles

Organelles/intracellular matters	Refractive index	References
Cytosol	1.360 – 1.390	[12]
Nucleus	1.355 – 1.365	[12]
Nucleolus	1.375 – 1.385	[12]
Mitochondria	1.400 – 1.420	[13]
Lysosome	1.600	[14]

The refractive index of several different bacteria were commonly measured and examined over the years. The most studied bacteria is *E. coli*. Using the average refractive index model, it is measured with average refractive index of 1.401 [8]. The measured average refractive index of suspended *E. coli* is relatively higher than the measured effective refractive index of single *E. coli.* Under a phase contrast microscope, different organelles and membrane of a single *E. coli* is clearly seen and studied. The nucleoid is separated from the cytoplasm. This contrast between the nucleoid and cytoplasm is due to the difference in their refractive indices and solid concentration. The cytoplasm with protein (21% wt/vol) and RNA (0.5% wt/vol) has refractive index of 1.390 RIU while the nucleoid mainly with DNA (6.8% wt/vol) and low amount of protein (8.6% wt/vol) has refractive index of 1.371 RIU [15].

Furthermore, the morphology of bacteria will also affect their refractive index such as bacillus family, which is able to produce endospore and undergo sporulation. Hence, this creates two different states with very different refractive indices allowing the clear differentiation between their vegetative and sporulation forms. It was shown that bacillus spores (1.517 – 1.539 RIU) have relatively higher effective refractive index than their vegetative forms (1.387 – 1.400 RIU) [16]. This is because the solid content in spore is significantly increased from approximately 30 to 99 g per 100 ml while the water content is reduced from approximately 77.5 to 25.5 g per 100 ml.

As the viral particle is very small in size, it is much harder to measure. The measurement techniques of its refractive index are limited and mainly based on suspension measurement. Due to the limitation of the measurement technique, not much literature can be found for refractive index measurement of viruses.

As cell refractive index is correlated with the concentration of materials, the first direct application of cell refractive index is cell cycle monitoring [17]. During a cell cycle, there is cell growth, which leads to increase in cell matters. In the cell cycle shown in Figure 2.1, the cell initially enters G1 phase and grows by producing proteins and cytoplasmic organelles. Next, it reaches S phase whereby chromosomes are replicated, followed by entering G2 phase to grow more and finally divide in the M phase. Since the DNA content in the nucleus is doubled in

G2/M phases as compared to G1/S phases, the nucleus refractive index of HeLa cells were measured to be increased from 1.5495 to 1.5515 RIU as shown in Figure 2.1b.

The growth of human osteosarcoma (U2OS) cells was studied [18] and they were transfected with YFP-proliferating cell nuclear antigen (PCNA) to monitor the progression through S phase. Based on the results reprinted in Figure 2.2, U2OS cells exhibited clear exponential growth in G_2 phase and typically doubled their mass by the end of G_2 phase. After mitosis, the daughter cells are typically half of their parents' doubled mass. Similar observation was recorded for the growth of *E. coli* [18]. During growth, *E. coli* underwent binary fission whereby DNA was replicated, size was increased and new daughter cells were formed with the complete development of the new cell wall. The growth rate of *E. coli* was shown to be linearly proportional to its mass density, which indicated the exponential growth behavior of *E. coli.*

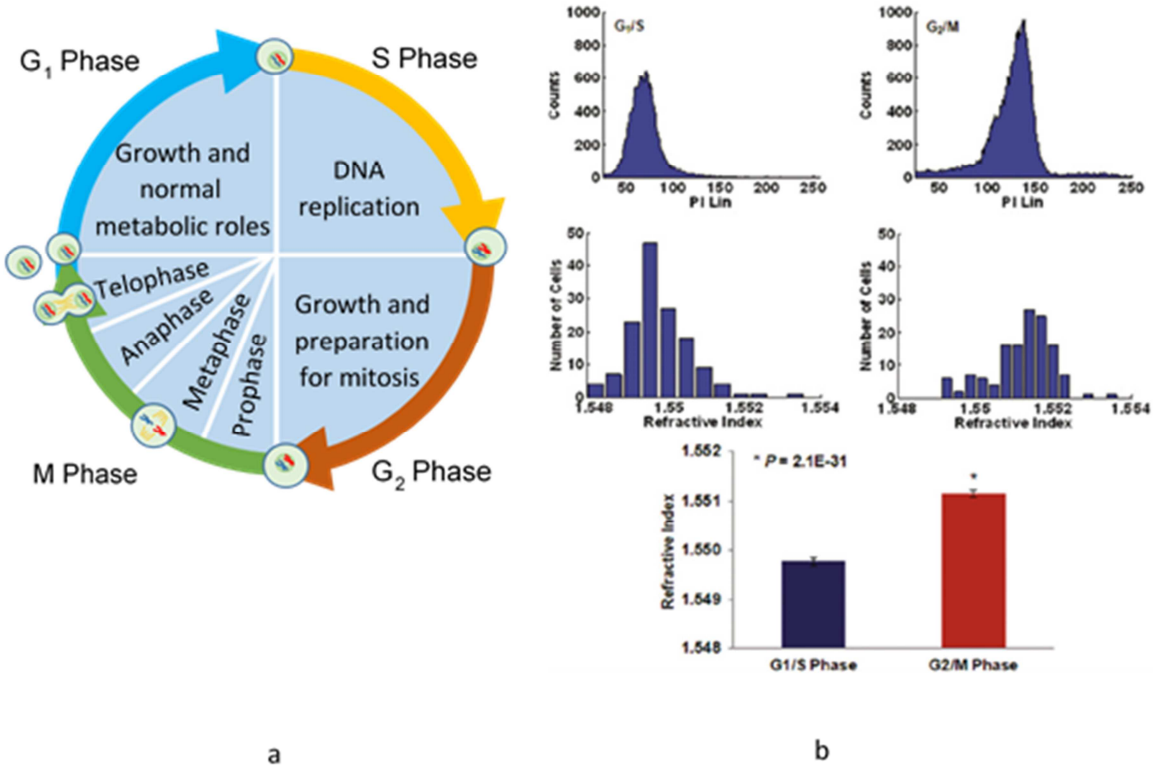

Figure 2.1 Cell cycle vs refractive index: (a) typical cell cycle whereby cell grows in G_1 phase, DNA replicates in S phase and cell continues to grow in G_2 phase, following by cell division in M phase. (b) Flow cytometry and corresponding nuclear refractive index histogram of HeLa cells arrested at the G_1/S and G_2/M phases, and statistical analysis of the refractive index from the cell nuclei [18].

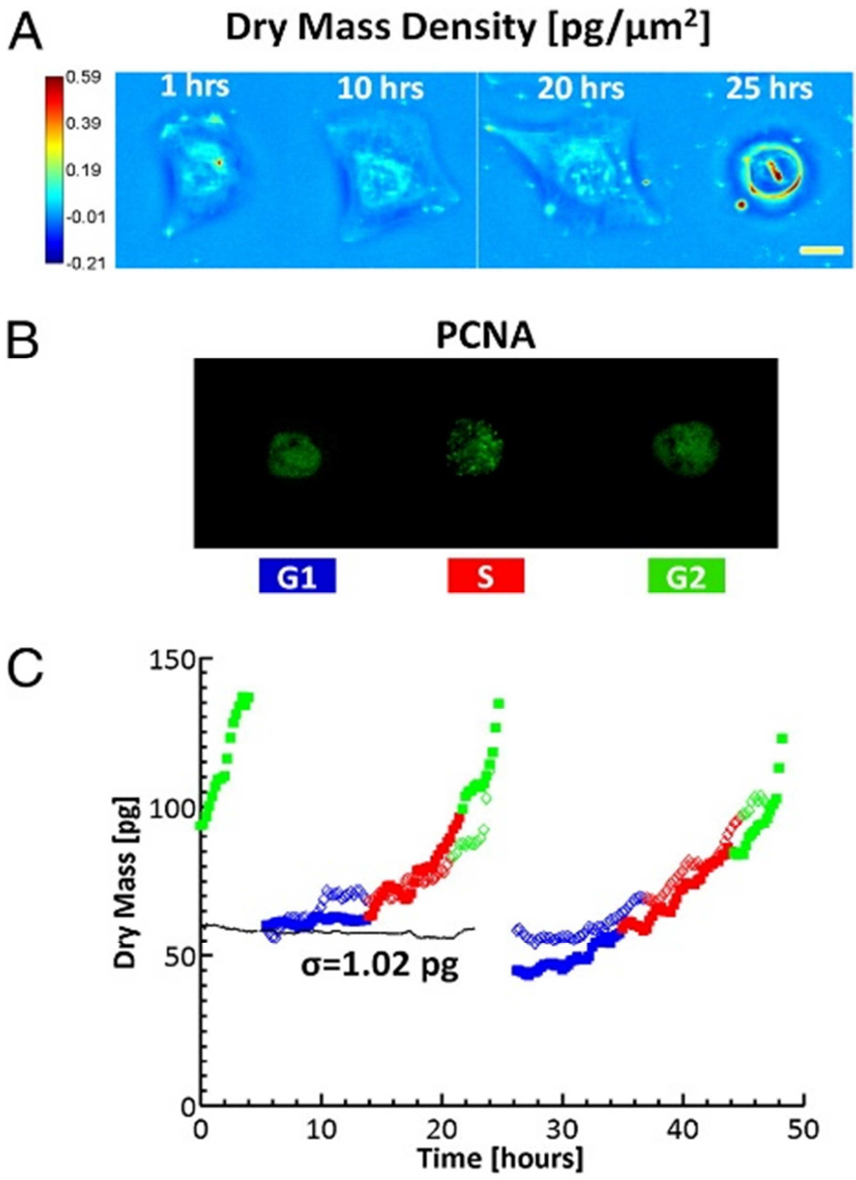

Figure 2.2 U2OS growth over 2 days, whereby (A) shows the dry mass density maps of a single U2OS cell over a cell cycle; (B) shows the GFP fluorescence images indicating PCNA activity; and (C) shows the dry mass vs. time for a cell family from 1 cell being divided to 2 and then to 4 [19].

Using immersion refractometry, the nuclear division during binary fission was also observed [19]. The cycle started as the sister nuclei were separated, forming a septum. The nucleus appeared like a 3-lobed structure. The individual lobes divided as they remained connected together. Then, the nuclear lobes moved apart, and the sister cells were completely separated at opposite ends of the cell. Such a cell cycle continued for a new division for thirty minutes.

Applications in Hematology

There are several cell types existing in the blood stream: red cell, white cell and platelet. Red blood cells are biconcave oval disk shaped with a simple cell structure. They do not have cell nucleus as do most organelles but are rich in hemoglobin. Using a tomographic bright field imaging method [20], red blood cells were determined to have the mean refractive index of 1.402, the dry mass of 27.2 pg, the diameter of 7.0 μm, the volume of 100.7 fL and the density of 27.1 pg/fL.

Platelets are subcellular fragment of blood and also do not have cell nucleus. They help sustain hemostatic and arterial thrombosis especially fibrillation. The two types of platelets that help separate between healthy and unhealthy individuals with diseases are in the form of activated and inactivated platelets. In activated state, platelets have spherical needle-like structure, while the inactivated state is a

discoid shape with diameter of 2 – 4 µm and thickness of 0.5 – 2 µm [21]. When oxygen enters the blood plasma, platelets become activated and a temporary protrusion results in the spherical platelet cell. Due to this difference, platelets are a useful means to determine certain diseases such as cerebrovascular disease, ischemic heart disease and renovascular disease [22-24]. The refractive index of a platelet cell was measured as 1.390 RIU in the range of 1.360 - 1.409 RIU [25, 26]. On the other hand, white blood cells are the body's main line of defense. There are five types of white blood cells in the blood stream, i.e. lymphocytes, monocytes, eosinophils, basophils, and neutrophils. Their sizes are in the range of 6 – 10 µm. Lymphocytes have a relatively simpler structure with a nucleus and small amount of cytoplasm, monocytes has a kidney-shaped nucleus, and others have multilobed nucleus and granules in the cytoplasm as shown in Figure 2.3 [27]. Based on light scattering and multiple-layer spherical model, lymphocytes and monocytes were measured [28] to have nuclear refractive index of 1.43 ± 0.05 RIU and 1.43 ± 0.04 RIU, respectively; and cytoplasmic refractive index of 1.356 ± 0.009 RIU and 1.348 ± 0.004 RIU, respectively. Using immersion refractometry, lymphocytes were measured with cytoplasmic refractive index of 1.3572 RIU [29], which is lower than the one measured by light scattering because of the effective refractive index model. Researchers showed that lymphocytes from infected or vaccine injected animals have a higher refractive index equivalent to 1% to 2% of protein concentration due to the production of antibodies [30, 31].

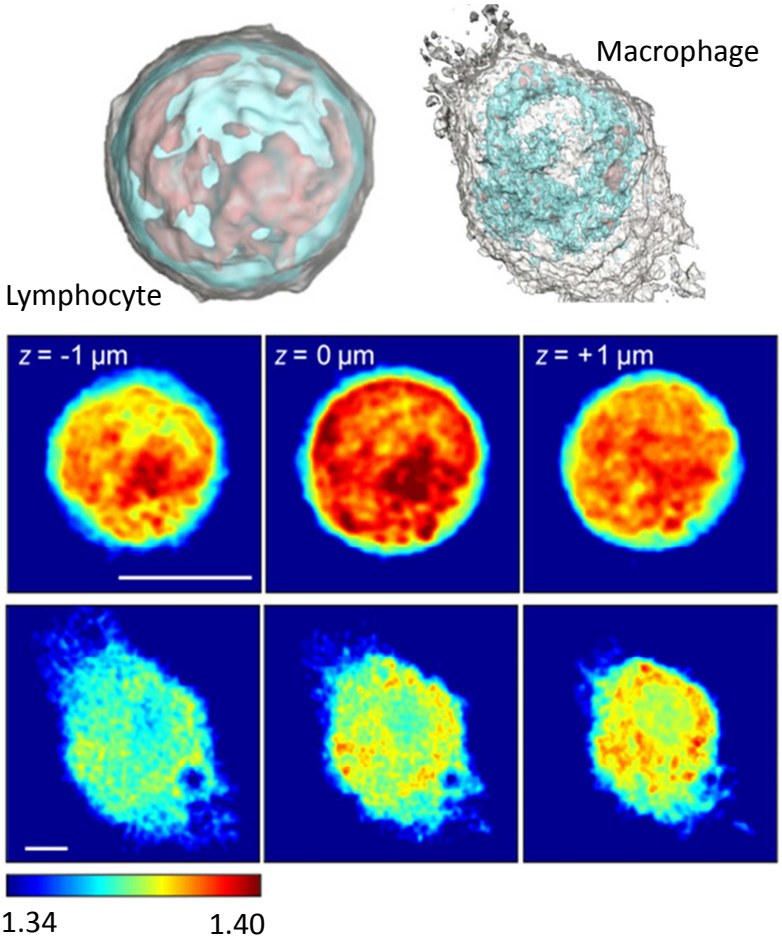

Figure 2.3 Application of cell refractive index in hematology. Rendered iso-surfaces of the refractive index map of lymphocyte and macrophage from the cross-sectional images of 3D refractive index tomograms on various axial planes [27].

Since human red blood cells lack of both nucleus and cellular organelles, by obtaining the refractive index of the cytoplasm of red blood cells, the concentration

of hemoglobin can be determined, i.e. $n_{rbc} - n_0 = \alpha C_{hemoglobin}$ where n_{rbc} is the refractive index of the red blood cell, n_o = 1.335 is the refractive index of cell fluid without hemoglobin and α = 0.0019 dL/g is the specific refraction increment [32]. The hemoglobin concentration for hypochromic anemia patients is relatively lower (37.9 vs 27.4 g/dL). In contrast, for sickle cell anemia where the red blood cell is distorted into a crescent shape and has a solider cell membrane, the stiffness of the red blood cell can be determined by dynamically measuring the fluctuation of the cell membrane using quantitative phase imaging.

Another major disease of red blood cell is malaria with 250 million people infected yearly. Hence, it is critical to detect malaria more effectively early on, allowing early treatment and reducing fatality. Malaria is caused by a protozoan parasite, transmitted by mosquitoes that invade liver cells and red blood cells. There are four species of *plasmodium* that can infect humans and cause malaria, i.e. *Plasmodium falciparum (P. falciparum), P. vivax, P. malariae and P. oval.* However, not all the species are deadly in which only *P. falciparum* caused malaria that leads to lethal infection and results in the most number of deaths, while *P. vivax* leads to severe disability after infection. The malaria infection cycle begins when mosquito feed on people. As the mosquitoes feed on human blood, the malaria parasites called sporozoites are injected into human tissues. The sporozoites travel to the bloodstream and invade the liver cells, which are called hepatocytes.

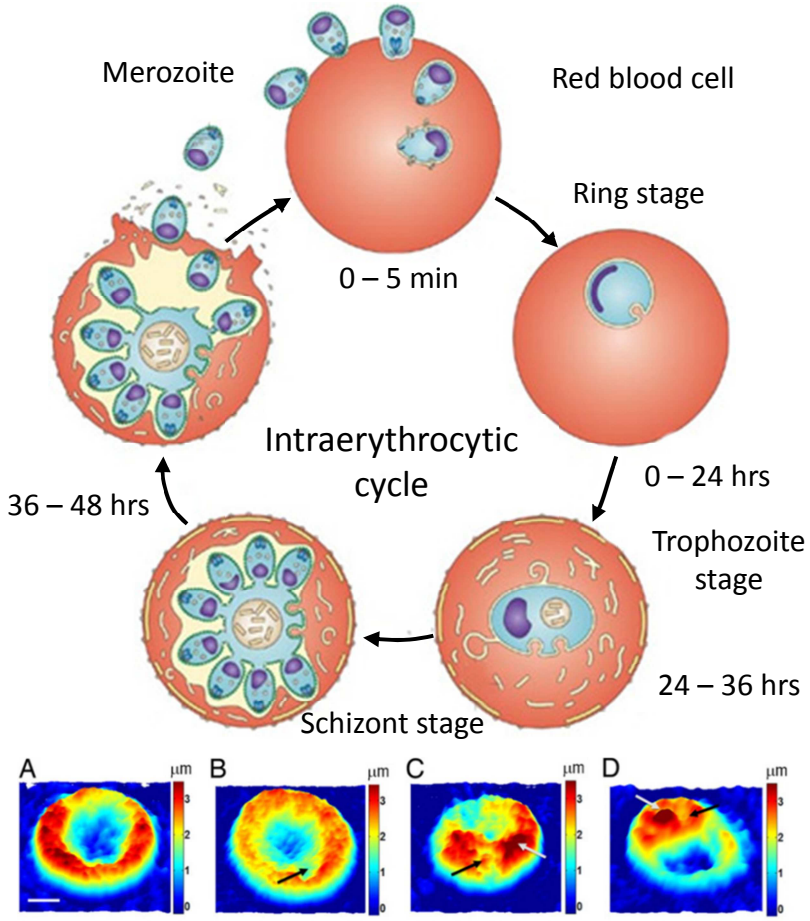

Figure 2.4 Schematic illustration of the intraerythrocytic cycle of malaria infection and its 3D phase mapping at various stages [33]: (A) healthy cell; (B) Ring stage; (C) trophozoite stage; and (D) Schizont stage; where black arrows indicate the merozoite and gray arrows indicate the hemozoin.

With a reprint [33] depicted in Figure 2.4, when the hepatocytes burst, the parasites are released into the bloodstream as merozoites to attack red blood cells and start the intraerythrocytic cycle. The intraerythrocytic cycle causes structural,

biochemical and mechanical changes to red blood cells. The cycle starts from the ring stage at which the merozoites invade red blood cells and become uni-necleated trophozoites. At the schizont stage, trophozoites develop into multi-nuclei cells called schizonts. The growth of schizonts is based on the digestion of hemoglobin with the production of hemozoin [34]. These schizonts undergo differentiation to form multiple merozoite cells in the red blood cell, and the discocyte shape of the red blood cell is lost during progression to the scizont stage.

Healthy red blood cells have a homogeneous distribution in refractive index, while infected red blood cells show non-homogeneous refractive index throughout the cytoplasm of the cell. The lack of homogeneity in infected blood cells may be due to several different factors, such as hemoglobin is metabolized and transformed into hemozoin crystal in the *P. falciparum* membrane. The vacuole of parasite occupies part of the cytoplasm of red blood cell and several types of parasite proteins are transferred from the parasite into the cytoplasm of the infected red blood cell. Parasites cause changes to both the internal and membrane structure of red blood cells. There is a significant refractive index difference between healthy and infected red blood cells. Healthy red blood cells have refractive index of 1.399 ± 0.006 RIU, whereas infected red blood cells have refractive index of 1.395 ± 0.005 RIU in ring stage, 1.383 ± 0.005 RIU in trophozoite stage, and finally 1.373 ± 0.006 RIU in schizont stage [35]. This indicates a significant decreasing trend in refractive index of red blood cells during the infection process.

The decrement of refractive index of the infected red blood cells is associated with the decrease in hemoglobin concentrations. As the infection proceeds, the volume of cyptoplasm reduces as compared to the healthy red blood cell. The results are significant as this shows substantial correlation between refractive index and infection of red blood cells. Red blood cell's refractive index and morphology can be used as important parameters for disease diagnosis such as malaria and anemia. In addition, refractive index of various cells in blood sample can be further studied and developed as one of the indicators in hematology laboratory diagnosis.

Applications in Pathology

Cancer cells have certain irregularities such as increased nuclear size, irregular shape and uneven chromatin texture [36]. Based on these features along with developments in nanoscale detection systems, prognosis and early discovery is becoming highly feasible. The refractive index of normal and cancer cells have been well researched into, so as to better understand the atypical cell cycles and increased proliferation of cancer cells. Most normal cells have refractive index of 1.353 RIU and cancer cells have higher refractive index ranging from 1.370 to 1.400 RIU [37, 38]. This could be the result of the abnormal cell cycles and increase in cell multiplying seen in cancer patients; where there is a large increase in cell production within the different cell cycle stages of cancer patients.

The refractive indices of breast biopsies cells were studied to determine their respective refractive indices: normal cells, cancer cells that are identified as normal cells and malignant cells [39]. It is seen that the nuclear refractive index is increased from 1.542, 1.544 to 1.545 RIU, where the normal cells have lowest refractive index and as the cancer cells increase the refractive index becomes higher. This increasing trend indicates as the cancer cells is higher the nucleus refractive index also increases. Hence nucleus refractive index can be a useful and significant factor for early-stage cancer diagnosis.

Clinical studies show that circulating tumor cells (CTCs) are presented in the blood stream when cancer metastasis occurs. The CTCs in the peripheral blood stream are good indicators of the presence of primary tumors and also correlated with the overall survivor rate of cancers such as breast, prostate and colorectal cancers. Thus identification, enumeration, and characterization of CTCs are vital to allow early detection of cancer. However, the concentration of CTCs (10 cells/ml) are relatively very low as compared to white blood cells (10^6 cells/ml) and red blood cells (10^9 cells/ml), which makes it much harder to detect CTCs. The biophysical properties of CTCs and leukocytes in an ovarian cancer patient were measured and compared by using quantitative phase imaging [40]. The results showed that CTCs have higher mass (33.6 *vs* 18.7 pg), greater volume (518.2 *vs* 230.0 fL) and lower dry mass density (0.065 *vs* 0.085 pg/fL) as compared to leukocytes. These results provide insight into the development of label-free biophysical CTC detection

system, and aiding to understand the genetic and proteomic composition of CTCs for targeted therapies. As the drawback of single cell observation is small amount of data to strongly support conclusion, hence the best way is to get more results to increase the credibility in biological study. It is important to increase the number of sample cells included as statistically significant to achieve a higher level of detection accuracy and usefulness of such a method.

2.2 Techniques for Refractive Index Measurements

Various refractive index measurement techniques are briefly introduced in this section. For easy reference, system specifications of most techniques are tabulated in Table 2.3.

Table 2.3 Measurement methods and their specifications

Cell refractive index model	Measurement technique	Refractive index resolution (RIU)	Minimal mass density change (pg/fL)*	Spatial resolution (nm)	Refs
Average refractive index of suspending cells	Interference refractometer	3×10^{-3}	0.0163	-	[8]
	Optical densitometer	3×10^{-3}	0.0163	-	[8]
	Light transmission and reflection	10^{-2}	0.0542	-	[41, 42]
Effective refractive index of a single cell	Light scattering	1×10^{-3}	0.0542	-	[43]
	Immersion refractometer	1×10^{-2}	0.0054	-	[44, 45]
	Laser resonant cavity	4×10^{-3}	0.0217	-	[46]
	FP resonant cavity	3×10^{-3}	0.0163	-	[47]
	Grating resonant cavity	1×10^{-3}	0.0054	-	[48]
2D Refractive index mapping by QPI	Digital holographic microscopy	3×10^{-4}	0.0016	-	[10]
		3×10^{-4}	0.0016	-	[51]
	Hilbert phase microscopy	2×10^{-3}	0.0108	1000	[55]
3D Refractive index mapping by ODT	Digital holographic microtomography	9×10^{-3}	0.0488	250	[7]
	Tomographic bright field imaging	8×10^{-3}	0.0434	260	[20]
	Tomographic diffraction microscopy	1×10^{-3}	0.0054	-	[57]
	Tomographic holographic microscopy	1×10^{-2}	0.0542	-	[63]
	3-D translational digital holography	5×10^{-3}	0.0271	350	[65]

2.2.1 Optical Densitometry, Scattering and Immersion Refractometry

Figure 2.5 demonstrates the principle of optical densitometry which is based on an assumption that all suspended cells are homogeneous with the same refractive index. It measures the transmission light propagating through the medium with cell suspension following the principle that when the refractive index of the medium and that of the suspending cell population are matched, then the average refractive index of the cells is known. In practice, the average refractive index can be determined by increasing medium′s refractive index through incremental changes and measuring the optical density after each increment. When the transmission light achieves its maximum, it means that the refractive index of cells matches that of the medium and thus no diffraction. Bateman *et al.* used an optical densitometer to measure the average refractive index of cell population suspended in a medium [8]. They also used Rayleigh type interference refractometer to measure the average refractive index of the cell suspension.

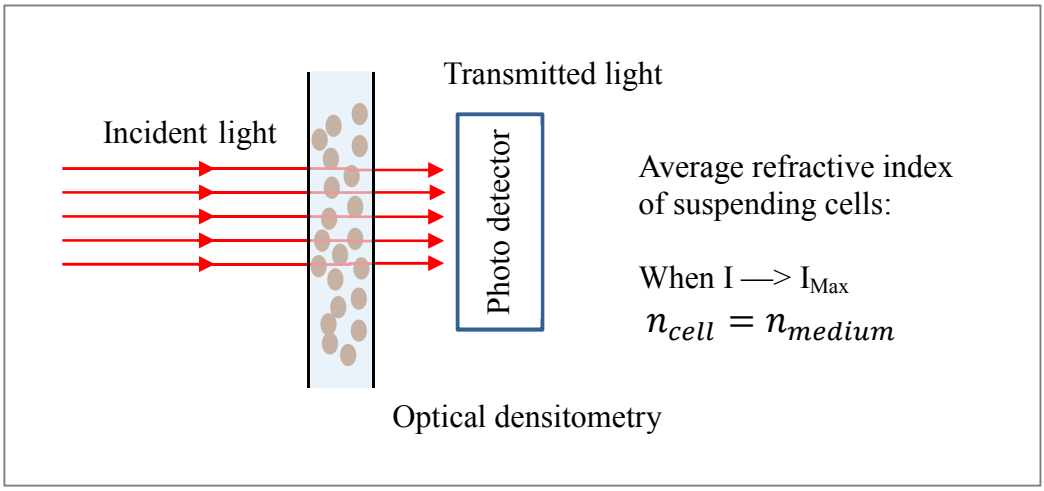

Figure 2.5 The model for the average refractive index of cells suspended in a medium measured by optical densitometry.

In interference refractometry, the average refractive index of the suspended cells (n_{cell}) is determined based on the classical equation of $n_{cell} = n_0 + \frac{\Delta n}{V}$ where n_0 is the refractive index of the medium, V is the volume fraction of cells in the medium and Δn is the difference of refractive index measured by an interference refractometer [8].

Another optical method that can be used to determine the refractive index of a biological sample is the optical scattering method, which normally measures the angular-resolving scattering intensity profile [26, 32, 38, 42]. Light scattering is the deflection of light rays from the directions governed by geometrical optics. It is

due to the anomalies in the propagating medium or at the interface between two media. For a specific sample and medium, the scattering pattern of light with a particular wavelength is the function of the scattering angle. This parameter provides the morphological and structural information about the sample. A comprehensive overview with models of different cell species and the detailed explanations of the scattering method as well as the experimental results can be found in Ref [28]. In optical scattering studies of most living cells, which are usually spherical in shape, the Mie scattering model is used as an analytical solution of Maxwell's equations to establish the scattering pattern of a spherical (or close to spherical) object [41] with its dimension close to the wavelength of the light. The scattering data is inverted based on creating a model and altering the parameters to get the least square fit to the scattering data, to determine the size and refractive index of a spherical sample [42]. Another measurement technique is spectral reflectance and transmittance detection of refractive index [43].

Besides optical densitometry and scattering methods, immersion refractometry can also be used for refractive index measurement is immersion refractometry. The cells are immersed in a liquid medium and by observing the light properties propagating through an individual cell in medium, the effective refractive index of the sample can be determined [44, 45]. This method will be discussed in details in subsection 3.12 as the working principle of the developed microfluidic immersion refractometer.

2.2.2 Optical Resonant Cavities

Several microfluidic chips integrated with various optical resonant cavities were demonstrated to determine the effective refractive index, dry mass and wet mass of single living cell. Figure 2.6 shows one example of the method with a fiber-based Fabry-Pérot resonant cavity [46]. Other methods include an on-chip laser resonant cavity integrated with a microlens and a micromirror [47], and a grating resonant cavity with optical trapping [48], etc... Resolution up to 10^{-3} refractive index unit (RIU) was demonstrated [48]. Most of these techniques measure the optical path difference caused by the cell in the medium and decouple its effective refractive index and size by the differential buffer method.

In this method, two buffers with different RIs (n_1 and n_2) are injected into the cavity alternatively. Four transmission spectra can be obtained with two spectra for each buffer, i.e. with the absence/presence of the single cell in the cavity. Subsequently, the refractive index and size of the cell, n_{cell} and l_{cell}, can be determined as

$$n_{cell} = (n_2\Delta\lambda_1 - n_1\Delta\lambda_2)/(\Delta\lambda_1 - \Delta\lambda_2) \quad \text{and} \quad l_{cell} = (\Delta\lambda_1 - \Delta\lambda_2)/[k(n_2 - n_1)]$$

where $\Delta\lambda_1$ and $\Delta\lambda_2$ are the resonant peak shift with/without the cell in medium 1 and 2, respectively, and, k is the dimensionless constant of the cavity. The main

drawback of these techniques is the assumption of a single living cell as a spherical object filled fully with a protein solution. In reality, cells exist in different shapes and other organelles exist in the cell especially cell nucleoli that is denser than the cytoplasm. In most cases, minor changes in the concentration and the abundance of various intracellular organelles are not reflected in the effective refractive index. Therefore, the study of effective refractive index cannot provide details to understand sophisticated intracellular biology and life process.

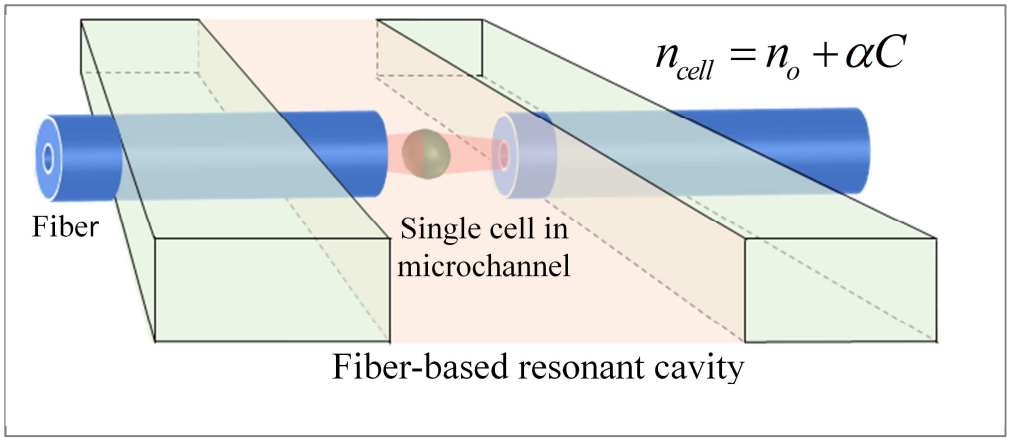

Figure 2.6 Method for measurement of the effective refractive index of a single cell by resonant cavity [46].

2.2.3 Quantitative Phase Imaging and Optical Diffraction Tomography

The refractive index map/distribution of a single cell can be obtained by using the quantitative phase imaging (QPI) technology [3-6, 10, 11, 33, 40]. The main factor

distinguishes QPI technology from classical bright-field microscopic imaging is that the former employs the principle of interferometry and introduces a reference beam to record the complex optical field with both amplitude and phase information while the later only record amplitude. With corresponding phase extraction/unwrapping algorithms, such as Fourier transform [3, 4] and Hilbert transform [3, 49], 2D phase delay map/distribution of the complex field at the recording plane, $\Delta\varphi(x, y)$, can be obtained. $\Delta\varphi(x, y)$ is the difference between the plane wave reference beam and the diffracted object beam by a weakly scattered cell. While the Hilbert transform is suitable for imaging optically thin samples, the images are recorded in the focus plane rather than in an out-of-focus plane. From the 2D phase delay map, the 2D refractive index map/distribution of the cell or a microorganism $n_{cell}(x, y)$ can be related to $\Delta\varphi(x, y)$ as [4]

$$n_{cell}(x,y) = n_0 + \frac{\Delta\varphi(x,y)\lambda}{2\pi h_{cell}(x,y)}$$

where λ is the wavelength of light and $h_{cell}(x, y)$ is the thickness of the cell.

The QPI technology can be classified to different categories based on the modulation schemes and optical configurations. Firstly, they can be divided to time-domain and spatial-domain modulation types. Time-domain modulation type is normally adopting the technique of phase shifting interferometry (PSI) [4, 5, 50, 51], which records a series of interferograms from the minimum of three frames to

hundreds by changing the phase of the reference beam with respect to that of the sample beam. One phase delay map/distribution is then extracted from the series of interferograms by phase unwrapping algorithm [50, 51]. It can be realized by either acousto-optic modulation (AOM) [12] or translating a mirror in the reference arm with a piezoelectric transducer (PZT) [7]. As this scheme requires several interferograms for one optical field image, the speed is governed by the modulation speed. In principle, its lateral resolution can maintain the diffraction limit of about 250 ~ 300 nm depending on the wavelength of light source used.

The other modulation scheme is the spatial-domain type, which is divided into in-line holography and off-axis holography. In-line (Gabor's) holography [4, 52], which employs the scattered and un-scattered light from a weakly scattered sample as the object and reference fields for a hologram/interferograms. It is simpler in optical configuration but more difficult to reconstruct the field image due to overlapping of the unwanted phase–conjugated twin–images. In off-axis diffraction holography called common path method, the reference beam has an angle with respect to the sample beam [4, 5, 53-55]. It is normally realized by inserting a grating with a large through hole in the center and one small pin hole to allow both zeroth order and the first order diffraction light to pass through. Due to superposition of the reference and sample beams, the interference image of the cell is formed and the phase map can be extracted from one image through phase unwrapping and background subtraction algorithms. Thus its speed is only limited

by the recording camera. By knowing the shape of the cell, the 2D refractive index profile is attained. A high resolution of 10^{-4} RIU is achieved with this method. Jo *et al*. [55] combined the grating type diffraction phase microscopy with an angular-resolved light scattering algorithm, in particular the Fourier transform light scattering algorithm.

Mach-Zehnder interferometric setup is another popular off-axis configuration for transparent objects where the reference beam goes directly as one arm to the photodetector [6, 56]. Lue *et al*. [56] used the built-in confocal 3D imaging function to acquire the physical thickness to compare with the "optical thickness" of the sample measured by phase microscopy. While many other researchers using QPI technique to achieve 2D refractive index maps assuming individual cells has thin and constant thickness.

With strong interests on 3D phase (delay) distributions and significant applications of 3D refractive index distributions, the technology of optical diffraction tomography (ODT) [7, 12, 20, 27, 57, 58], also called digital holographic tomography, has developed as an extension of QPI. ODTs are developed with similar optical configurations, frequency domain manipulations and reconstruction concepts. The major advancement of ODT over QPI is to employ multiple independent 2D interferograms generated by multiple angles or wavelength scanning/changing, and perform 3D Fourier diffraction transform and inverted

transform to achieve 3D refractive index map/distributions [57]. Bailleul *et al*. [58] demonstrated real-time reconstruction in 3D tomographic diffractive microscopy. While time-consuming reconstruction has been a severe obstacle along the development of ODT, preventing it being used in many dynamic applications.

Common-path off-axis interferometric 3D diffraction tomography technique has gained increase interests in the last two decades [59-61]. One typical common-path optical layout [59] for 3D refractive index distribution of single cell is shown in Figure 2.7, where a diffraction grating is utilized to generate the reference and object beams with its zeroth and first order beams respectively. Such common-path configuration has demonstrated lower temporal phase fluctuation and thus better measurement precision than a Mach–Zehnder configuration but it requires a more complicated reconstruction algorithm. Kim *et al*. [60, 61] reported that they realized a compact QPI unit with a half-wave plate, a Wollaton prism and a linear polarizer, which could be attached to an inverted microscope with angular scanning capability to realize the function of ODT.

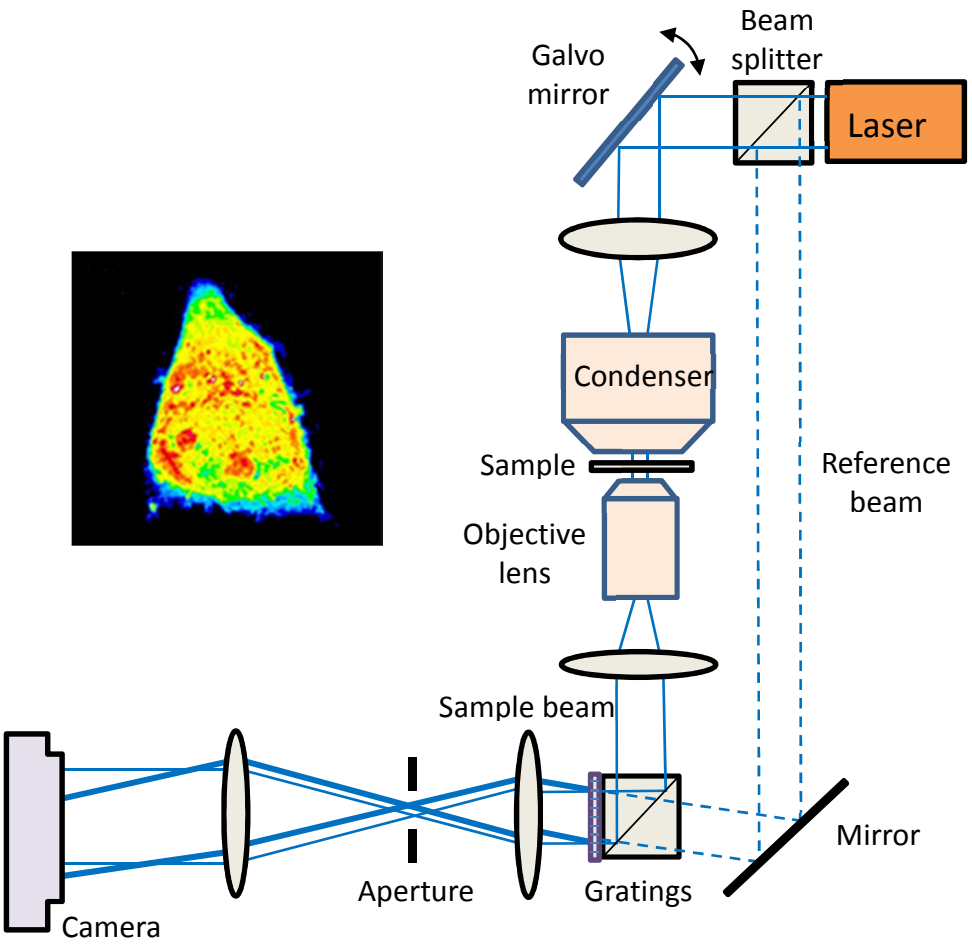

Figure 2.7 A common-path off-axis digital holographic microtomographic system for refractive index mapping [59]. The object and reference beams were the zeroth order and the first order of the light from the grating.

Many researchers still prefer to Mach-Zehnder optical configuration for their ODT systems [7, 12, 27, 58, 62-65]. Su *et al.* [7] employed a pair of mirrors to do angular scanning of live cell and mounted one PZT at the reflection mirror of their

reference beam to realise phase shifting. At a fixed angle, they capture 7 phase shifted interferograms and unwrapped them to achieved one phase image. They obtained the 3D refractive index map with 41 frames of scanning angles, as compared with previous studies using at least hundred over scanning angles. In the studies of [12, 62, 63], they used a pair of scanning mirrors for angular scanning and also a pair of acoustic-optical modulators (AOMs) in the reference beam for shifting of the frequency of the 633nm laser beam by 1250 Hz, generating $\pi/2$ phase shift between 4 consecutive interferogram frames at a fixed angle. They used a simpler reconstruction algorithm of filtered back-projection analogous to the projection of absorption in X-ray tomography. Kim *et al*. [65] later realized real-time visualization of 3D dynamic behaviours of red blood cells with a powerful graphic processing unit (GPU) implementation in their processing computer to realise tomographic reconstruction 17 times faster than conventional ODT with CPU computation.

There has been another approach to realise 3D refractive index maps of cells, which is called synthetic aperture tomographic phase microscopy [66, 67]. Lue, *et al*. [66] proposed to use line-focused beam for translational motion without the need of axial scanning of the object lens. A set of transmitted complex field images of cells at successive points of transverse translation was taken with a focused line beam. Y. sung *et al*. [67] applied this technique to generate 3D refractive index distribution of flowing cells in a microfluidic channel. They used line illumination

and off-axis optical configuration to record the angular spectra of light scattered from a flowing cell at high speed. With a filtered back-projection algorithm, they obtained depth-resolved 3D refractive index map of the cell.

2.3 Optofluidics and Microfluidics

With on-going research advancements in developing integrated optical systems into the microfluidic system, Compact and portable lab-on-chip systems with robust cellular manipulations, treatment and optical detection have been employed extensively in biomedical research areas [68, 69], State to art functions like precise mixing [70] and cell sorting [71] have established many micro total analysis systems (μTAS). Particularly, due to the size compatibility with cells, optofluidic and microfluidic devices have been fruitfully employed in single cell analysis [72]. Numerous applications have been reported in literature for biological analyses, chemical detections and biomedical diagnostic.

The synergic combination of optical mechanisms with a microfluidic device is known as optofluidics. Optofluidic systems combine the compactness and portability of microfluidic device with exclusive optical functions and detection setup to allow single cell detection without time-consuming and labor intensive procedures. With main parts of optical detection are light sources, light guiding

elements and photodetectors, they act as miniature platforms for cell manipulation, treatment and detection. Such miniaturized optofluidic platforms/systems perform fast and non-contact for high quantity single cell analysis in a well-ordered environment. Microscopes, pulsed lasers and fluorescent biomarkers are some of the most common means to be used with microfluidic devices to form an effective system/platform for cell analyses.

The common light source used in optofluidic devices is a laser source. Near-infrared laser can be used for cell sorting, while pulse laser is used to optically transfect single cell with DNA, RNA or nanoparticles. Visible-range laser lines are often used for fluorescence detection, optical imaging and label-free spectroscopy. However, bulk laser sources are unsuitable due to large size and high power usage. Microfludic dye lasers have been developed to facilitate an integrated laser source. Micro-cavity fluidic dye lasers are established using a pair of metallic mirrors or a ring resonator to form the laser cavity [72]. Liang *et al*. [46] integrated a 1550 nm laser diode in their resonant cavity type of device for refractive index measurement.

In microfluidic systems, integrated optical elements that have been demonstrated can be divided into three phases, i. e. solid-air phase, solid-liquid phase and liquid-liquid phase. Initially, optical elements are designed using the interface of the chip material and air. For example, solid lenses are patterned and fabricated using soft lithography [73]. Different radii of curvature of interfaces can be easily fabricated.

In-plane microlenses are fabricated to focus or collimate the incident light and increase the excitation light intensity in the neighboring microfluidic channels or chambers. Song *et al*. [47] inserted two fibers in their microfluidic device and made use of the two facets of the two fibers to form a Fabry-Pérot cavity for refractive index measurement of a single living cell. Chin *et al*. [48] inserted a pair of Fabry-Pérot grating (FPG) fibers in their microfluidic device to form a grating resonant cavity also for refractive index measurement of a single live cell. Subsequently, solid prism can be easily realized by controlling the incident angle of the light on the solid-air interface [74]. Although the integration of optical elements is solved, the main limitation of the solid-air optical elements is the lack of tunability as using fixed geometries. To provide certain tunability in optical properties, tunable optical elements are demonstrated based on the flexible solid geometries or the solid-liquid interface. Microlenses fabricated with flexible and deformable membranes are capable to tune its radii of curvature in a limited range [75].

Optofluidic platform provides an ideal approach to study cell biophysical properties [46-48, 76, 77]. Properties such as size, shape, mass [76], deformity, cell viability and refractive index offer important information about individual cell conditions and the biological functions of these cells. They also provide significant insights to disease and infections. Biochemical properties, such as protein secretion, calcium levels, and surface biomarkers are also used to understand cellular

functions or reactions to environmental conditions. In broader fields of health, food, water and energy, optofluidic devices have all taken significant roles [78].

Compared to other systems based on mechanical, magnetic or electrical detection setups, optical methods are much easier to be implemented in a microfluidic system. Microfluidics combined with free or imbedded optics offers greater flexibility for measurements based on cell biophysical properties and provides higher accuracy in cell analysis.

2.4 Summary

Cell refractive index is one of the key biophysical parameters extensively studied, starting from the average refractive index of suspending cells and the effective refractive index of a single cell to the recent 2D and 3D refractive index distribution of organelles within a single cell. Based on the refractive index value, the concentration of solid mass in the cell, the dry mass and wet mass of the cell can be determined consequently. In this chapter, various new biological insights are briefly introduced. Due to the complexity of live cells and other microbes, it is critical to consider the following criteria when cell refractive index is used for cell analysis and disease diagnosis:

- ***Statistical sample size*** – Cell refractive index, size and mass etc. vary in a range even for the same cell species. In such a case, it may not be conclusive to determine cell types or states with a limited number of cells. To extract meaningful and correlated information from the cell refractive index, it is essential to have a sufficiently large number of cells in different cell stages of the life cycle.

- ***Dependent on measurement conditions*** – The measurement of cell refractive index is highly depending on many factors: the wave length of the light source used, the chemical pre-treatments, extracellular conditions such as live or fixed samples, temperature, osmotic pressure, culture medium, etc. Therefore, for any investigation to correlate cell refractive index with cell state or disease diagnosis, experimental conditions have to be controlled and maintained throughout the experiments.

- ***Non-specificity*** – Cell refractive index is non-specific to chemical or protein molecules. For the same species of microbes, such as bacteria, their refractive indices are having similar values and their sizes are sometimes overlapping, thus the measurement diversity become noticeable. However, it has a potential in complement with biomarkers and corresponding techniques such as fluorescence imaging to achieve specificity and provide more complete information on the target microbes.

- ***Lateral resolution*** – Formerly, only average refractive index of suspending cells or effective refractive index of single cell can be measured, which limit the applications of cell refractive index due to the lack of details and resolution. With the advanced development of optical imaging techniques, cell refractive index mapping offers substantial resolution and detailed information for the studies of cell biology, hematology and pathology. Not only diffraction limited lateral resolution is preserved, rapid temporal resolution and 3D life cell imaging can also be realized. However, the diffraction limit of lateral resolution may hinder the applications of cell refractometry for nano-sized viral particle in virological studies or single molecule or sub-cellular organelle analysis.

On the other hand, robust and rapid manipulation methods for cells and liquids in microfluidic platforms have gained more attention in the research community of single cell imaging and refractometry and other biological studies. Microfluidic devices have also appeared in complicated microscopic techniques such as QPI and ODT. Considering 2D and 3D refractive index measurements have become main trends in physiological study of various biological objects, the integration of microfluidic platforms with advanced optical imaging and refractometric systems would facilitate more advanced rapid and label-free biological and pathological studies of cells and other microbial with 2D or 3D information.

Chapter 3 A Microfluidic Immersion Refractometer for Refractive Index Measurement of Single Bacterium

This chapter introduces a microfluidic immersion refractometer for the measurement of biophysical parameters (size, shape and refractive index) of single waterborne bacterium. Section 3.1 introduces the definition of the refractive index and principles of the phase contrast microscopy and the immersion refractometry. Section 3.2 presents the design of the microfluidic immersion refractometer, which consists of a bacterium trapping chamber and a micromixer for efficient mixing of liquid media. Next, section 3.3 describes the fabrication process of the PDMS chip, the experimental setup, bacterial culture protocol and sample preparation processes. In section 3.4, experimental results are shown; from the efficiency of the micromixer and the biophysical parameters of the three different bacteria species. Lastly, section 3.5 concludes the chapter with future potentials for the microfluidic immersion refractometric platform in water monitoring network.

3.1 Refractive Index, Phase Contrast and Immersion Refractometry

Refractive index, denoted by *n*, is a dimensionless physical parameter of a substance which describes how light propagates through, or more precisely, interact with a substance. It is defined as the ratio of the velocity of the light propagating in vacuum, *c,* to the velocity propagating in a specific substance/medium, *v,* as

$$n = \frac{c}{v} \tag{3.1}$$

The most popular method to determine the refractive index of a liquid medium, and thin films is an Abbé refractometer which applies the principle of critical-angle for total internal reflection. For irregular surfaces or very small objects in millimeter or micrometer scales, the method of immersion refractometry is popularly applied. It is based on the phase contrast between the substance and its surrounding medium.

The refractive index of a substance is strongly influenced by the ambient temperature and the wavelength of the light used to measure it. Therefore, refractive index measurements are usually reported at a reference temperature of 20°C with a reference wavelength of 589.3 nm.

3.1.1 Phase Contrast Microscopic Imaging

Biological objects, such as cells, are relatively thin and transparent, which usually have weak absorption and weak scattering. Therefore, the contrast between biological samples and the background is too low to be observed clearly under bright-field microscope. Without much change in the amplitude, these biological objects do change the phase of the incident light. Hence, the phase change of light after propagating through a biological object, which is also called a phase material, can be considered as an important parameter to generate phase contrast for microscopic imaging and related analysis.

Phase contrast microscopy is a label-free imaging technique using a contrast-enhancing method based on coherent light interference. It alters the light at the image plane to increase the contrast between a weakly scattering samples and the background by increasing phase difference between the transmitted light (background) and the diffracted light (from the sample), and converts difference in optical path length to difference in amplitude of the optical field. A schematic optical layout of a phase contrast microscope [79] is shown in Figure 3.1 for easy understanding of its working principle. With two phase rings, diffractive light and non-diffractive light can be separated and adequate phase difference can be achieved by retarding the phase of the diffraction light with a phase plate while

non-diffractive light remains unaffected. Thus, details in cells can be amplified by utilizing the phase contrast microscopy.

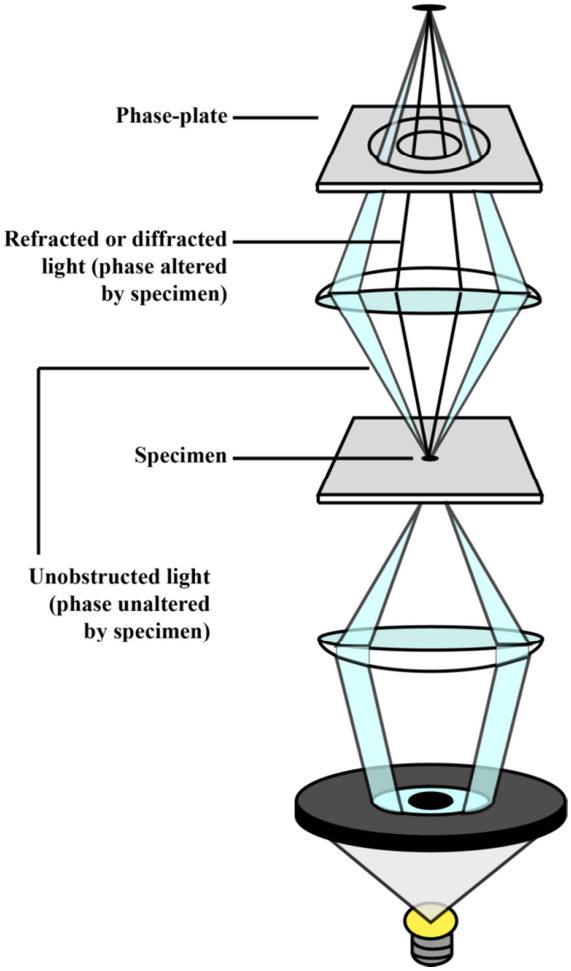

Figure 3.1 Schematic optics of a phase contrast microscope [79].

There are two types of phase contrast microscopes. A positive phase contrast microscope causes a sample in light background with brighter halo while a negative one causes the sample in dark background with darker halo. Halos are one of the artifacts in the technique, and it will become more distinctive with larger difference between refractive indices of the sample and the background due to the

increase of phase differences. In fact, it is possible to employ a "null" method to determine the refractive index of a phase object with a medium with known refractive index through the phase change, $\Delta\varphi = \Delta nd$ where Δn is the refractive index difference and d is the thickness. With the characteristic of label-free and high contrast, phase contrast microscopes have been widely used for (living) cells and tissue imaging and numerous other applications.

3.1.2 Immersion Refractometry

The principle of immersion refractometry has long been used in mineralogy. In simple words, the immersion method means matching the refractive index of an object to that of a surrounding liquid medium. In the early 50s, R. Barer and co-workers proposed an effective refractive index model of a single living cell and adopted the conventional immersion refractometry for refractive index determination of a single living cell [2, 9, 80, 81]. This model is based on the approximation that the cytoplasm inhabits the largest proportion of the cell solid while the cytoplasm is largely comprised of proteins, thus the cell is largely comprised of proteins. It is assumed that a single cell is like an entity filled with protein solution. Hence, if the external medium uses a protein solution, the environment would cause the least disturbance or damage to the cell, from pH values to osmotic effect. From their extensive search and testing, they found that most common species of protein hold the same linear equation, i.e., the effective

refractive index is linearly proportional to the concentration of the proteins in the cell expressed as [2, 9]

$$n_{cell} = n_0 + \alpha C \qquad 3.2$$

where n_o is the refractive index of cell culture medium, α is a constant known as the specific refraction increment, which depends on the nature of the solute, and C is the mass density of the protein, in terms mass in grams per unit value of 100 ml.

Based on Barer's model, the effective cell refractive index is linearly proportional to the concentration of protein in the cell. Several unconjugated proteins were measured in solution form and their specific refraction increments α have about the same values of $(1.85 \pm 0.02) \times 10^{-3}$ [9]. Barer showed that indeed the variation of refractive index as the protein concentration increases is a linear relationship with insignificant discrepancy even at high protein concentrations. A table tabulated their experiment results can be found in §2.1.9. Therefore, Equation 3.2 holds for many different proteins, i.e. the refractive index of a protein solution increases by 1.85×10^{-3} for every one percent increase in concentration regardless the species of the protein. Although lipids and carbohydrates exist in the cytoplasm, they occur as complexes, which have similar refraction increments as proteins. The influence of pH value on the specific refraction increment was investigated and the results showed that the effect of pH is small and negligible [2, 80]. Similarly, the effects of temperature and salt concentration were investigated and their effects on the specific refraction increment are small and within 0.5% to 2%. Then they used a

plasma albumin which is available as a dried powder, as their solute for the immersion medium.

As with a bright-field microscope, the brightness contrast associated with the experienced phase delay is minute to be observed. In order to increase the system's sensitivity, a phase-contrast microscope must be employed to enhance the brightness contrast caused by the experienced phase delay.

However, there are limitations of immersion refractometry due to technology at that time, which include the lack of exact control in the medium changing process; the absence of non-contact cell trapping in which contact based cell trapping will have noise artifact and the difficulties to incorporate other biological techniques. This motivates the development of an microfludic platform based on immersion refractometer with the capabilities of cell trapping and liquid mixing.

Immersion refractometry is thus employed in current research project for measurement of the effective refractive index of a single bacterium by immersing it into a liquid medium and observing the optical contrast between the bacterium and the liquid medium, where n_{bac} and n_0 are the refractive indices of the bacterium and the liquid medium. Referring to Figure 3.2, when the bacterium has a refractive index higher than that of the liquid medium ($n_{bac} > n_0$), the bacterium appears to be darker under phase-contrast microscope as shown in Figure 3.2a. Once the refractive index of the liquid medium is

equal to that of the bacterium ($n_{bac} = n_0$), the bacterium appears to be invisible as shown in Figure 3.2b. When the external liquid medium has a higher refractive index ($n_{bac} < n_0$), the bacterium appears to be brighter as shown in Figure 3.2c. While Figure 3.3 displays recent experimental results of an *E. coli.* immersed in a medium with the same three refractive index arrangements like what illustrated in Figure 3.2.

The optical path difference (OPD) experienced by the light can be expressed as

$$OPD = (n_{bac} - n_0) \cdot t_{bac} \qquad 3.3$$

where n_{bac} and n_0 are the refractive indices of the bacterium and the liquid medium respectively, and t_{bac} is the thickness of the bacterium.

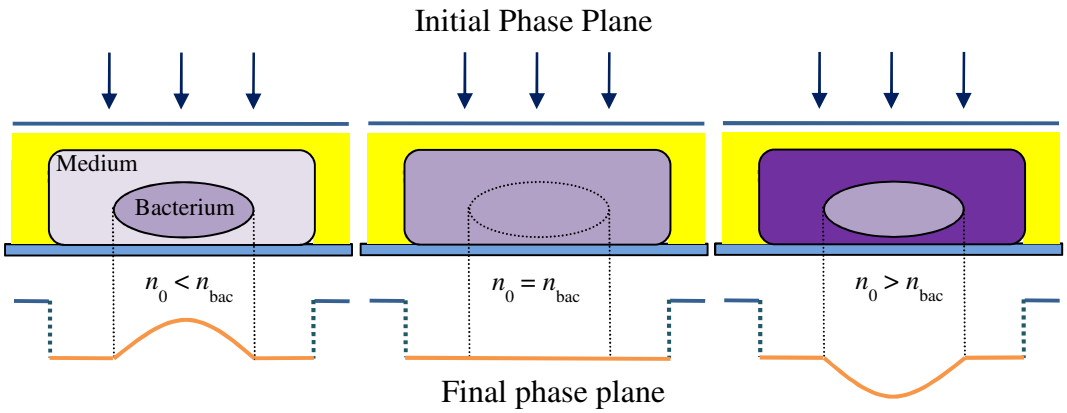

Figure 3.2 Schematic illustration of the phase changed images by a positive-mode phase contrast microscope. When light passes through the bacterium immersed in a medium with refractive index (a) lower than; (b) the same as; and (c) higher than the one of the bacterium.

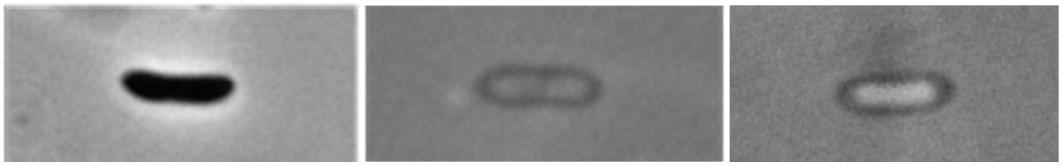

$n_0 < n_{bac}$ $n_0 = n_{bac}$ $n_0 > n_{bac}$

(a) (b) (c)

Figure 3.3 Experimental phase contrast images with a positive mode phase contrast microscope for a single *E. coli*. When *E. coli*. is immersed in a liquid medium with refractive index (a) lower than; (b) the same as; and (c) higher than the one of the bacterium.

Other applications of the Refractometry of single living cell

In addition, other biophysical parameters besides effective refractive index, such as dry mass and wet mass of single living cell can also be measured [2]. The mass density of a cell is defined as

$$\rho = \frac{n-n_0}{\alpha} \qquad 3.4$$

where n is the refractive index of a cell or that of a protein solution and α is the specific refractive increment approximately being 0.185 ml/g since it was demonstrated that α is nearly independent of intracellular composition of the cell or protein concentration and species, [2, 9, 80]. This correlation is typically applied

to a cell composed of mostly protein. Based on this model, ρ could be taken as the mean dry mass density of the cell. Therefore, the dry mass, wet mass and total mass of the cell can be expressed as

$$M_{dry} = \rho V \quad 3.5.1$$

$$M_{water} = \rho_0 V \quad 3.5.2$$

$$M_{cell} = M_{dry} + M_{water} \quad 3.\ 5.3$$

where $V = (4\pi/3)(l_c^3/8)$ is the cell volume, l_c is the cell thickness and ρ_0 =1 g/ml is the density of water. Cell refractive index and cell mass have been reviewed intensively for various applications such as in hematology and cancers in chapter 2.

3.2 Design of a Microfluidic Immersion Refractometer

An innovative microfluidic immersion refractometer is designed for obtaining the biophysical signatures of a single waterbourne bacterium. Both its morphologies such as size and shape, as well as refractive index are studied. The main features of the proposed microfluidic platform consists of (1) multiple sites for single bacterium trapping, which enable parallel measurements to achieve higher throughput, and (2) a liquid micromixer, which allows efficient refractive index deviation of the surrounding medium. The microfluidic chip comprises of an array of trapping sites to ensure simultaneous trapping of 50 bacteria for measurement, extendable up to hundreds. The refractive index

of the bacteria is measured by the null-method of phase contrast imaging via the immersion refractometry [2, 9, 80]. In this research, three different species of bacteria are investigated, which are *Escherichia coli* (*E. coli)*, *Shigella flexneri* and *Vibro cholera*.

3.2.1 Design of Microfluidic Chip

The optofluidic imaging system entails of a microfluidic chip to manipulate bacterial samples and change the liquid medium, combined with a phase-contrast microscope, to realize immersion refractometry. Figure 3.4 shows the schematic illustration of the microfluidic chip with a trapping microchamber and an integrated micromixer. The microchannels are filled with bacterial-containing medium solution. Several bacteria are trapped in the sample trapping area with an array of trapping sites. Each trapping site has a U-groove structure with a small gap of 500 nm [83]. The trapping site can trap any sample with a physical size larger than 500 nm up to approximately 20 μm. Once the bacteria are being trapped in the trapping microchamber, the surrounding liquid medium is tuned from low to high refractive index by mixing two different liquids using the integrated micromixer. At a specific refractive index, the trapped bacteria appeared to be invisible, i.e. the liquid medium and the bacteria have the same refractive index. The refractive index of the bacteria can be determined by measuring the refractive index of the liquid medium.

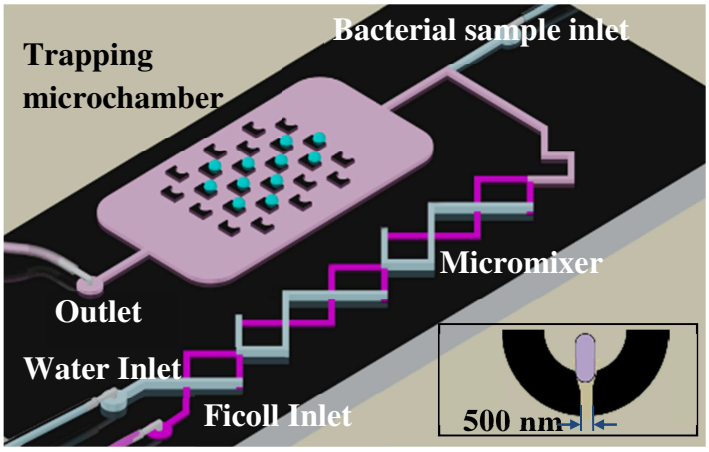

Figure 3.4 Schematic illustration of the microfluidic chip for biophysical measurements of single bacterium. Inset shows one trapping structure with a gap of 500 nm.

3.2.2 Micromixer for Efficient Mixing

In rapid immerging optofluidic and microfluidic devices, one important function is mixing of liquid media at micro-scales suitable for lab-on-a-chip systems for biological detections and manipulation processes [70]. It is considerably hard to mix liquid media uniformly at micro-levels. To achieve efficient liquid mixing, two important factors to be considered are (1) the Reynolds number and (2) liquid viscosity. At low Reynolds number, the liquid flow is laminar and mixing is negligible. On the other hand, viscous liquids are harder to be mixed. Therefore, precisely designed micromixers are required to

improve the mixing of liquids. Such micromixers are categorized into passive mixers and active mixers. Passive mixers use channel geometry to stir liquids, increasing the mixing interface. On the other hand, active mixers use external sources to blend the liquids. Passive mixers normally use zigzag, rotation or twisted microchannels that have patterned indentations using fluid lamination or applying surface tension [84]. They are time independent and have periodic structures. The flow in each mixer unit is stable and invariant.

In order for passive mixers to boost mixing in laminar flow, it must generate chaotic advection by using channel geometry. A two-layer structure is used for the micromixer, which is more effective than a single-layer mixer for liquid medium manipulations such as widening, splitting and recombination as shown in Figure 3.5. The mixer consists of three-dimensional "X-shaped" crossing channels. The slanted channels have an angle of 45° with the principle axis of the mixer and are perpendicular with each other. The channels are arranged in a periodic manner. The two-layer channels first go across each other at the cross-section AA′. In section BB′, the base-layer channel drives the fluid to the top layer through rotation and the top-layer channel turns the fluid by 90° in the same plane. Then, the two channels meet symmetrically at section CC′ and guide the fluid to the base layer. Section DD′ is similar to section BB′, and the difference is that the two side channels are inter-converted. From section CC′ to DD′ is the first half cycle. The second half cycle has similar structures, except that the slanted channels turn in the opposite direction in an attempt to reduce

the isolated fluid volumes. The channel depth of the different layers is 150 µm and the channel width is 300 µm.

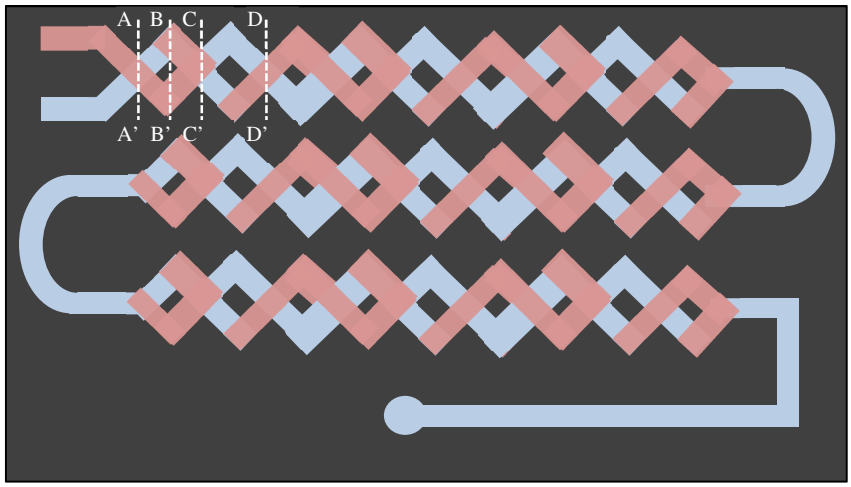

Figure 3.5 Schematic illustration of micromixer.

Figure 3.6 shows the simulation results of the micromixer using COMSOL Multiphysics simulation tool. The simulated flow comprises of the following patterns at different cross sections. In section AA′, as the two channels cross each other, it forms a hyperbolic parabola flow outline. When the two flow streams converge in the crossing section, each of the flow streams is split along the diagonal *x* into two thinner ones that go opposite directions along the diagonal *y*. In section BB′, there are two branches of flow streams. It shows that the winding of the channel in the same layer does not carry much impact, and the flow streams are kept in parallel to the channel wall. In the other branch channel, the flow streams are focused from the bottom layer to the top layer

with rotation, and realigned. In section CC′, rotation occurs when the two flow streams meet in the top layer and are steered to the bottom-layer. The left flow stream rotates clockwise while the right flow stream rotates anticlockwise. Therefore, the flow stream positions on the mixer cross-section are further changed. After section CC′, the flow streams simply continue to repeat the above-mentioned three flow patterns, starting at section DD′.

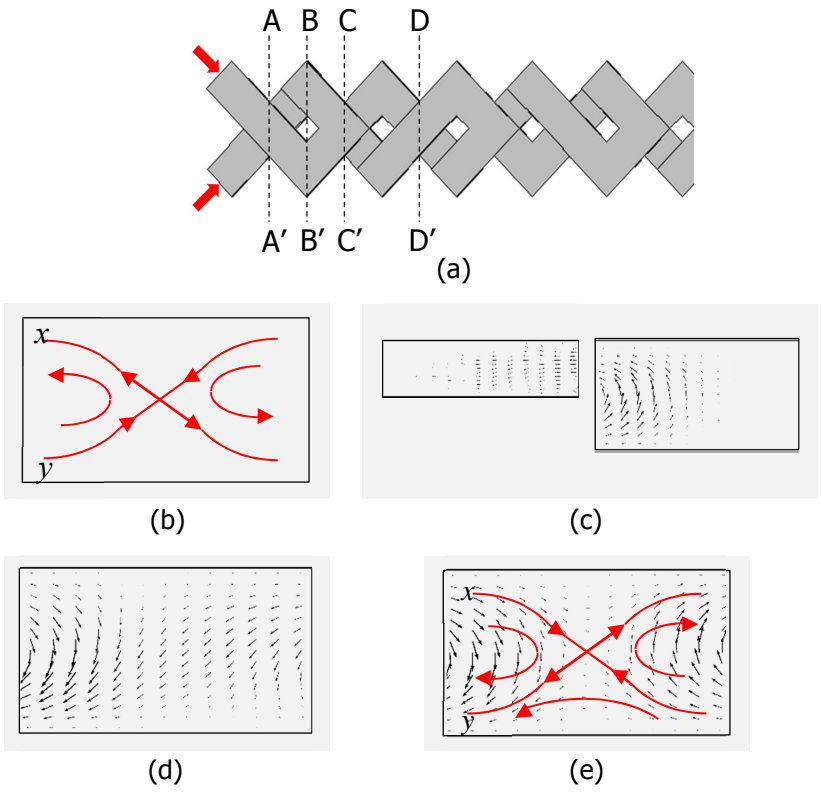

Figure 3.6 Simulation results of the micromixer. (a) Configuration of the micromixer. Velocity vector plane at sections (b) A-A′; (c) B-B′; (d) C-C′; and (e) D-D′.

3.3 Fabrication, Experimental Setup and Sample Preparation

3.3.1 Fabrication Processes

Polymers are the most useful materials for biochips as they are easy to fabricate and replicate, biocompatible and low cost. There are several different types of polymers commonly used for microfluidic device fabrication, such as polydimethysiloxane (PDMS), polymethyl methacrylate (PMMA), polystyrene (PS) and polycarbonate (PC). These polymer materials offer tremendous optical (visible light) transparency, chemically inert, biocompatible, high temperature and dimensional stability. One of the most common fabrication processes is soft lithography or molding technology, which consists of two main steps, i.e. the fabrication of a master by using silicon, glass or hard polymer wafer and the replication of pattern to the polymer.

The designed microfluidic chip used in the optofluidic platform is made of PDMS with the fabrication process being shown in Figure 3.7. The fabrication of a microfluidic chip involves three main steps; master patterning, molding and bonding. First, the master is fabricated on the silicon wafer using the lithography method with SU-8 development. A layer of SU-8 (SU8 2025) is spun-coated on the silicon substrate at 500 rpm for 5 seconds and the speed is then increased to 2,000 rpm for 30 seconds to obtain a thickness of about 50 µm

photoresist coat. Next, the wafer is placed on a flat surface for 2 hours to flatten and smoothen the SU-8 layer. Then, the wafer is put on a hotplate for soft-baking at 65°C for 15 minutes and, subsequently, at 95°C for 30 minutes. The photoresist layer is exposed to UV light under a glass mask with the designed patterns using a mask aligner machine at 24 mW/cm^2 for 8 seconds. The exposed SU-8 material is cross-linked. After that, the exposed wafer is post-baked at 65°C for 1 minunte and at 95°C for 3 minuntes. The post exposure bake (PEB) is used to catalyze the cross-linking process of the exposed SU-8. Finally, the wafer is immersed into the SU-8 developer solution for 6 minutes. The developed SU-8 structures are attached onto the wafer and the master is ready.

The second step involves the curing of the PDMS elastomer when being poured onto the master to obtain the replica. PDMS elastomer (Sylgard 184) is a two part heat curing material. It consists of a base and a curing agent. First, they are pre-mixed at the ratio of 10:1. Then, the mixture is degassed in a desiccator under vacuum. Subsequently, the PDMS is cured in an oven for 1 hour at 75°C. The curing temperature and the ratio of the curing agent define the hardness of the PDMS. After curing, the PDMS sheet can be peeled off from the master. It is worth to note that the master surface is firstly salinized to avoid the PDMS sheet sticking to it, by being submerged in toluene for 5 hours and several drops of dichloromethylsilane (DMS) is dropped into the solvent.

Lastly, the replica will be peeled off from the master and bonded with a PDMS-coated coverslip to form the microfludic chip with sealed microchannels. To bond the PDMS microfluidic chip, the PDMS slab and the PDMS-coated coverslip are meticulously cleaned with ultrasonic cleaner and isopropanol (IPA). Then, it is dried under a moderate stream of nitrogen gas. As a PDMS surface has very low surface energy and is hydrophobic, it is necessary to change the surface features of the PDMS to increase its surface energy. Both surfaces are oxygen plasma treated with a handheld corona treater to increase the surface energy so as to improve the adhesion qualities of the PDMS surfaces, as well as to change the surfaces from hydrophobic to hydrophilic for easy flow of the sample liquid. After surface treatment, the two surfaces are taken to conformal contact and put aside for one day such that an irreversible bonding is formed.

Some silanol groups are also created on the PDMS surface and sidewall due to the exposure of oxygen plasma. This provides an electroosmotic effect on the sidewalls of the microchannels of the PDMS.

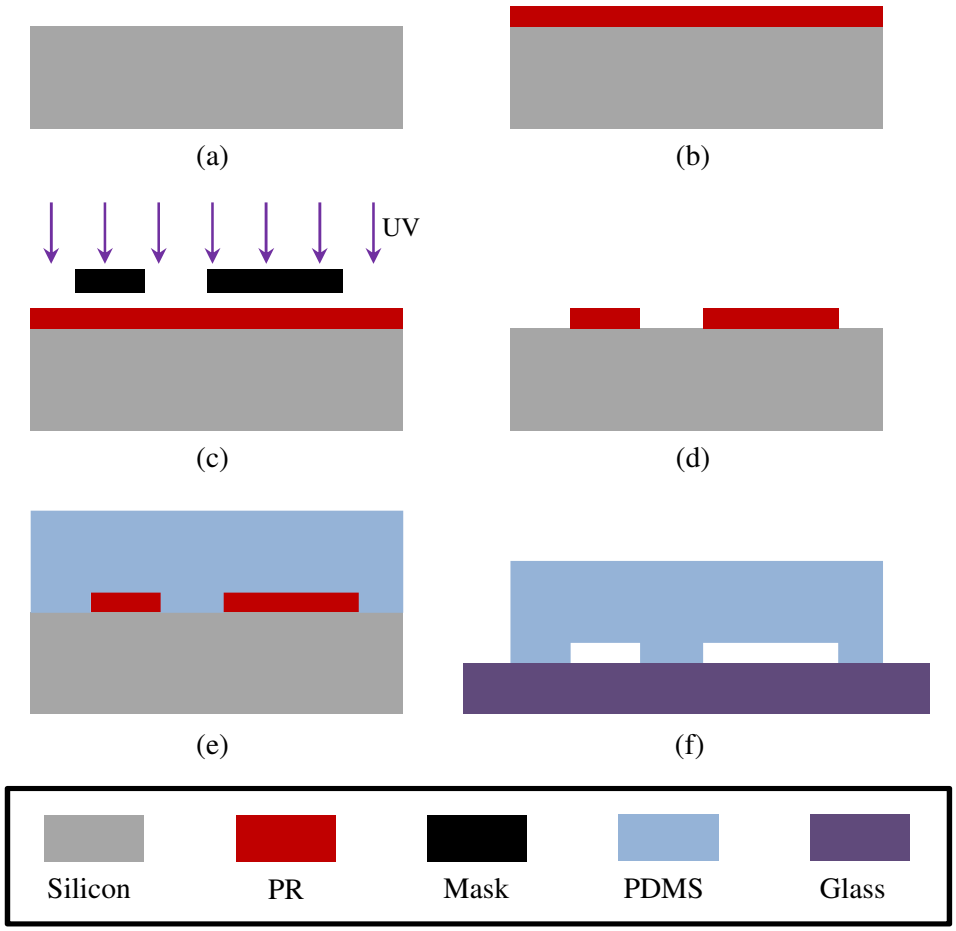

Figure 3.7 Illustration of the fabrication process flow. (a) Silicon wafer; (b) photoresist (PR) coating; (c) lithography exposure; (d) photoresist develop; (e) PDMS molding; and (f) chip bonding.

3.3.2 Experimental Setup and Image Processing

The optofluidic chip is placed on an inverted microscope (NIKON, Eclipse Ti) and a 60× objective lens is used to image the trapped bacteria. To tune the refractive index of the external medium, Ficoll solution is selected to mix with DI water because of its low osmotic pressure and biocompatibility [85]. Bacterium samples, DI water and Ficoll medium are injected into the chip using high precision syringe pumps (New Era Pump Systems Inc, NE-1000) to allow them to flow through the inlets. The phase contrast images are taken by a digital CCD camera (NIKON, DS-Ri1) for measuring the biophysical properties of the bacterium samples. The image processing software ImageJ is used to analyze the width, length and aspect ratio (length/width) of each bacterium. For the refractive index measurement of each bacterium, the refractive index of the medium is varied with small increment by changing the ratio of the flow rates of the two mixing solutions. The various refractive indices of the flowing medium are repeatedly measured using a hand-held refractometer (Atago, PA-RI). The intensity profiles along a line cross the same flow channel in the captured phase contrast images are are obtained using the software of ImageJ. The contrast of images is enhanced and preudo-colored during image processing using ImageJ.

3.3.3 Protocol for Bacterium Preparation

In the experiments, three different species of bacteria are studied, i.e. *E. coli*, *Shigella flexneri* and *Vibrio cholera*. For *E. coli*, Luria-Bertani (LB) broth medium is used as the culture medium. LB broth medium is prepared by mixing thoroughly 25 g of broth powder (Sigma-Aldrich, L3522) in one liter of deionized (DI) water. On the other hand, nutrient broth medium is used for *Shigella flexneri* and *Vibrio cholera*. Nutrient broth medium is prepared by mixing thoroughly 13 g of broth powder (Sigma-Aldrich, 70122) in 1.00 liter of DI water. Both media are sterilized and heated with a benchtop autoclave machine (Tuttnauer, 2340EKA) at 121°C for 15 min.

To thaw the vial of frozen bacteria, which was removed from the liquid nitrogen freezer, it was left in a 37°C water bath (YIHDER, BT-150D) with moderate agitation. Then, the vial is removed from the water bath and decontaminated with 70% ethanol solution. After thawing, the content is transferred to the prepared growth medium (10 mL). Once the bacteria have been fully cultured, 10% of the culture is used in the experiment while the remaining is frozen for future usage by cryopreservation. For storage, the bacterium is frozen, and 10% glycerol (Invitrogen 15514011) is added to culture medium. Glycerol is prepared at twice the final concentration for freezing and mixed with an equal volume of cell suspension whereby 1.0 ml of

bacterial suspension is aliquoted to each vial and sealed. The bacteria cells are equilibrated in the medium at room temperature for 40 mins. The vials are placed in a temperature rate-controlled freezing chamber and stored in a -70°C freezer (SANYO, MDF-C8V1) for at least 24 hours before being transferred to liquid nitrogen tank (Thermo Scientific, 807). The bacteria to be used in the experiment are transferred from the culture medium to tap water and incubated for 24 hours before the biophysical measurements are performed to mimic the conditions of bacteria in drinking water.

3.4 Experimental Results & Discussions

3.4.1 Mixing Efficiency of Micromixer

DI water and Ficoll solution (Sigma-Aldrich, F4375) with refractive indices of 1.3326 and 1.4651 respectively, are used in the experiment. Therefore, the refractive index of the liquid medium can be tuned from 1.333 up to 1.465 by changing the ratio of the flow rates of DI water and the Ficoll solution. As shown in Figure 3.8a, DI water and fluorescein-premixed Ficoll solution are injected to the microchannel at different ratio of flow rates to determine and illustrate the mixing efficiency of the chaotic mixer. The mixing efficiency is measured by monitoring the fluorescence intensity at the end of the chaotic mixer. When the flow rate of the Ficoll solution is changed from 20 to

50 μL/sec, the measured fluorescence intensity is increased remarkably. Figures 3.8b to 3.8c show three typical fluorescence images across the microchannel, with intensity profiles of fluorescence images (dashed line in Figure 3.8. The intensity profile shows that the liquids are well mixed with a variation lower than 1%, which verifies the accuracy and precision of the microfluidic immersion refractometer. The refractive index of the liquid medium as a function of the flow rate ratio (Q_{ficoll}/Q_{water}) is illustrated in the graph of Figure 3.10. When the microchannel is filled with DI water, the refractive index is 1.3326. Subsequently, the refractive index is increased at a rate of 0.029 RIU by increasing the flow rate of the Ficoll inlet. At the point where the flow rate ratio is 2.5 and the refractive index of the external medium is 1.4152, the increment rate is reduced to 0.004 RIU.

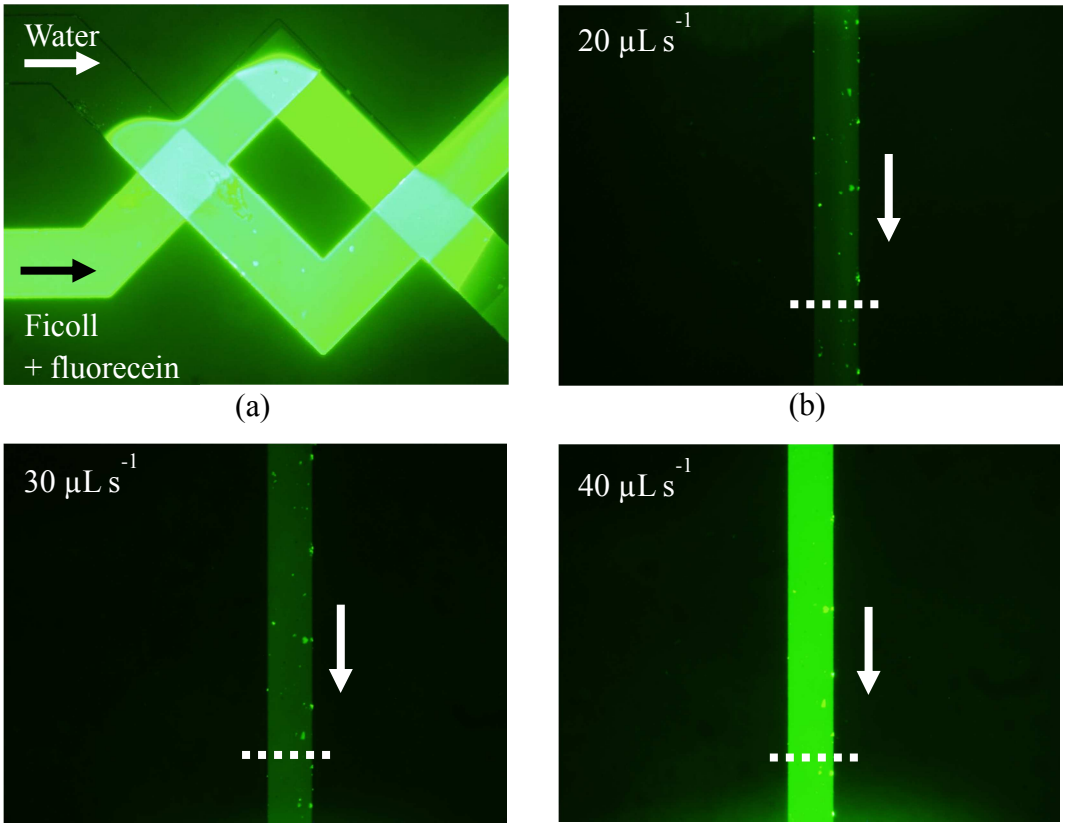

Figure 3.8: Measurement of mixing efficiency of the chaotic micromixer by mixing DI water and Ficoll + fluorescein solution with different ratios of flow rates.

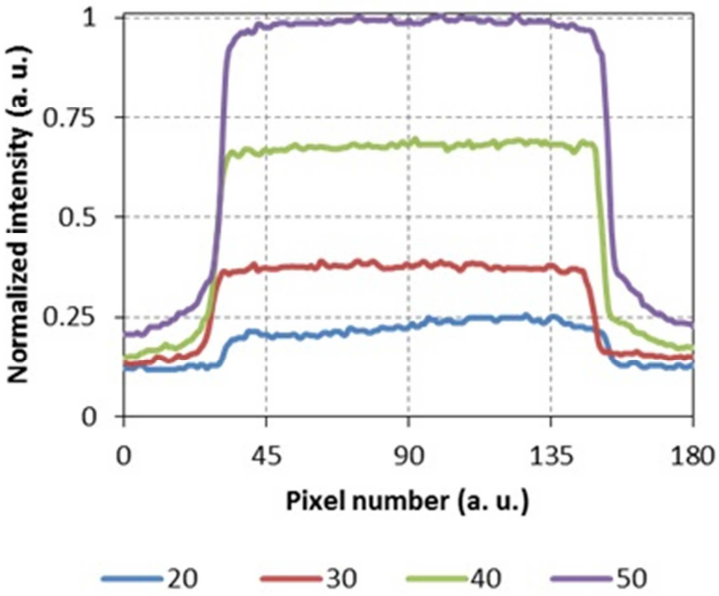

Figure 3.9 Fluorescent intensity profiles across the microchannel with the fixed flow rate of DI water of 10 μL/s and varied flow rates of 20, 30, 40 and 50 μL/s respectively for the Ficoll + fluorescein solution.

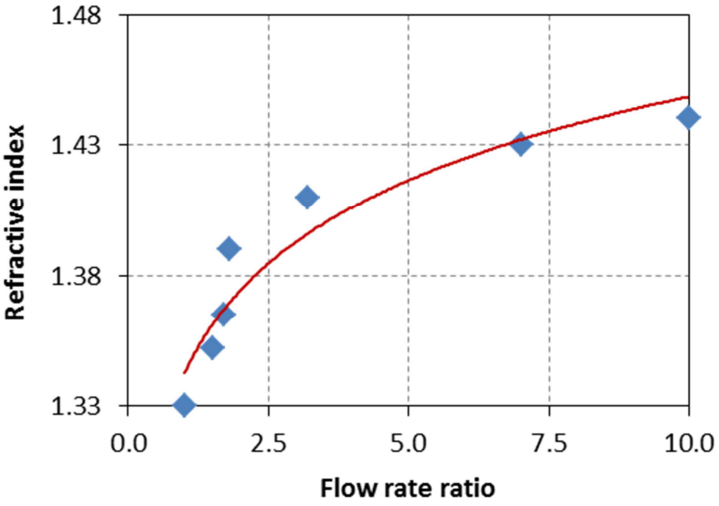

Figure 3.10 Tuning of the refractive index of the liquid medium by varying the ratio of flow rates between the DI water and the Ficoll + fluorescein solution.

3.4.2 Characterization of the Immersion Refractometer

The optofluidic immersion refractometer is characterized by using a PDMS (Dow Corning, Sylgard 184) testing structure in a microfluidic chip and its phase contrast images when the liquid medium is changed from 1.410 to 1.414 as shown in Figure 3.11(a) as A, B, C. D and E respectively. In the image E, the PDMS structure indicated by the dotted curve becomes invisible. For each phase-contrast image, the relative intensity is obtained by dividing the average pixel intensity of the PDMS testing structure with the average pixel intensity of the surrounding liquid medium. The linear relationship between the relative intensities and the refractive indices of the media is confirmed and shown in Figure 3.11(b). When the liquid medium has lower refractive index as compared to the one of the PDMS material, the PDMS structure appears to be darker and concave. On the other hand, when the medium has higher refractive index, the PDMS structure appears to be brighter and protruding. Based on the interpolation of the measured data, the PDMS testing structure has a refractive index of 1.412, which matches with previous report [86].

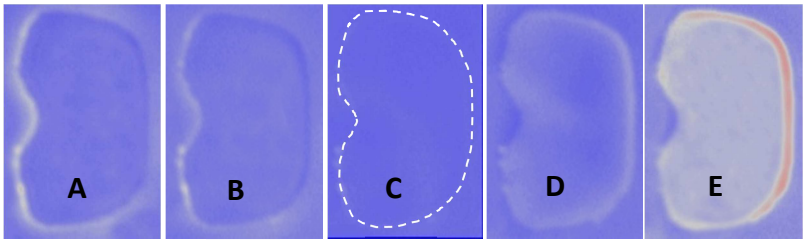

(a)

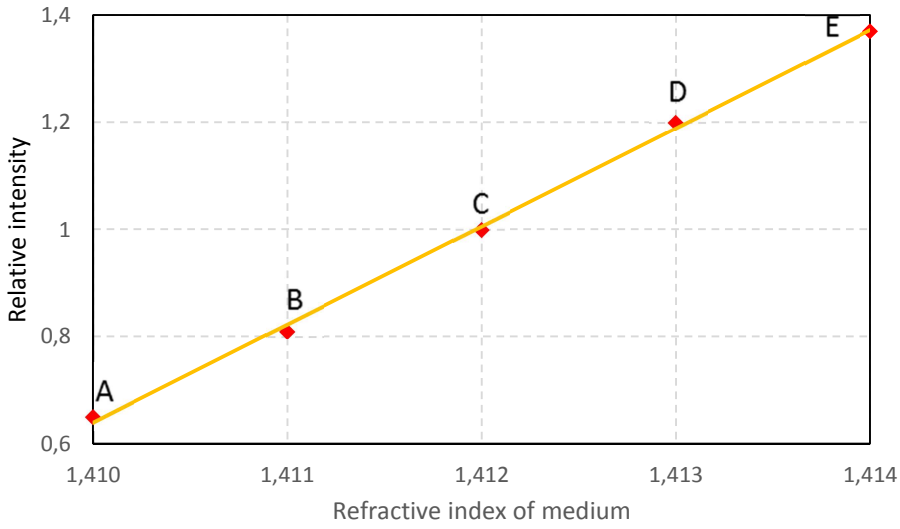

(b)

Figure 3.11 (a) The positive-mode phase contrast images of A, B, C, D and E are corresponding to medium's refractive indices of 1,410, 1.411, 1.412, 1.413 and 1.414 respectively; (b) Characterization of the optofluidic immersion refractometer by measuring the refractive index of PDMS testing structure shown in images A, B, C, D, and E.

3.4.3 Single Bacterium Biophysical Measurements

In the experiments, a sample size of 250 for each bacterium species is measured and statistically characterized with results showing in Figure 3.12. Both *E. coli* and *Shigella flexneri* have similar morphology whereby they are both rod shape bacteria. According to these results, *E. coli* has a mean length and width of 2.83 and 0.86 μm, respectively, and a mean aspect ratio of 3.87. On the other hand, *Shigella flexneri* has a mean length and width of 2.74 and 0.77 μm, respectively, and a mean aspect ratio of 3.48. *Vibrio cholera* is relatively smaller as compared to the two and has a shape of comma. *Vibrio cholera* has a mean length and width of 1.21 and 0.43 μm, respectively, and a mean aspect ratio of 2.84. Figure 3.13 shows the effective trapping of the E. coli in the trapping sites where the contrast is enhanced by image processing.

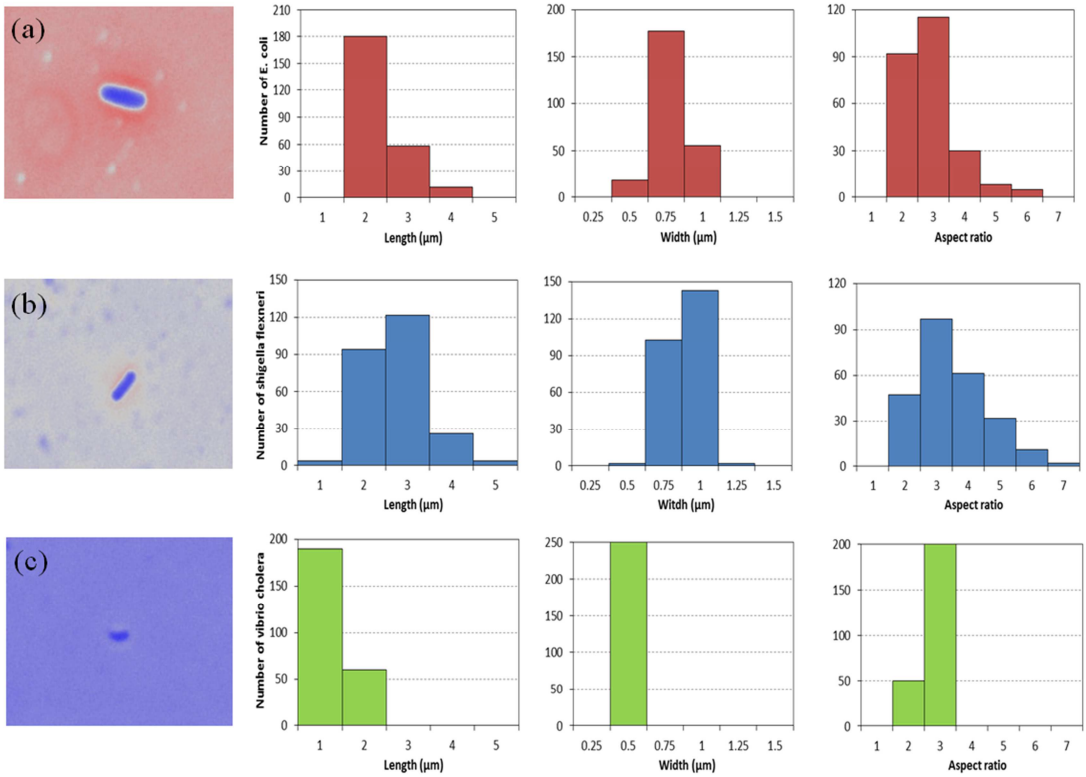

Figure 3.12 Morphological measurements of (a) *E. coli*; (b) *Shigella flexneri*; and (c) *vibrio cholera.* Their phase contrast images are shown in the far left of the row.

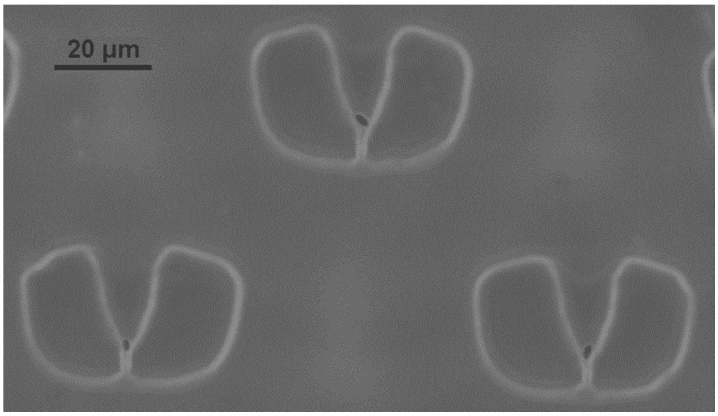

Figure 3.13 Trapping of *E. coli* in the trapping site (Contrast enhanced by image processing).

Figure 3.14 shows the pixel intensity analysis for single *E. coli* bacterium by varying the refractive index of the medium. The relative intensity profile is divided by the average intensity of an area of the medium. When the relative intensity is lowers than 1, it means the refractive index of the medium is lower than that of the bacterium, and vice versa. The matching refractive index of 1.388 occurs when the relative intensity is about 1, which is the effective refractive index of the *E. coli*. Such a value is comparable with the value reported using light scattering technique (1.390) [27]. By the SAME data processing for the intensity profile, the measured results of *Shigella flexneri* are shown in Figure 3.15, its effective refractive index is about 1.422. In addition, *Vibrio cholera* is measured and analyzed with its effective refractive index being found at 1.365.

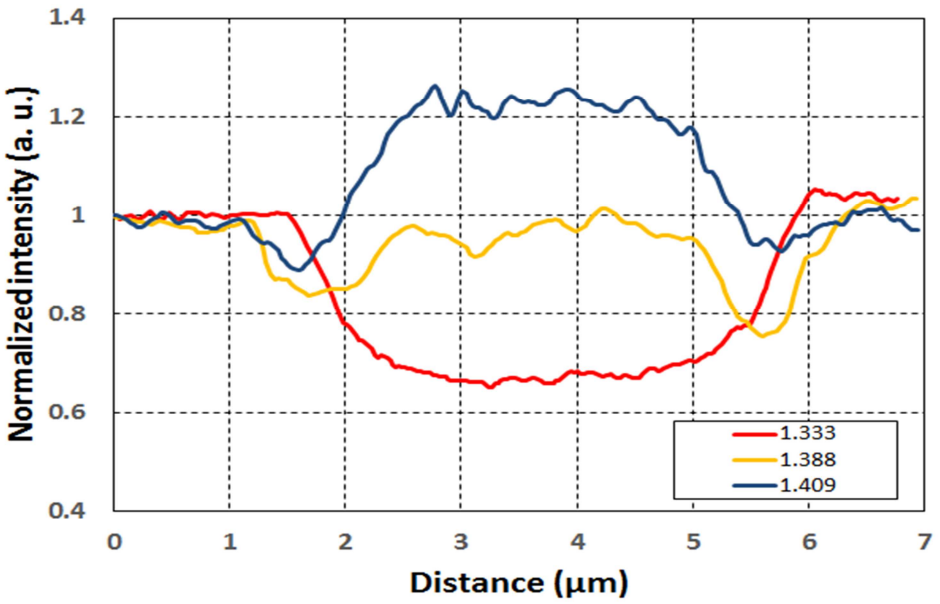

(a)

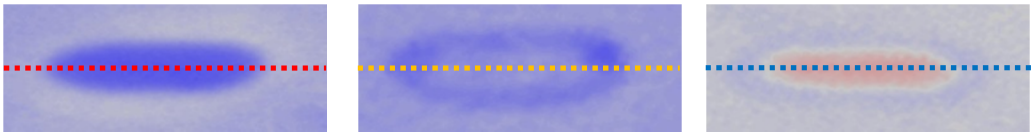

1.333 1.388 1.409

(b)

Figure 3.14 (a) Pixel intensity analysis of *E. coli* when the liquid medium is tuned from low to high corresponding to the images shown below; and (b) Phase contrast images of *E. coli* appears to be darker, nearly invisible and brighter when the refractive indices of the media being 1.333, 1.388 and 1.409 respectively.

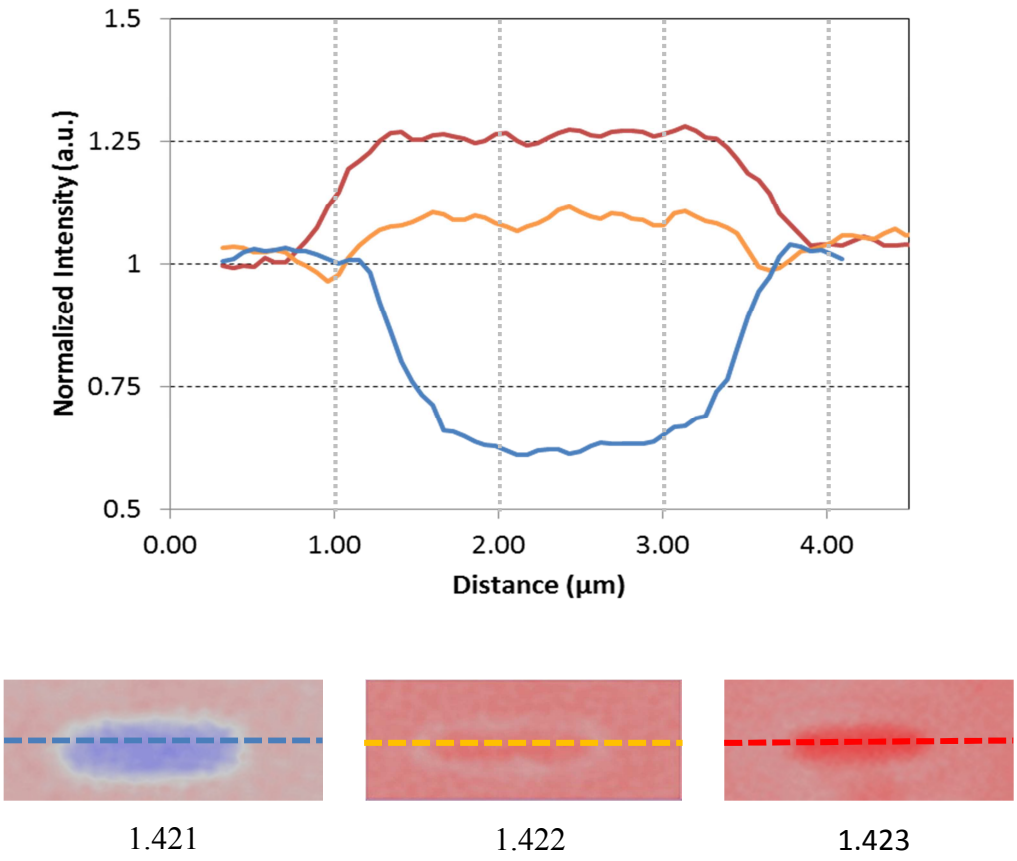

Figure 3.15 Pixel intensity analysis of *Shigella flexneri* when the external medium is tuned from low to high. Phase contrast images of *Shigella flexneri* appears to be darker, nearly invisible and brighter when the refractive indices of the media being 1.421, 1.422 and 1.423 respectively.

The statistical results of the morphological and effective refractive index measurements based on the mean and standard deviation of the three different species of bacteria are summarized as shown in Table 3.1. For morphology, *Vibrio cholera* has a relatively smaller size and is comma in shape as compared to *E. coli* and *Shigella flexneri* that are in rod shape. For effective refractive index, *Vibrio cholera* has the lowest effective refractive index (1.365) as compared to *E. coli* (1.388) and *Shigella flexneri* (1.422). It is concluded that these three different species of bacteria can be differentiated based on their effective refractive index measured at least at the resolution of 5×10^{-3} RIU.

Table 3.1 Biophysical measurements of three different bacteria (N = 250)

Bacteria	*E. coli*	*Shigella flexneri*	*Vibrio cholera*
Length (μm)	2.83 ± 0.41	2.74 ± 0.67	1.21 ± 0.35
Diameter (μm)	0.86 ± 0.10	0.77 ± 0.10	0.43 ± 0.09
Aspect Ratio	2.50 ± 0.80	3.48 ± 0.80	2.84 ± 0.80
Refractive Index	1.388 ± 0.005	1.422 ± 0.005	1.365 ± 0.005

3.4.4 Discussions

The sensitivity of the microfluidic system depends on two criteria: (1) the phase shift detection limit of the phase-contrast microscopy, and (2) the resolution of the commercial liquid refractometer used to measure the refractive index of the liquid medium. For a non-absorbing phase plate, it is possible to achieve a detectable phase change of less than $\lambda/100$ with ease. The wavelength used for the detection of bacteria is 514 nm, while the thickness is approximately 1 μm. Hence, the minimum detectable refractive index difference, i. e. the resolution of the system, is approximately 0.005. The phase shift detection limit of the phase-contrast microscopy depends on the light absorption of the phase plate, in which $\lambda/1000$ can be achieved with heavily absorbing phase plates. The sensitivity can be theoretically improved to 0.0005 [1]. The refractive index of the external medium is measured by using a refractometer (Atago, Pal RI) with a resolution of 10^{-4}, which is sufficiently precise such that it is not the limiting factor in the measurement. However, when it is calibrated with another high end Abbé refractometer, large discrepancy is shown that the hand-held refractometer has errors at the 10^{-3}.

Bacteria have a relatively small size that makes it difficult to determine the refractive index inhomogeneity within the bacteria, which is the limitation of the microfluidic immersion refractometer. Although such inhomogeneity can be

seen in larger samples, such as mammalian cells, it is difficult to quantify the exact refractive index value of various parts of the cell. A more sophisticated model and technique is required.

Based on the size, shape and refractive index, the biophysical signature of the bacteria can be used as an alternative method for waterborne bacteria identification in treated water facilities. Even though biophysical properties may be unable to distinguish between different strains of *E. coli*, the technique has high potential and capability to identify different species of bacteria. It also delivers a rapid, highly-automated detection method of the presence of *E. coli* in water samples, which is an indicator of fecal pollution and possible presence of enteric pathogens.

3.5 Summary

The originality of this work is concentrated on development a microfluidic immersion refractometer to measure the biophysical signature of single waterborne bacteria, i.e. size, shape and refractive index. In the microfluidic immersion refractometer, a trapping microchamber with an array of trapping sites is designed to trap single bacteria simultaneously. In addition, a micromixer is employed to mix the two liquid solutions (DI water and Ficoll solution) and tune the refractive index of the liquid medium smoothly. By using the microfluidic immersion refractometer, three bacteria species are measured namely *E. coli*, *Shigella flexneri* and *Vibrio cholera*. The refractive indices of each bacterium species is 1.388,

1.422 and 1.365 respectively. While *E. coli* has a mean length and width of 2.83 and 0.86 µm. The microfluidic immersion refractometer provides an efficient method to measure and build up a database of the biophysical signature of different bacterium species. This modernizes the drinking water detection technology and has high potential to facilitate label-free on-site detection of waterborne bacteria. The detection of single waterborne bacteria based on their biophysical signature is especially beneficial pertaining to the drinking water industry.

Chapter 4 Refractive Index Mapping of Single Cell and Lipid Droplets using Optical Diffraction Tomography

This chapter introduces an optical diffraction tomography with fluorescence imaging for the measurement of refractive index map/distribution of single cell. Section 4.1 introduces the principles of Mach-Zehnder interferometry, phase shifting interferometry and diffraction tomography. Section 4.2 introduces biology of intracellular lipid droplets and their functions and importance. Next, section 4.3. reports the design of the optical diffraction tomography system integrated with fluorescence imaging and the methodology to obtain a refractive index map of a single cell from a large number of angular-scanned images. While section 4.4, presents the experimental preparation, system characterization, intracellular organelle measurements and the measurement results of lipid droplets in 3T3-L1 cells under fatty acid stimulation. Lastly, section 4.5 concludes the chapter with future potentials of lipid droplet investigation in biological and biomedical studies.

4.1 Optical Diffraction Tomography and Comprised Techniques

Optical diffraction tomography is mainly comprised of Mach-Zehnder interferometer, phase shifting interferometry, phase diffraction tomography and reconstruction algorithm for 3D refractive index or phase map/distribution. To understand the functions of different optical configurations clearly, their principles are briefly described in the following subsections.

4.1.1 Principle of Mach-Zehnder interferometer

Mach-Zehnder interferometer is a simple but very important conceptual design popularly adapted by various sensors and diagnostic devices used in photonic, integrated optics and biochemical applications [88]. It is popularly incorporated as electro-optic modulators in various fiber-optic communication and monolithic integrated circuits applications [89]. Because of its relative large and freely accessible working space and flexibility of fringe locations, it is also suitable for aerodynamics [90] and heat transfer to measure density, pressure and temperature changes in gases or liquids in flow [91]. It is also used to study one of the most counter-intuitive predictions of quantum mechanics, the phenomenon known as quantum entanglement [92-94].

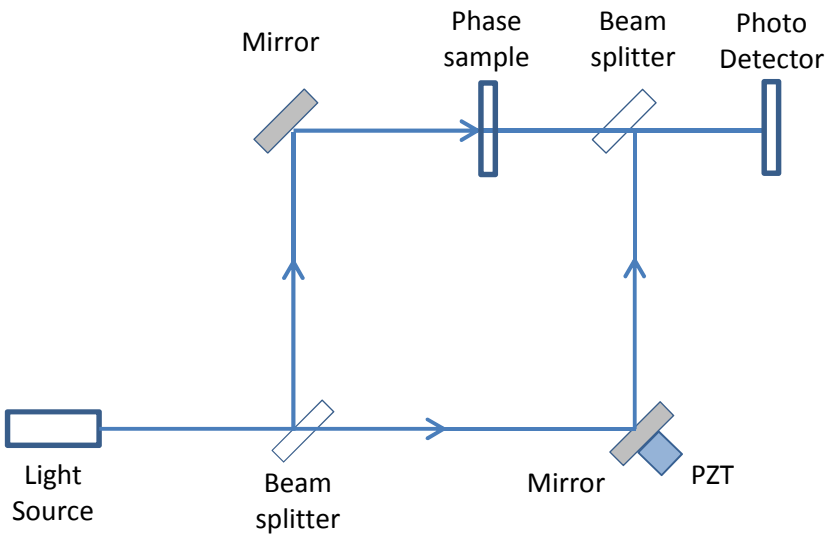

Figure 4.1 Schematic layout of a Mach–Zehnder interferometer

A schematic layout of a Mach–Zehnder interferometer is illustrated in Figure. 4.1. The light from the optical source, such as a laser, is collimated and split into two beams with a non-polarized beam splitter. Both of them are reflected by mirrors and then combined by a half reflection and half transparent optical mirror/filter and eventually incident to the recording plane denoted as the *x*-*y* plane. The reference beams is assumed to be a planar wave, which hits the recording plane at its surface normal. Its complex amplitude field at the recording plane can be expressed by the harmonic wave equation as

$$U_r(x,\ y) = u_r\ exp(i\psi) \qquad 4.1$$

where u_r is the constant amplitude and ψ is a constant phase at all positions in the recording plane. The complex field of the object beam can be expressed in terms of the amplitude $u_o(x, y)$ and the phase $\varphi(x, y)$ distribution,

$$U_o = u_o\,(x,y)\exp[i\varphi(x,y)] = u_o\,(x,y)[cos\varphi(x,y) + i\,sin\varphi(x,y)] \qquad 4.2$$

Since most optical recording media are only responding to intensity but not amplitude or phase, the phase information has to be unveiled by intensity. In this case, the coherent linear addition of the two wavefronts forms a resultant complex field with its intensity being expressed as

$$I = u_r^2 + u_o^2(x,y) + 2u_r\,u_o\,(x,y)\cos[\varphi(x,y) + \psi] \qquad 4.3$$

Eq. 4.3 can be readily rewritten as

$$I(x,y) = A(x,y) + B(x,y)\,cos[\,\varphi(x,y) + \psi] \qquad 4.4$$

where $A(x,y)$ is the background intensity and $B(x,y)$ is the intensity modulation of the interference fringe pattern, both of them vary much slower compares to the cosine term, while ψ is simply considered as the phase difference of the two beams.

The ease of control and adding a phase-shifting module in the reference beam path without disturbing of the object beam makes Mach–Zehnder interferometry a popular configuration in holographic interferometry [88, 7].

4.1.2 Phase Shifting Interferometry

Phase-shifting concept for conventional holographic interferometry is originally introduced by Gabor and Goss [95]. With digital implementation, algebraic manipulation becomes much easier such that the technique has been adapted to many different areas. In the field of quantitative phase imaging, it serves as the main configuration for temporal modulations.

Phase shifting technology records a series of interferograms from a minimum of three frames to hundreds by changing the phase of the reference beam with respect to that of the object beam. The wavefront phase distribution is encoded in the irradiance variation, while the wavefront phase difference between the two interfering beams can be obtained by analysing the point-by-point irradiance of three or more interferograms with varying phase difference. However, phase values calculated with any phase shifting algorithms lie in the range of $-\pi$ to π, which is known as the principal value range. Such discontinuous distribution is called wrapped phase and is caused by the nonlinear reconstruction function. In order to recover the original phase values from the principal values, i.e. the wrapped phase distribution and the phase unwrapping, a classical signal processing algorithm is employed [96, 97] such that a continuous phase image/distribution can be extracted from the series of interferograms.

Practically, the set of interferograms, with phase delays in between, can be realized by either acousto-optic modulation (AOM) [7, 98], or translating a mirror in the reference arm with a piezoelectric transducer (PZT) component [6]. The latter is popularly employed and is shown in Figure. 4.1. In principle, its lateral resolution can maintain the resolution of the microscopic system. Based on Eq. 4.4, a phase delay δ is now generated by a PZT or AOM and added to the reference beam. For simplicity, the constant phase of ψ is omitted, and the shifted phase δ_i are used to represent the phase delay term of the reference beam in the intensity equations of the interferograms. From Eq. 4.4, a series of interferograms achieved by phase shifting can be obtained as

$$I_i(x,y) = A(x,y) + B(x,y)\cos[\,\varphi(x,y) + \delta_i\,] \qquad 4.5$$

where the subscript i = 1, 2, …, N is the frame index, and N is the total number of frames. $A(x,y)$, $B(x,y)$ and $\varphi(x,y)$ are the background intensity, intensity modulation, angular phase deference between the sample beam and phase shifted reference beam, respectively.

In early phase shifting studies and applications, the amount of phase shift is a known constant [99, 100]. Since there are only three unknown numbers in the interferograms equation, three interferograms are needed to obtain an analytical solution of the phase difference field distribution $\varphi(x,y)$. However, this limit

requires precise calibration and close-loop control of the phase shifter. Other researchers relax the requirement to arbitrary phase shift but known precisely [101], or arbitrary constants but equal steps [102, 103]. Both approaches need more interferograms to obtain the phase field. Later, such limitation is removed by defining the phase shifting to be unknown arbitrary and unequal phase steps using only three or four interferograms [104].

The phase measurements of the sample is within the (–π, π) interval, which is then numerically corrected to expand to larger interval, which is known as phase unwrapping. The Goldestein phase unwrapping concept is used to achieve the correct phase relative to the medium. In particular the advanced iterative algorithm (AIA) of Zhang and Han [105] was set on the basis of least squares estimation and iterative computation to extract the values of $A(x,y)$, $B(x,y)$, $\varphi(x,y)$, and δ_i accurately from the interferograms. These are affected by speckle noise intrinsic to all laser-based optical systems and dust or air perturbations in the beam paths.

4.1.3 Diffraction tomography

Optical diffraction tomography (ODT) is an interferometric technique that directly obtains the 3D refractive index distribution of an optically transparent sample, which is theoretically proposed by E. Wolf in 1969 [106] and geometrical interpreted by Dandliker and Weiss [107]. Therefore, ODT is very suitable for full-field investigations of live cells and other microorganisms. From late 70s, ODT technology has demonstrated its capability and significance with rapidly increased applications [108-111] especially for micro-scale biological samples, whose refractive index values can also be easily translated into various useful biophysical parameters such as protein concentrations and cellular dry mass.

ODT solves an inverse problem of light scattering from a weakly scattering object. It is analogous to X-ray computer tomography in which 3D absorption distribution is reconstructed by a back-projection algorithm. In ODT, 3D refractive index distribution of the sample is reconstructed from a large amount of 2D interferograms of the sample obtained by either scanning the sample with various illumination angles or rotating the sample itself. Both ODT and X-ray computerized tomography share the same governing equation of Helmholtz equation. Detailed principle and mathematical descriptions can be found in

Ref. [112, 113]. X-ray tomography is used here as a reference to explain the basics of ODT (Figure 4.2). X-ray is considered non-diffractive to an absorptive object. Under a plane wave with θ angle with respect to the x-axis, its projection intensity field is shown as the green doted profile along the line *t-t′*. By performing a Fourier transform, the frequency values profile is along the straight line B-B′ in the frequency domain as shown in the right of Figure 4.2. On the other hand, a visible light is diffractive when shines on a weakly scattering object. Light diffracted with its forward scattering field along the line t-t′ being depicted as the red solid profile. By Fourier transform, the frequency profile of the diffracted intensity field is now along a semicircular arc in the frequency domain.

Considering an inhomogeneous weakly scattering core-shell microstructure in Figure 4.3a and a homogenous microstructure in Figure 4.3b, both are in the same medium and illuminated by a single plane wave. The optical phase shifts and thus the projected optical field profiles are the same. Therefore it is clear that it is impossible to differentiate the two microstructures. A high resolution 3D map can only be reconstructed from a large amount of interferograms in different angles.

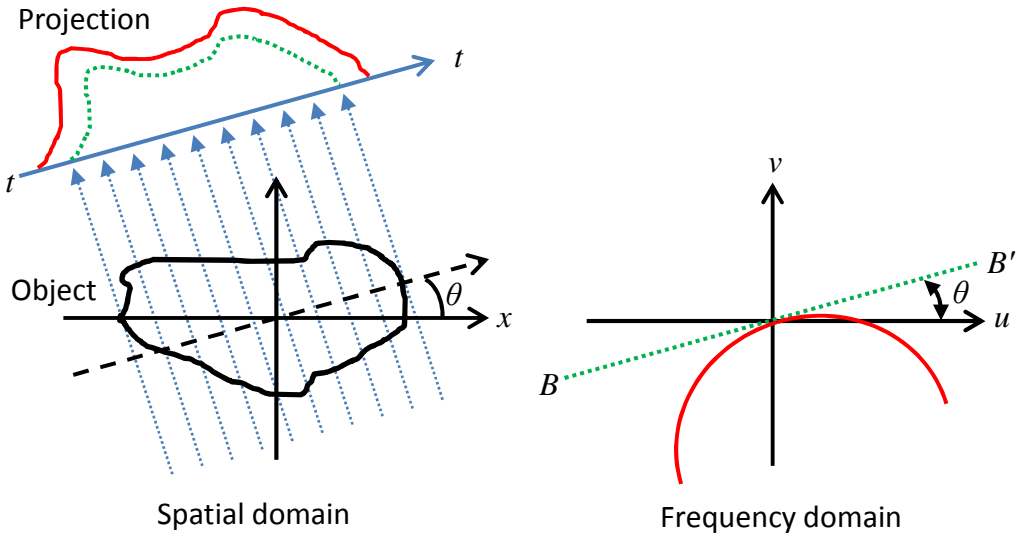

Figure 4.2 One weakly scattering object is illuminated by a plane wave. If it is an X-ray wave, the projection field profile along the *t*-*t*′ line is depicted as the doted profile. Its Fourier transform gives frequency values along the straight line *B*-*B*′ in the frequency domain. For optical plane wave, the projection forward scattering of the object has a diffraction profile with the solid curve. The Fourier diffraction theorem gives frequency values along a semicircular arc in the frequency domain for the intensity field along the *t*-*t*′ line in the spatial domain [112].

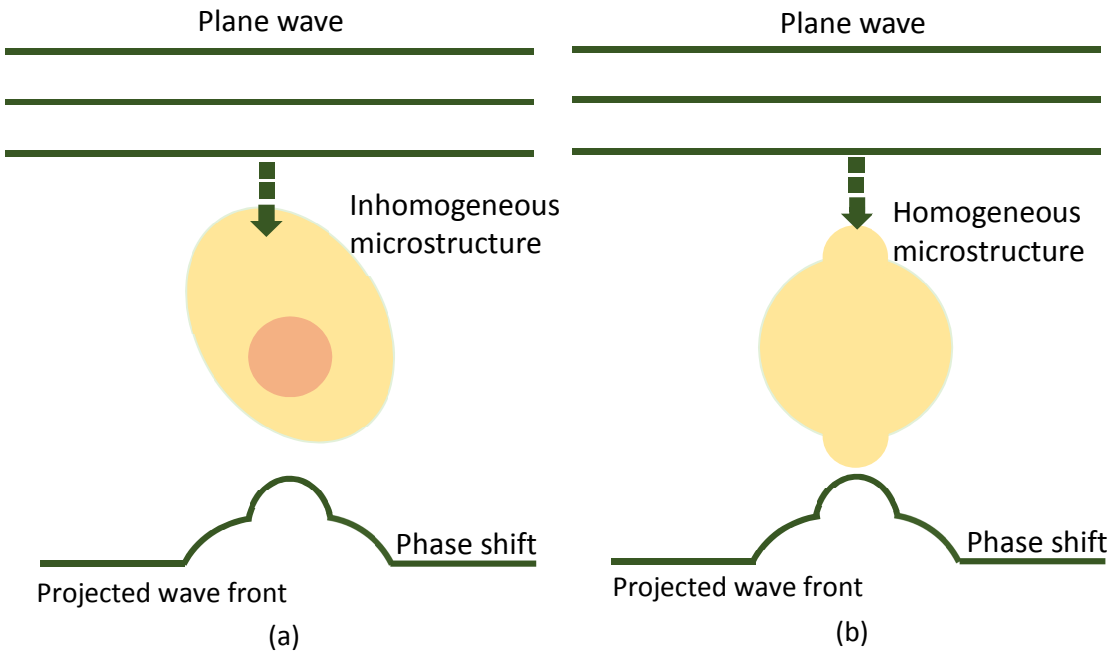

Figure 4.3 Illustrations of different structures having the same phase shift in the same medium: (a) one core-shell weakly scattering microstructure under an optical plane wave projection; (b) a homogeneous microstructure with irregular shape.

Figure 4.4 illustrates the schematic optics with a scanning mirror and a scan lens to perform the angular scan through the condenser with a large NA. The inset is an enlarged view of the plane wave illumination at different angles impinging on the cell and scattered wavefronts out of the cell.

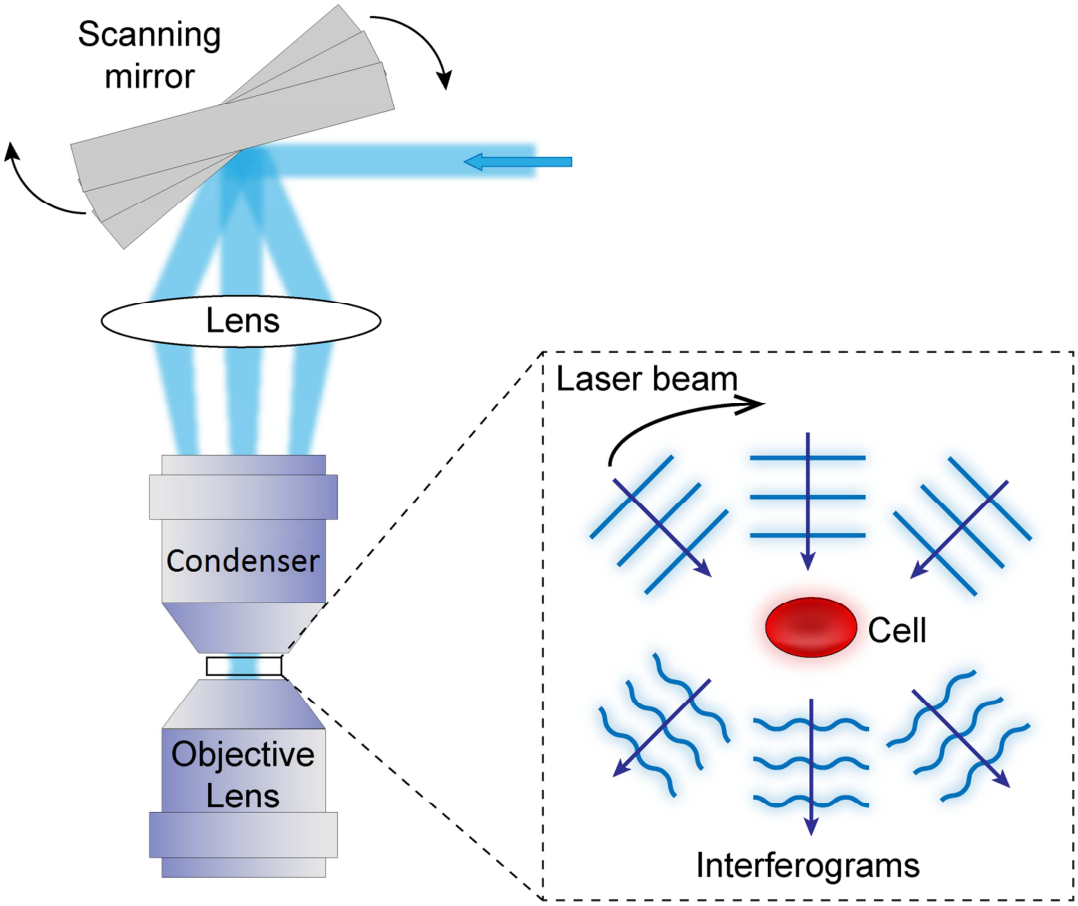

Figure 4.4 Schematic illustration of the optical system with a scanning mirror used to perform the angular scan through the condenser.

The 3D Refractive index map is reconstructed by using a diffraction algorithm which considers light diffraction inside a sample by solving the Helmholtz equation for the incident and scattered optical fields [112, 113]. Figure 4.2 depicts a simpler case of Fourier diffraction theorem with an in-plane plane wave.

Generally, 2D Fourier spectra of an optical field at a certain illumination angle is mapped onto the surface of a hemisphere called Edward sphere. The center position of the sphere is translated from the origin in the 3D Fourier space by the distance and direction corresponding to the $\vec{k}$ vector or spatial frequency of the incident angle. Therefore, 3D Fourier spectra can be composed by a series of 2D Fourier spectra, which are obtained from the multiple interferograms with various incident angles. Finally, the inverse Fourier transform of the mapped 3D Fourier spectra provides the reconstruction of the 3D refractive index distribution of the phase object. Detailed mathematical derivations of the diffraction algorithm can be found in References [7, 112, 113].

4.2 Intracellular Lipid Droplets

Lipid droplets are essential part of human and plants. As it contributes significantly to growth and numerous diseases, it is essential to develop new techniques to gain deep understanding on the biophysical properties of lipid droplets. An important biophysical feature is the refractive index of lipid droplets. The refractive index provides structural material and important information of cellular activities. Research has shown that cultured cancer cells have higher refractive index values compared to healthy non-cancer cells. Lipid droplets are closely linked to several tissues and heavily involved in many biological processes in the body. By

investigating their refractive indices can give researchers greater insight in these biological processes. The concentration of lipids also relates to tissue functional changes and the progression of disease. For instance, hepatic steatosis is indicated by the abnormal accu mulation of lipids in the liver. Knowing the refractive indices changes due to lipid droplets will also allow us to compare that of an obese individual to a normal healthy individual. This information can serve as a preliminary simple and direct way to test for early manifestations of obesity and other metabolic diseases.

4.2.1 What are Lipid Droplets?

Lipid droplet is mainly comprised of lipid esters and its surface is lined by a phospholipid monolayer as shown in Figure 4.5 [114]. The lipid droplet structure is distinctive as compared to other cell organelles. It is enclosed by a monolayer of phospholipids, which possesses both hydrophobic and hydrophilic elements, and proteins. In mammalian lipid droplets, phosphatidylcholine is the main surface phospholipid. At the centre core, hydrophobic neutral lipids are formed such as triglycerides, and sterol esters. The size of lipid droplet can vary greatly between different cell types and their number is also vastly different between cell types or population. Most lipid droplets have diameters between 0.5 µm to 10 µm while

some lipid droplets such as mature adipocytes have diameters of 100 µm that occupy almost the whole cytoplasm [115].

Many lipid droplets undergo accelerated growth and change their size during adipogenesis [116]. Lipid droplets are formed rapidly from endoplasmic reticulum by enzymes when there are high levels of fatty acids [117, 118]. This is true for both eukaryotes and yeasts. Even though the exact mechanism of formation is still unknown, lipid droplets are thought to form as they grow from when the endoplasmic reticulum and bud off from it as shown in Figure. 4.6. Triglycerides are accumulated from the two layers of the phospholipid membrane. Then, lipid droplets continue to grow either by direct diffusion of fatty acid or endocytosis of sterols [119].

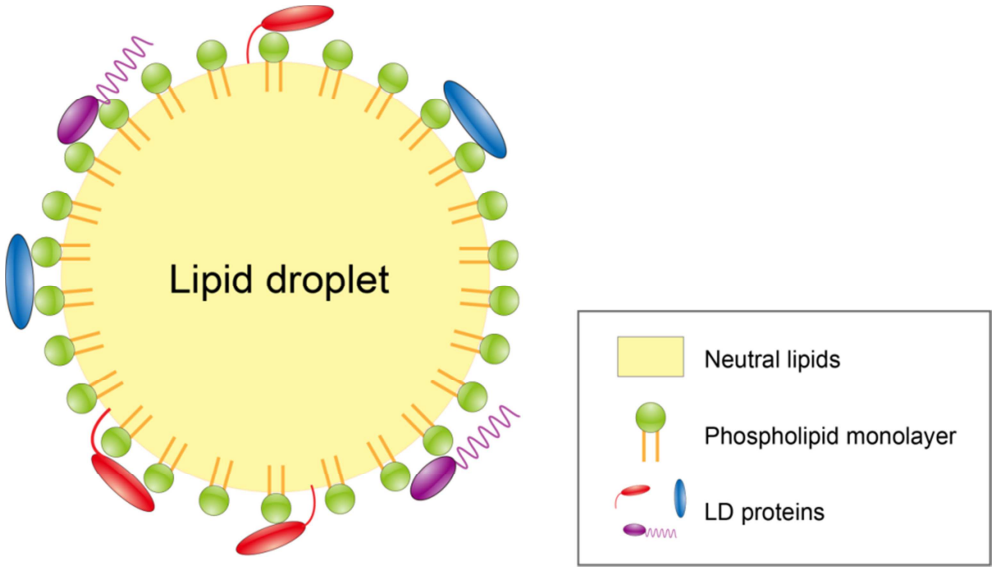

Figure 4.5 Schematic illustrations of lipid droplet and its structure [114].

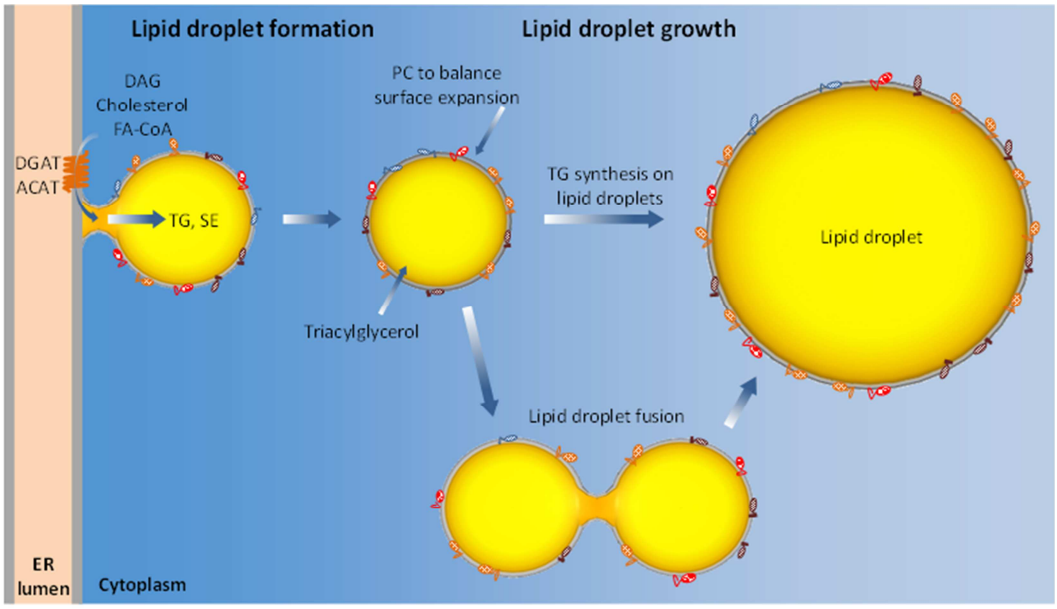

Figure 4.6 Schematic illustration of lipid droplet formation process [116].

The most specialized type of cells for storing lipids in lipid droplets is known as adipocytes. In human fat cells, large quantities of energy are stored in lipid droplets in the form triglycerides. Liver is the organ that has the largest volume to store lipids in the form of lipid droplets. Hepatocytes in the liver can hold up to enormous amounts of triglycerides [116]. Another organ that store lipid droplets is the small intestine. The intestinal enterocytes have large surface area to produce and store triglycerides. Skeletal muscle is involved in oxidative metabolism and have high amount of mitochondria and lipid droplets. Intramuscular triglycerides act as source of fuel for healthy muscle during periods of physical activity [120]. Other steroidogenic cells also have noticeable lipid droplets storage in the cytoplasm that is essential for producing steroid hormones [121].

4.2.2 Functions and Importance of Lipid Droplets

In the past few years, a strong interest in biology of lipid droplets is seen, investigating on how they function and coordinate with other parts of the cell. There is also strong interest to gain insight about other tissue or cell types, besides adipocytes. Neutral lipids stored in lipid droplets are used for phospholipids and cholesterol production, metabolism and steroid creation [122]. They are the fundamental parts of cell membranes and also sources that provide energy.

Lipid droplets perform an important role in storing cholesterol as cholesteryl esters and are vital in organelle development [123]. One of the important functions is to aid in sustaining cholesterol levels in intracellular membranes. Cholesterol in its free form is nearly insoluble in water, and hence needs to be transported by cholesterol-binding proteins [124]. This is a tightly controlled process that maintains the free cholesterol levels within a restricted range. It has been found that disruption of lipid droplets have damaging effects on cholesterol balance [125] such as interruption of the signaling pathways at plasma membrane that are dependent on cholesterol.

Lipid droplets also act as organizing cores for producing specific lipids such as triglycerides, which are made in the endoplasmic reticulum. Enzymes required for lipid synthesis move to lipid droplets and produce various types of lipids. Lipid droplets are associated with protein storage [126] and they also temporarily store unfolded membrane proteins before protein complex degradation. Through interactions with other organelles, lipid droplets are involved in lipid trafficking, and other cellular functions. In steroidogenic cells, their interactions possibly function in the production or catabolism of steroid hormones [127]. Lipid droplets also interact with endosomes by engulfing lipid droplets and sending them to lysosomes by autophagy in macrophages to create cholesterol [128]. Mitochondria associate closely with lipid droplets in numerous cell types such as adipocytes, lactating cells and oocytes, their synapses allow direct transport of fatty acids released from lipolysis of triglycerides to sites of oxidation to meet the cell's energy needs [116].

It is crucial to achieve a balance in maintaining the availability of lipid droplets stored in cells and the requirements of metabolic energy activity because excessive lipid storage capacity will lead to diseases. Obesity happens when there are excess lipid storage and excess lipid droplets in the adipose tissue [129]. Cells store excess lipids such as fatty acids and sterols in esterified forms. The unesterified lipids can cause inflammation in tissues and lead to lipotoxicity. Obesity can lead to metabolic malfunctions, which escalate the risk for type II diabetes,

steatohepatitis and coronary heart disease [130]. When the adipose tissue accumulates excess lipids, it is enlarged and this affects insulin secretion directly. These excess free fatty acids flow from the adipose tissue to the skeletal muscle, liver or heart. They also interfere with signaling pathways while causing insulin resistance in the surrounding tissues [131, 132]. Obesity can also result in excess lipid droplets to be accumulated in hepatocytes of the liver, known as hepatic steatosis [133, 134]. This may also lead to steatohepatitis that is nonalcoholic inflammation of the liver along with simultaneous fat increase and even cause liver failure. Other diseases that can lead to excessive lipid droplets include atherosclerosis, cachexia [135], etc. On the other hand, deficiencies in lipid droplets can lead to damaging effects on health. The body′s largest fat storage adipose tissue regulates lipid metabolism [136-138]. It buffers excess lipid by isolating fatty acids into triglycerides, hence protecting the body from lipotoxicity or tissue dysfunction. It also releases fatty acids and glycerol into surrounding tissues during starvation. Therefore, it is significant in research on investigating the lipid droplet mechanisms and how they contribute to diseases, allowing a better understanding and potential ways to treat such diseases.

4.2.3 Microscopic Imaging of Cellular Lipid Droplets

Most lipid droplets have diameters between 0.5 µm to 10 µm, which can be imaged by light microscopy. Their refracting nature of lipid droplets makes them distinguishable under phase contrast imaging. But both methods cannot provide quantitative information with sufficient details to study the changes of lipid droplet due to micro-environmental stimulations. The intracellular 3D morphology of lipid droplets can be measured after specific dye staining by laser scanning confocal microscopy with submicron resolution. However, 3D fluorescence images from confocal do not provide material information, such as dry mass and mass density. Therefore, a novel approach is proposed to determine the refractive index of lipid droplet using ODT technique for quantitative study of cellular lipid droplets under fatty acid stimulation.

Lipid droplets are typically stained using hydrophobic dyes such as Oil red O, which is usually used for fixed samples, Nile red and BODIPY. To study lipid droplets in a single cell, BODIPY dye is used to stain the lipid droplets and imaged under the fluorescence imaging. Subsequently, the 3D refractive index map of the whole cell is achieved using the ODT system. Both the cell and lipid droplet distribution can be explored.

4.3 Experimental setup and Preparation

4.3.1 Optical System

The ODT system used is an existing customized system following the system of Su *et al*. [7] with some modifications and one more function of fluorescent imaging as shown in Figure 4.7. The optical setup is based on the Mach-Zehnder interferometer combined with the phase shifting technique to reduce the noise and improve precision. This is a typical off-axis phase shifting quantitative phase imaging (QPI) configuration. To realize the diffraction tomography, multiple interferograms are obtained by using a pair of x-y scanning mirrors.

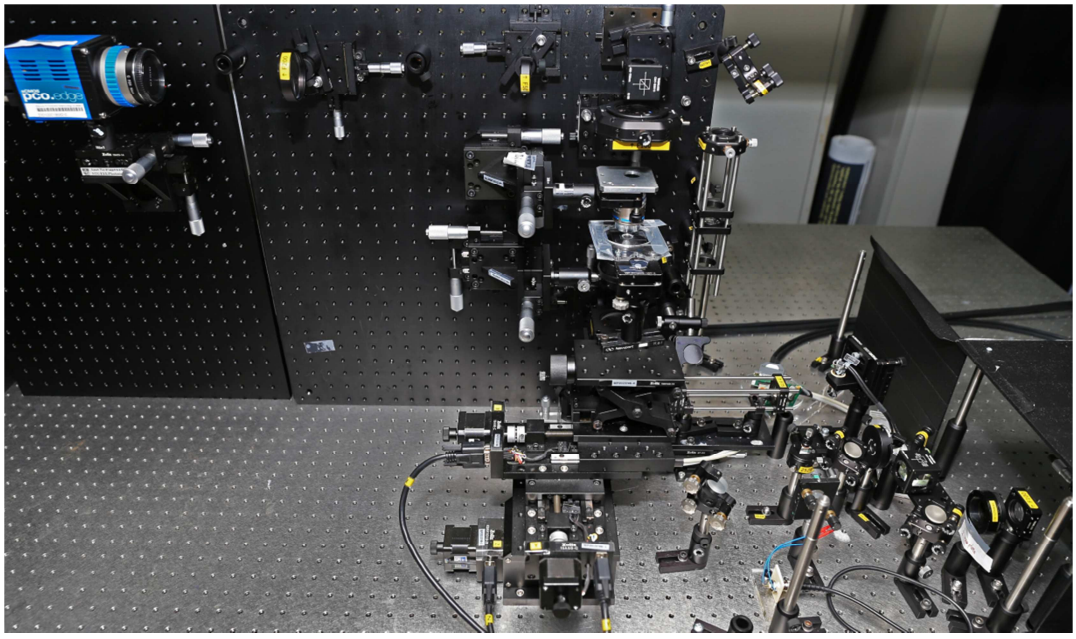

Figure 4.7 Photograph of the optical setup of the ODT system

The optical layout of the system is illustrated in Figure 4.8. The laser beam from a 488 nm DPSS laser (COHERENT, Sapphire 488 SF, 100 mW, 100:1 polarizability) passes through a polarizer, POL, to increase polarizability. A quarter wave plate, QWP, is used to change the linearly polarized laser beam to a circular polarized beam such that the reflected S- and P-polarized beams are both retarded by 90° corresponding to their original orientations and thus blocked. Then, the circular polarized laser beam passes through a 10× objective lens OL1 and then a 25 μm pin-hole spatial filter to eliminate high frequency noises and thus clean up the Gaussian beam profile. After a collimation lens L1 (f_1 = 50 mm), the laser beam is expanded to the diameter of about 3 mm. Next, the S- and P-polarized waves are separated by a polarized beam splitter (PBS). The objective beam shown in blue color is impinging on a galvanometer mirror SM-X (Scanlab, DynAXIS 3M) located at the front focal plane of the 4-f lens system and then impinging on the other galvanometer mirror GM-Y (Scanlab, DynAXIS 3M). The two scanning mirrors is located far part at the focal plane of the 4-f lens system (L2 and L3, $f_2 = f_3$ =75) is to ensure that the light spot stays at the same central point at the two galvanometer mirrors SM-X and SM-Y, ensuring that the object beam does not incur transverse displacement during scanning and penetrating through the sample cell. It avoids sample spot dislocation at the image plane. After X-Y scanning, the collimated beam is focused by the scan lens L4 (f_4 = 100 mm) to the back focal plane of an oil-immersion condenser (Nikon, NA = 1.40) to generate a plane wave

illumination on the sample cell. The uniform plane wave is essential to achieve pure scanning without changing the direction and position of the scattered wavefront. A 60× oil immersion objective lens (Nikon, NA = 1.40) is used to collect the transmitted illumination light, which is still depicted in blue lines, and the weakly scattered light depicted in dashed green lines. Normally, it is the latter to form a microscopic image with a bright-field microscope. The object beam is then re-collimated by a tube lens L5 (f_5 = 100 mm).

The reference beam from the polarization beam splitter PBS, depicted in red color, impinges on a mirror, M, to change its direction. Then it then passes through a half wave plate, HWP, to change the polarization of the beam by 90° such that the reference and objective beams are in the same polarization orientation, which is the essential condition for two beam interference. Next, it is reflected twice from each of the reflective prisms PS1 and PS2. PS1 is attached to a piezoelectric transducer (PZT) to generate a phase shift of π/3 along the lateral direction of the beam at each scanning angle. By adding the prisms PS1 and PS2 in the optical path transverse displacement of the beam spot can be avoided. The beam then passes a 4-f lens system with lenses L6 and L7 (f_6 = 50 mm, f_7 = 75 mm) whose function is to expend the diameter of the beam. After being reflected by 90° with a mirror, the reference beam recombined with the object beam by a non-polarizing beam splitter referred as BS.

The objective and reference beams passes through another 4-f lens system with lenses L8 and L9 (f_8 = 50 mm, f_9 = 200 mm), whose function is to increase the magnification by a factor of 4 for the interference images. Eventually, the two beams reach the sensor plane of a SCMOS camera (PCO Edge 5.5) to form an interferogram. The camera has the function of global shutter, which ensures that intensity signals at different pixels and lines are captured at the same time. The maximum speed of the camera is 100 frames/sec, while limited by electronic signal transferring speed, the recording speed for all experiments is about 80 frames/sec. The pixel size of the camera is 5.5 μm × 5.5 μm. 1024 pixel × 1024 pixel image format is used throughout the experiments. The overall lateral magnification of the system is about 102×, attributed by the 4-f system composed by the 60× objective lens and the lens L5, while the last 4-f system composed by lenses L8 and L9.

The two scanning mirrors are controlled by an electronic control box. The rotation of the mirror and recording of the interferograms by the camera are synchronized with a custom-made software via an analog command signal and a trigger signal, respectively. The interferograms are acquired at a frame rate of 100 fps and an exposure time of 0.1 ms per image.

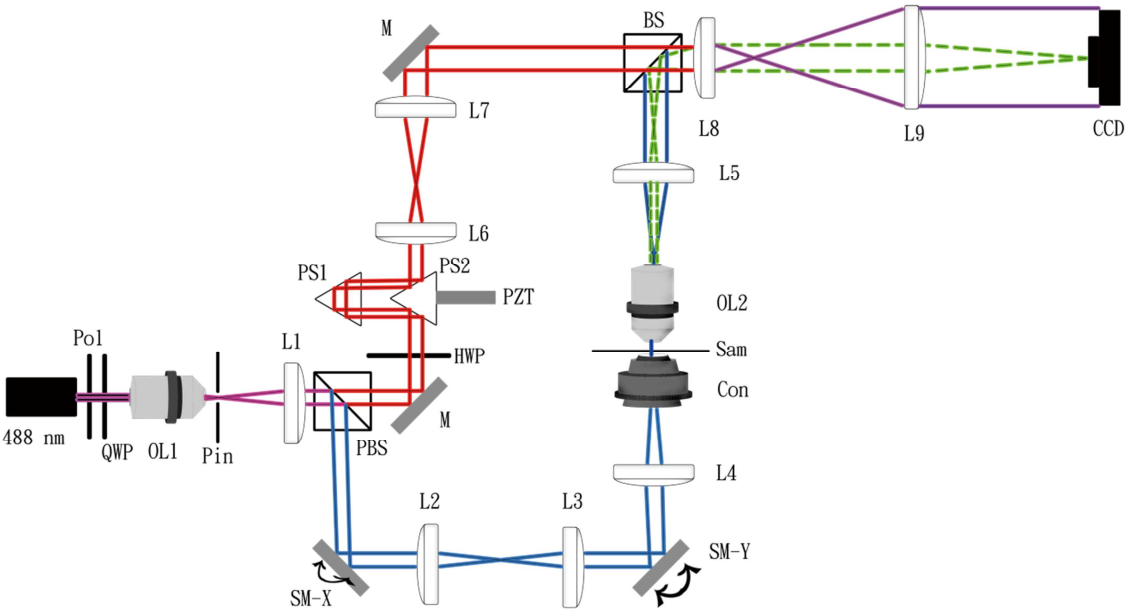

Figure 4.8 Optical layout of the ODT system. Pol: polarizer; QWP and HWP: quarter and half wave plate; OL1 and OL2: objective lenses; Pin: pin-hole spatial filter; L1 to L9: lenses with various focal lengths; PBS: polarization beam splitter; BS, beam splitter; SM-X and SM-Y: galvanometer mirrors; Con: Oil immersion condenser; Sam: sample; M: mirror; PS1 and PS2: prisms; PZT: piezoelectric transducer for position shifting of the mirror.

The customized ODT system is integrated with one value-added function of fluorescence imaging as shown in Figure 4.9. A long pass filter, LPF (Thorlabs with the threshold = 500 nm) can be slid in the object beam path between the objective lens OL2 and the lens L5 to capture fluorescence images. With the 488 nm laser source, a wide range of fluoresce dyes can be employed to stain different intracellular organelles such as SyBr Green for DNA staining, mitotracer green for

mitochondria, BODIPY for lipid droplets etc. The integrated function enables capturing of a projected fluorescence image of the same single cell using the same optical system to compare with the 2D refractive index map and identify different intracellular organelles with corresponding dye staining.

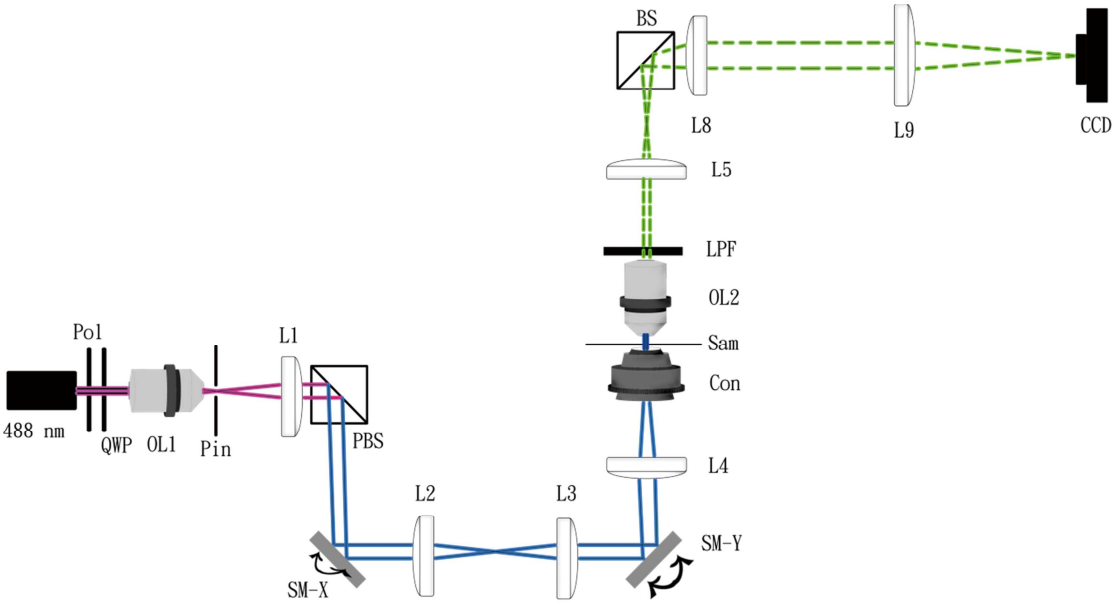

Figure 4.9 Optical layout of the object-beam arm for fluorescent imaging.

4.3.2 Methodology for Obtaining 3D Refractive Index Maps

To reconstruct the 3D refractive index map of a single cell using the ODT system, the key function is to perform angular scan of the cell at illumination angles ranging between -60^{o} and +60^{o}. At each angle, the PZT mounted with the prism

PS1 generates phase differences in the reference beam corresponding to the objective beam from 0 to 2π with a nominate interval of π/3. With a phase shifting cycle of 6 interferograms, a 2D phase map/image is obtained by the advanced iterative algorithm. The stability of phase measurements is achieved by the iterative phase extraction algorithm without the need to control precisely the value of phase shifts that requires extra feedback controlling system. A good quality 3D refractive index map requires about 500 2D phase maps/images. Therefore, a total of 3000 frames of interferograms are captured. Ultimately, the whole sets of 2D phase maps with varying illumination angles can be employed to reconstruct the 3D refractive index map of the cell. With current computer format, the processing time required about 30~40 minutes.

Figure 4.10 is the schematic illustration of the process flow of obtaining a 3D refractive index map. One rotational scan angle will trigger the PZT to displace 6 times with a phase difference of π/3. While each phase shift signal will trigger the camera to capture the 1024 pixel × 1024 pixel image. The synchronization of these three key components are realized and controlled by the existing customized graphic user interface. Once 6 phase shifted images are recorded by the camera, the control interface will send an order for the X-Y scanning mirror to rotate one angle increment. When 3000 images are all recorded, the control interface will stop the whole imaging cycle. The interferograms are computed to obtain the 500 frames of 2D phase maps and subsequently reconstruct the 3D refractive index map. The

processing time needed to reconstruct the 3D refractive index map is approximately 1 hour using a 10-core 2.3-GHz workstation with a 4 GB graphic card. All images are reduced from 1024 × 1024 pixels to 512 × 512 pixels due to the limited computing power. The detailed computing algorithms are out of the scope of the project, thus not included in this chapter.

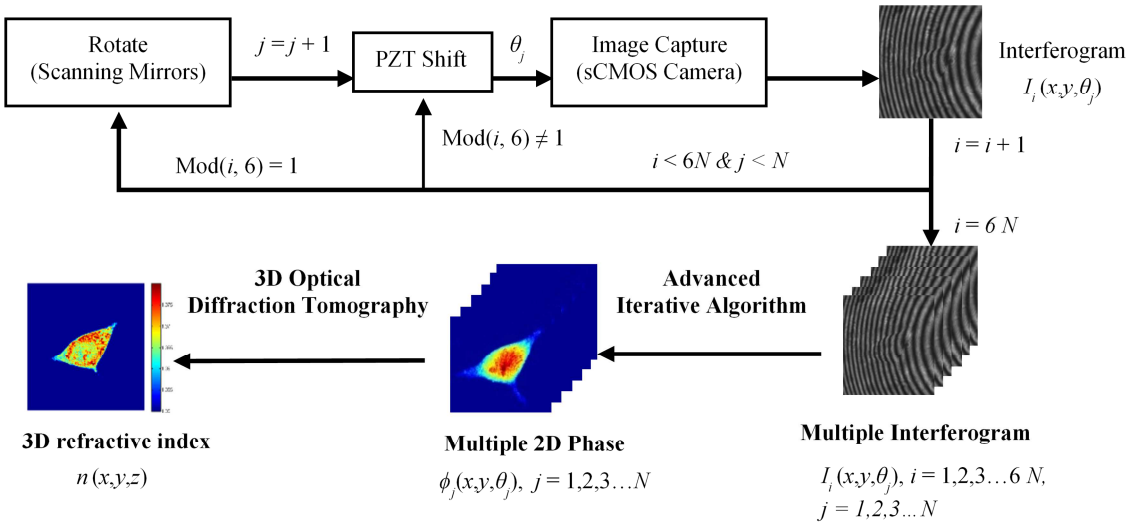

Figure 4.10 Schematic illustration of the process flow to reconstruct a 3D refractive index map, where, j and i are the indices of scanning angles and interferogram frames and θ_j is the jth scanning angle of the object beam.

4.3.3 Cell culture and fluorescence staining

In the experiments, 3T3-L1 cell line (CL-173, ATCC) is used. To thaw the vial of frozen cell, which is removed from the liquid nitrogen freezer, it is left in a 37°C

water bath (YIHDER, BT-150D) with moderate agitation. The cells are thawed until all ice crystals are melted. The vial is removed from the water bath and decontaminated with 70% ethanol solution. Then, the content is transferred to the culture medium, Dulbecco's Modified Eagle's Medium (30-2002, ATCC). Culture medium should be put in 37 degree, 5% CO2 incubator at least 15 minutes to adjust the pH to normal range (7.0 – 7.6) before adding 3T3-L1 cells. Culture medium will be renewed 2 times per week, and subculture will be implemented when reaching about 70-80% confluence. When the cells are fully cultured, 10% of the culture is used in the experiments while the remaining is frozen for future usage by cryopreservation. For storage, the cell is frozen, and 5% DMSO is added to culture medium. Cells are stored in -80°C for 24 hours for a gradual temperature reduction before being moved for storage in liquid nitrogen. Before the experiments, the cells will be taken from flask or dish, and seeded on cover glass. The cells are cultured in 37^{o}C and 5% CO_2 in the incubator at least 12 hours for cell adhesion. Various fluorescence dyes (Thermo Fisher) are used to stain various intercellular organelles, including BODIPY for lipid droplets, mitotracer green for mitochondria and SyBr Green for nucleus DNA.

4.4 Experimental Results and Discussions

4.4.1 System Calibration and Characterization

The ODT system as an interference imaging system is firstly calibrated for its imaging magnification and resolution. With a standard resolving power test target (USAF 1951), the system's magnification is confirmed to be 102×. The edge definition and refractive index precision is calibrated with 5-μm polystyrene beads (Polyscience, Inc., n = 1.6054 at 488 nm), while the accuracy and precision of the system are also evaluated with different sonicated oil droplets with known refractive indices.

Calibration with microbeads in media with known refractive indices

Figure 4.11a, to 4.11c display the 2D cross sectional refractive index maps obtained from the 3D refractive index maps of a 5-μm bead immersed in immersion oils with refractive indices of 1.551 1.556 and 1.560, respectively. Figure 4.11d is the refractive index profile along the white dotted line in Figure 4.11b. The measured value of full width at half maximum is 5.08 μm, which

indicates the diameter of the bead. It also depicts the edge response, which is the distance required for the intensity to rise from 10% to 90%. It is a measure to reflect the resolution of the imaging system. The measured resolution is about 300 nm.

The mean refractive indices of beads in three media are measured to be 1.6039, 1.6041 and 1.6045, respectively, as compared to the standard value of 1.6054. The average refractive index difference, Δn, between the polystyrene bead and the surrounding liquid medium is obtained by ODT and the results are shown in Figure 4.12. It can be seen that the measured refractive index differences match with the standard values. When the Δn is close to or larger than 2π (the last data point in Figure 4.12), the precision of the ODT system is reduced due to the uncertainty of the phase difference.

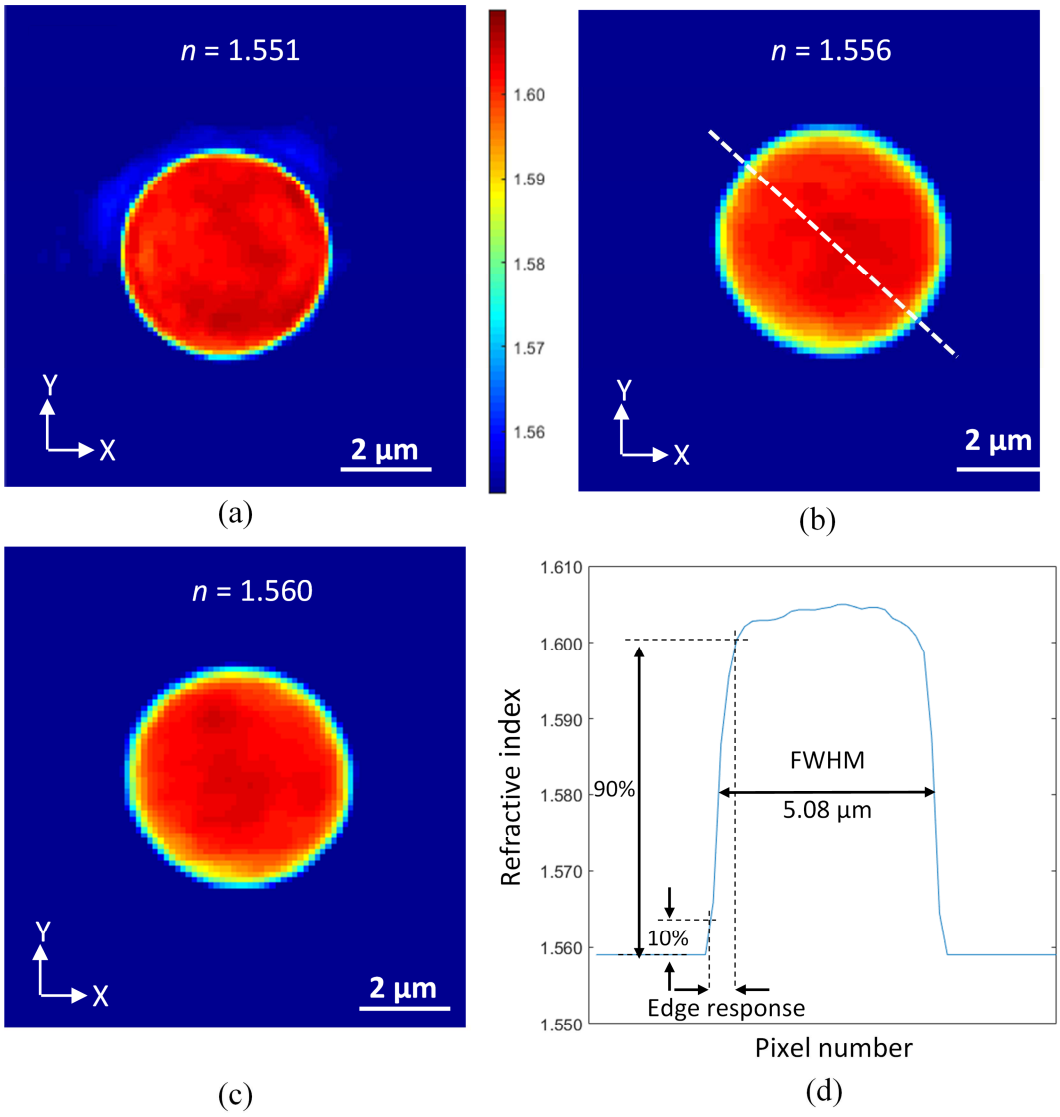

Figure 4.11 Cross section 2D refractive index maps at the central horizontal plane (X-Y) of a 5 µm polystyrene bead (n = 1.605) in the medium of immersion oil with n_{med} equals to (a) 1.551; (b) 1.556 and (c) 1.560 respectively; while (d) is the refractive index profile along the white dashed line on the 2D map shown in (c).

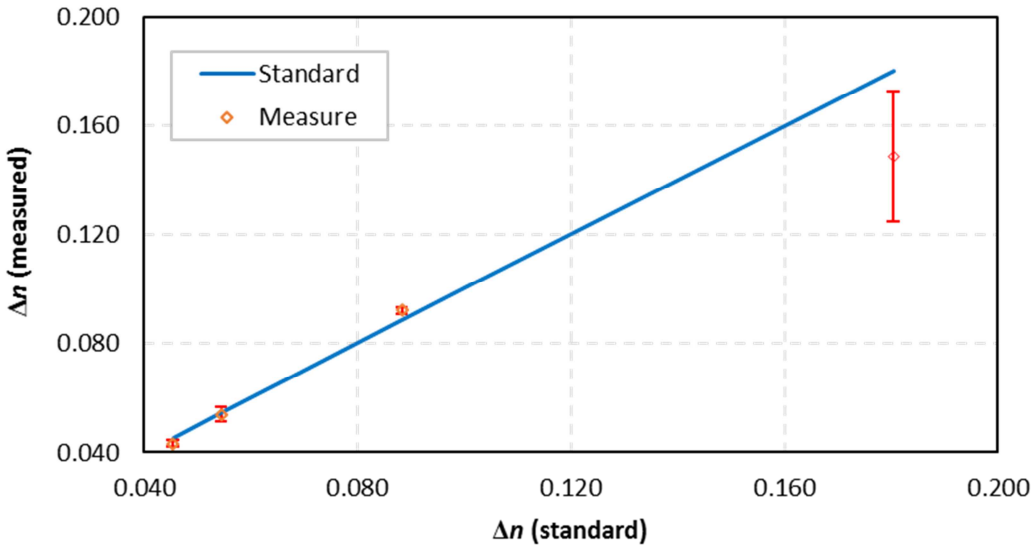

Figure 4.12 Calibration results of the system using single 5 µm polystyrene beads immersed in immersion oils with different refractive indices.

Calibration with droplets of different oils in PBS medium

Since the ODT system will be used to measure the refractive index of cellular lipid droplets, the system is further calibrated by measuring the refractive index precision of various oil droplets. Their refractive indices are firstly measured by a high precision Abbé refractometer (Abbemat MW, Anton Paar) at the wavelength of 480 nm and temperature of 20°C. Subsequently, micro-sized oil droplets are generated by using an ultrasonicator and their refractive index and size are measured by the ODT system. The measured refractive index data, $\bar{n}$, and their standard deviation errors are also included in Table 4.1. The calculation of

$\frac{|\bar{n}-n_{stard}|}{n_{stand}} \times 100\%$ in the 2nd last row of Table 4.1 is to evaluate the accuracy of the system and all data are less than 0.3% show that the accuracy is fairly good. The calculation in the last row is to use the standard deviation as an indicator for system's precision. Since error can only be one digit, they are firstly round up to one digit and then used in the equation of $\frac{\Delta n}{n_{stand}} \times 100\%$ to evaluate the precision. From the data in the last row, we can see that all the values are less than 0.6% which suggests that the precision of the system is also considerably good. To match with one digit of standard deviation, it might be prudent to define the sensitivity of the system at 10^{-3} based the calibration of oil droplets. In following experimental analysis, all standard deviations are only expressed in one single digit. Further consideration for other errors include electronic noises, imprecision of PZT and scanning mirror movements and reconstruction algorithm, as well as the reading errors of the CCD pixels - when an object is small and intensity signal is weak, error of each CCD pixel also contribute to overall the error. Therefore the refractive index measurement resolution is limited to 0.005 RIU for lipid droplet analysis in next section.

The measured refractive index data tabulated in Table 4.1 are drawn in Figure 4.13 with error bars representing the standard deviation which shows that the measured refractive indices are agreed quite well with those refractive index values measured with a high accuracy auto-refractometer.

Table 4.1 Calibration using oil droplets with known refractive indices

Oil of droplets	Hair oil	Immersion oil	Immersion oil	Peanut oil	Olive oil	Grape seed oil
Refractometer n_{stand}	1.4054	1.4200	1.4520	1.4785	1.4806	1.4861
ODT $\bar{n}$	1.4090	1.4241	1.4545	1.4782	1.4781	1.4839
Standard deviation Δn	±0.0055	±0.0049	±0.0033	±0.0065	±0.0078	±0.0031
Accuracy $\frac{\lvert\bar{n}-n_{stand}\rvert}{n_{stand}} \times 100\%$	±0.27	±0.29	±0.17	±0.02	±0.17	±0.15
Precision $\frac{\Delta n}{n_{stand}} \times 100\%$	±0.43	±0.35	±0.28	±0.47	±0.54	±0.02

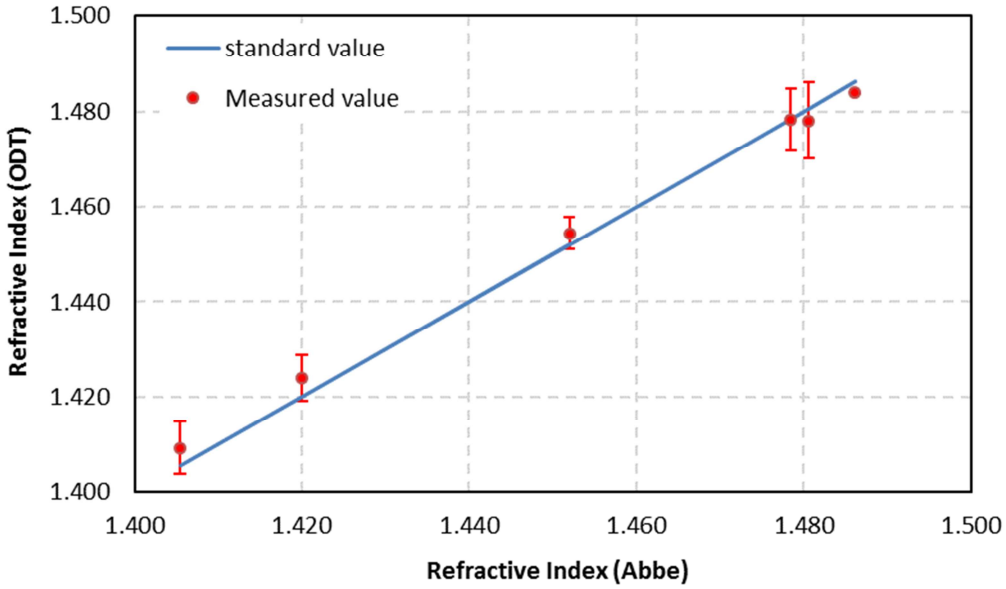

Figure 4.13 System calibration results: standard refractive indices of oils measured by a high precision auto-refractometer versus measurement values by ODT system.

For brevity, only one set of results for one droplet of the immersion oil with n = 1.420 is displayed in Figure 4.14. Figure 4.14a is an interferogram of the oil droplet, and Figure 4.14b is the 2D phase map obtained from 6 phase shifted interferograms. Figures 4.14c is a 2D cross-sectional slice of the 3D refractive index map of the droplet at the focal plane, and Figure 4.14d is the refractive index profile along the diameter of the 2D refractive index map in Figure 4.14c. The FWHM is 4.50 μm.

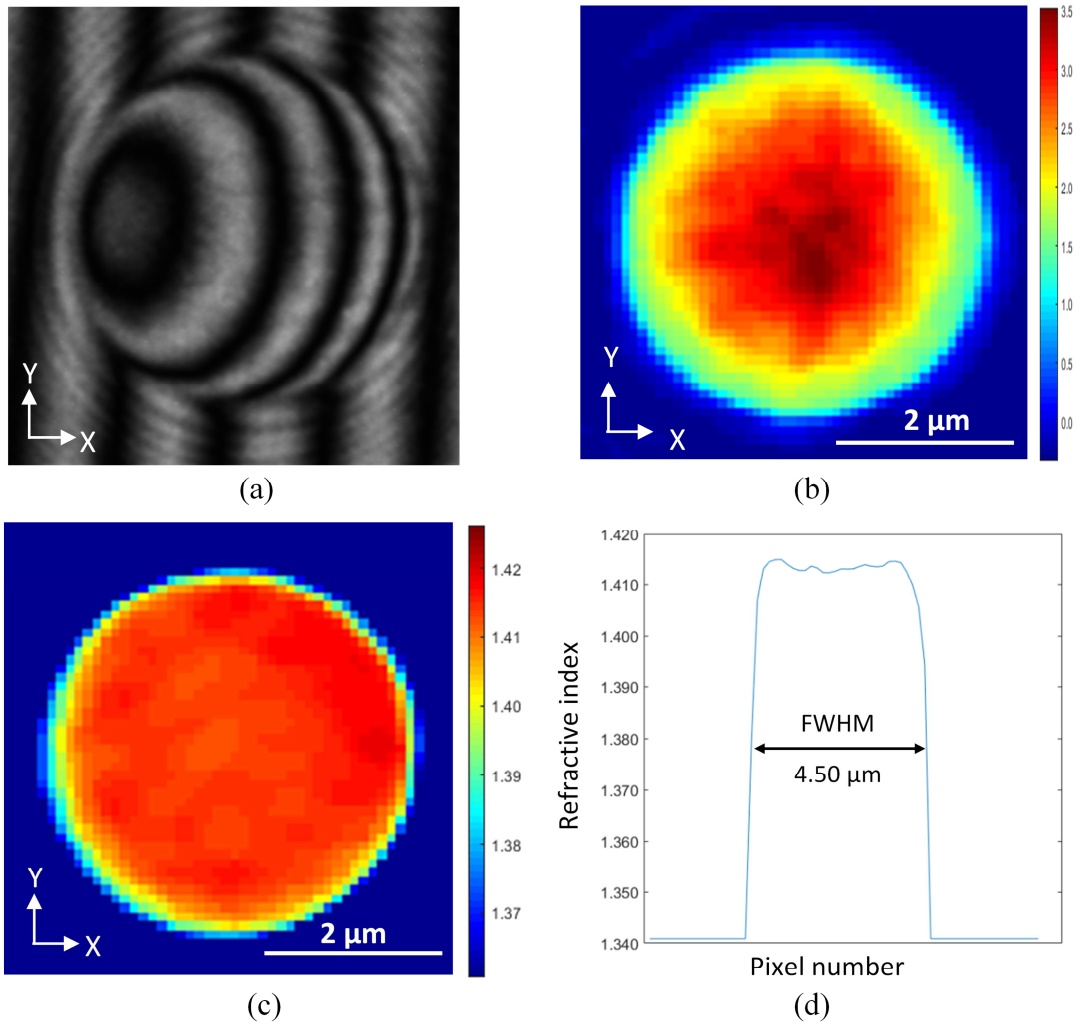

Figure 4.14 One set of measurement results for one immersion oil droplet (n = 1.420): (a) an interferogram; (b) 2D phase map; (c) cross-sectional 2D refractive index map selected from the 3D refractive index map; and (d) refractive index profile along the diameter of the oil droplet in (b).

Figure 4.15 presents the refractive index measurements of different oil droplets versus droplet sizes. It is to check if the refractive index measurement is size

dependent especially in situations near system's spatial resolving limit. The results show that the refractive index is consistent and not depending on the droplet size. This is theoretically true because the refractive index is depending on the mass density of the droplet but not the size.

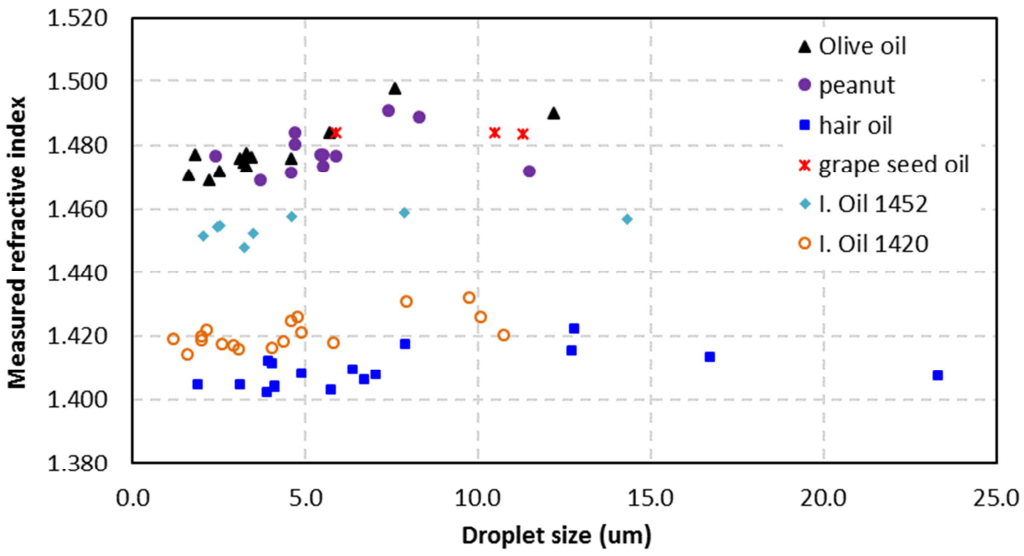

Figure 4.15 Experimental results of the refractive index values of oil droplets versus sizes of various oil droplets.

4.4.2 Refractive Index Mapping of Single Cells

The ODT system with the integrated fluorescence imaging is firstly used to measure the refractive index maps of intracellular organelles, including nucleus, nucleoli and mitochondria of Madin-Darby canine kidney (MDCK) cells.

Figure 4.16 presents a live MDCK cell showing its nucleus and nucleoli. Figure 4.16a is a projected fluorescent image of the nucleus of the MDCK cell stained with SYBR green nucleic acid gel stain. Figure 4.16b is the cross-sectional 2D refractive index map from the 3D refractive map of the cell in the focal plane (x-y). From this map, the average refractive index of the nucleus and nucleoli are 1.358 ± 0.007 and 1.373 ± 0.008, respectively. Figure 4.16c is the y-z cross-sectional refractive index map of the vertical line shown in Figure 4.16b. Figure 4.16d is the superposition of the fluorescence image in Figure 4.16a and the unicolor version of the 2D refractive map shown in Figure 4.16b. Figure 4.16e is the x-z cross-sectional refractive index map of the horizontal line shown in Figure 4.16b. Lastly, Figure 4.16e is the zoom-in view of the nucleoli of the highlighted square in Figure 4.16b. By using both fluorescence image and refractive index map, the nucleoli of MDCK cell is successfully identified and its refractive index is measured.

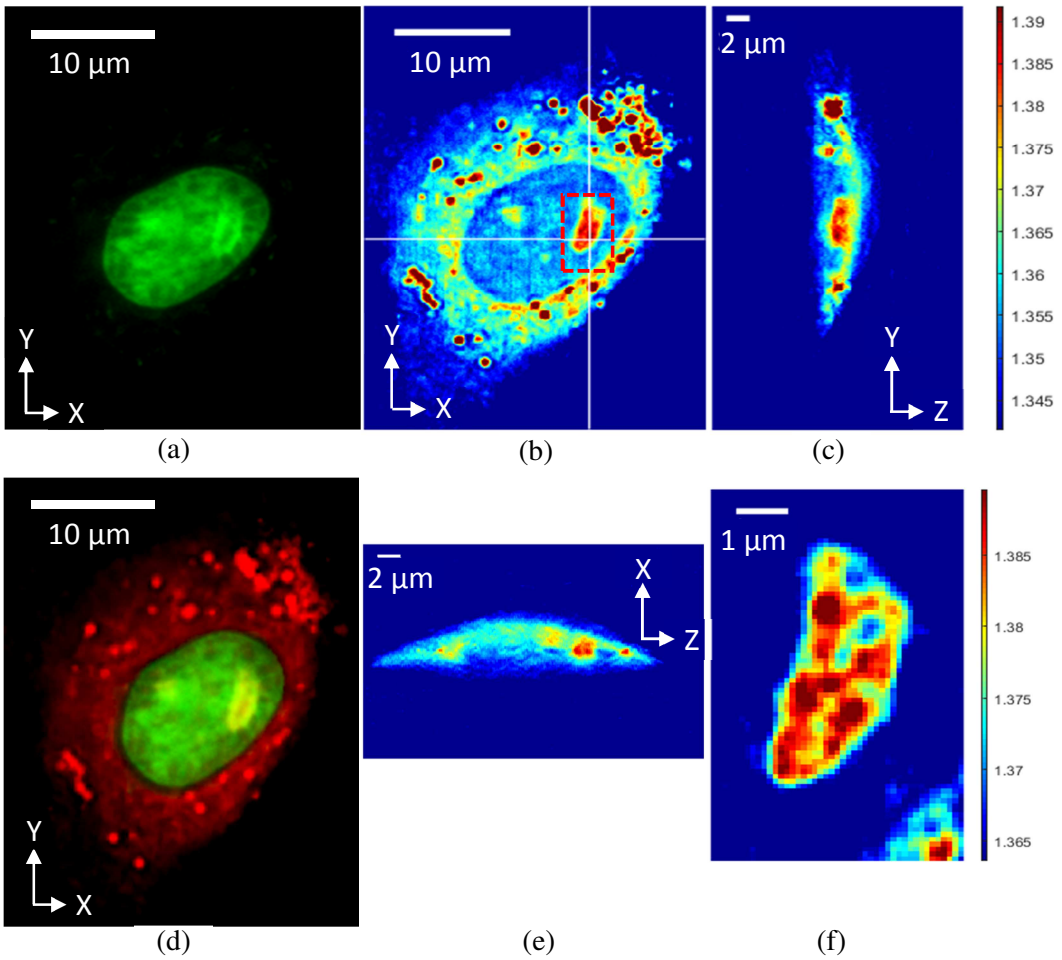

Figure 4.16 Measurement results of a MDCK cell: (a) 2D projected fluorescent image of the nucleus of an MDCK cell stained with SYBR green; (b) 2D refractive index map of the cell in the focal plane (x-y); (c) Y-Z cross-sectional refractive index map of the vertical line shown in (b); (d) superposition of (a) and the unicolor version of (b); (e) X-Z cross-sectional refractive index map of the horizontal line shown in (b); and (f) the zoomed-in view of the 2D refractive index map of nucleoli highlighted in (b).

The same approach can be used to identify and measure the refractive index of different intracellular organelles, for instance, Mitotracer Green is used for mitochondria staining. Figures 4.17a shows the cross-sectional 2D refractive index map from the 3D map of the MDCK cell (in the focal plane) with refractive indices in the range of 1.354 to 1.368. Figure 4.17b is a unicolor version of the 2D map in Figure 4.17a. Figure 4.17c is the projected fluorescence image of the whole MDCK cell to show the mitochondria distribution in the MDCK cell. Finally, Figure 4.17d is the superposition of Figure 4.17b and c. The areas in yellow indicate strong fluorescence.

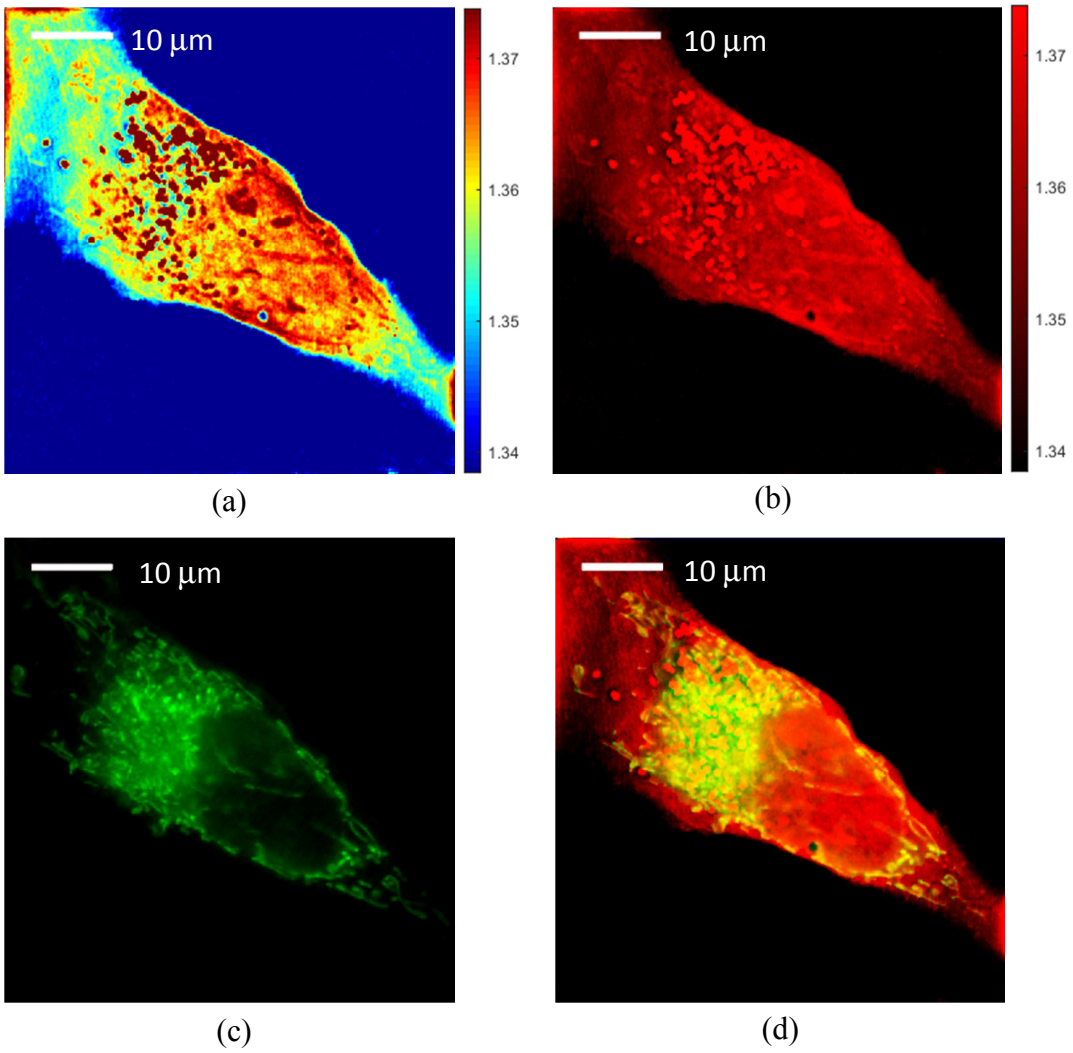

Figure 4.17 Experimental results of (a) 2D refractive index map (x-y) of a slice of MDCK cell in the focus plane; (b) a unicolor version of the 2D map in Figure 4.17a; (c) projected fluorescence image of the whole MDCK cell stained with Mitotracer green dye to show the mitochondria distribution in the MDCK cell; and (d) is the superposition of (b) and (c). The areas in yellow indicate strong fluorescence.

4.4.3 Refractive Index Measurement of Lipid Droplets

After calibration and demonstration of the ODT system to measure various intracellular organelles, the ODT system with the integrated fluorescence imaging is used to measure live single 3T3-L1 cell, focusing on lipid droplets, under different micro-environmental stimulations. 3T3-L1 cells are stained using BODIPY dye specifically to label lipid droplets. In the experiments, 3T3-L1 cells are cultured under different concentrations of oleic acid, a fatty acid, and the refractive index of the lipid droplets generated by the 3T3-L1 cells are measured. The images and consequently 3D refractive index maps of 3T3-L1 cells are obtained with the addition of 0, 0.5, 1.0 and 2.0 mM of oleic acid, respectively, in their culture media. After 20-hour culture, the live cells are measured by the ODT system. In each test, 10 live cells are captured. From the reconstructed 3D refractive index map, total droplet number ranges from 400 to 700 for each test is measured.

Lipid Droplet analysis with zoom-in view and refractive index profile

Figure 4.18 shows a set of experimental results of a fully cultured live 3T3-L1 cell without any addition of oleic acid as the control experiment. Figure 4.18a is the 2D refractive index map of the cell near the focal plane, and the square area highlighted by the dashed line is enlarged in Figure 4.18b. Figure 4.18c is a projected fluorescent image of the 3T3-L1 cell with green fluoresced lipid droplets. Therefore, lipid droplets are confirmed by the fluorescence image and their refractive index are measured from the refractive index map. A refractive index profile along the diameter of the lipid droplet, as indicated by the white dashed line in Figure 4.18b, is displayed in Figure 4.18d. For this particular droplet, the FWHM is measured as 0.98 μm. By analyzing a series of lipid droplets, it is found that the size of lipid droplets are in the range of 0.5 μm to 2.0 μm.

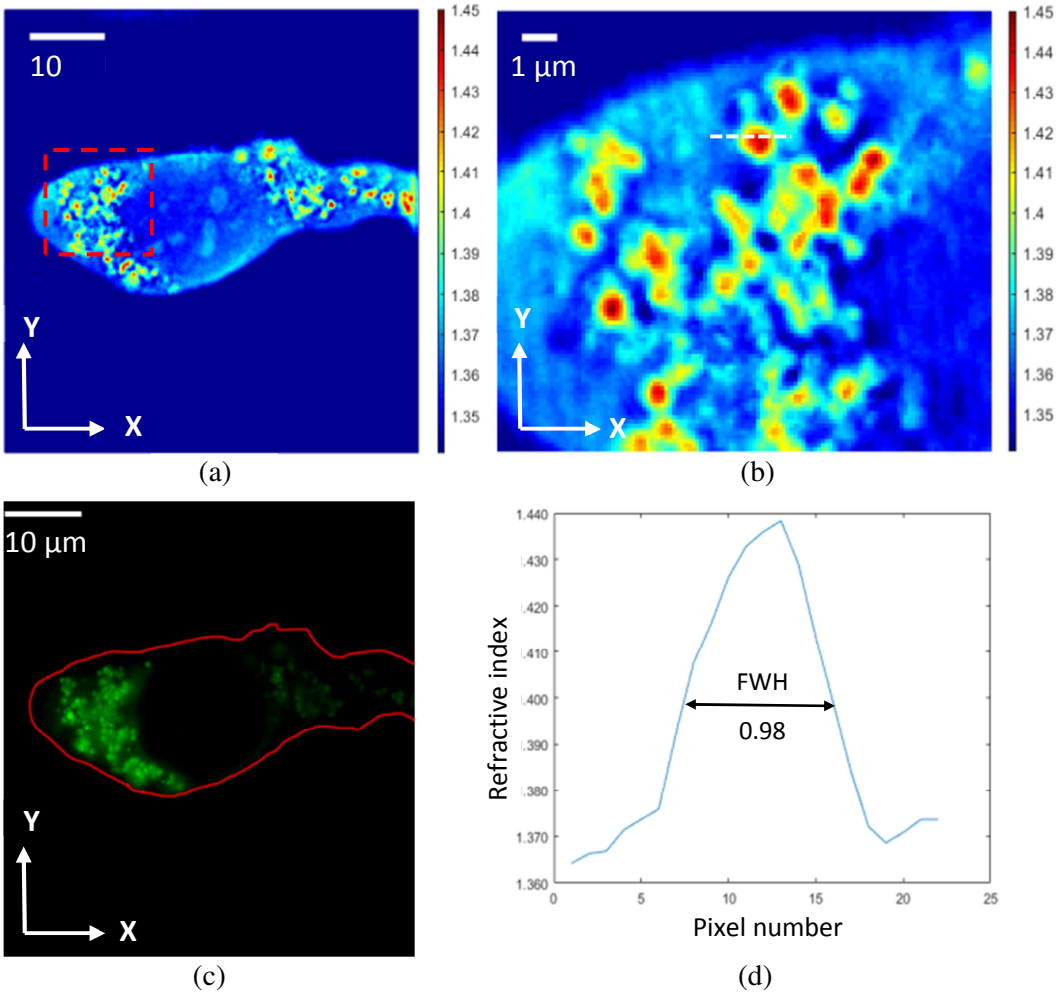

Figure 4.18 Experimental results of a live 3T3-L1 cell (a) 2D refractive index map (X-Y) of a slice of the cell close to the focus plane; (b) zoom-in view of the highlighted area in (a); (c) the projection fluorescence image of the whole cell with BODIPY dye for lipid droplet staining; and (d) refractive index profile along the dashed line in (b).

Figure 4.19 shows a set of experimental results of a cultured 3T3-L1 cell imaged 20 hours after 0.5 mM oleic acid is added to the culture medium. Figure 4.19a is a cross-sectional 2D refractive index map of the cell near the focal plane, and the square area highlighted by the dashed line is enlarged in Figure 4.19b. Figure 4.19c is the projected fluorescent image of the whole cell with green fluoresced lipid droplets. A refractive index profile along the diameter of a lipid droplet, as indicated by the white dashed line, is displayed in Figure 4.19d. For this particular droplet, the FWHM value is determined to be 0.96 μm. Figure 4.19e and 4.19f are the cross-sectional 2D refractive index map in the X-Z plane and Y-Z plane, respectively, along the horizontal and vertical lines in Figure 4.19b. Similarly, Figure 4.20 and Figure 4.21 show the experimental results of a cultured 3T3-L1 cell with the addition of 1.0 and 2.0 mM of oleic acid in the culture media. The FWHM of the highlighted lipid droplet is 0.99 μm and 1.74 μm, respectively, as shown in Figure 4.20d and 4.21d.

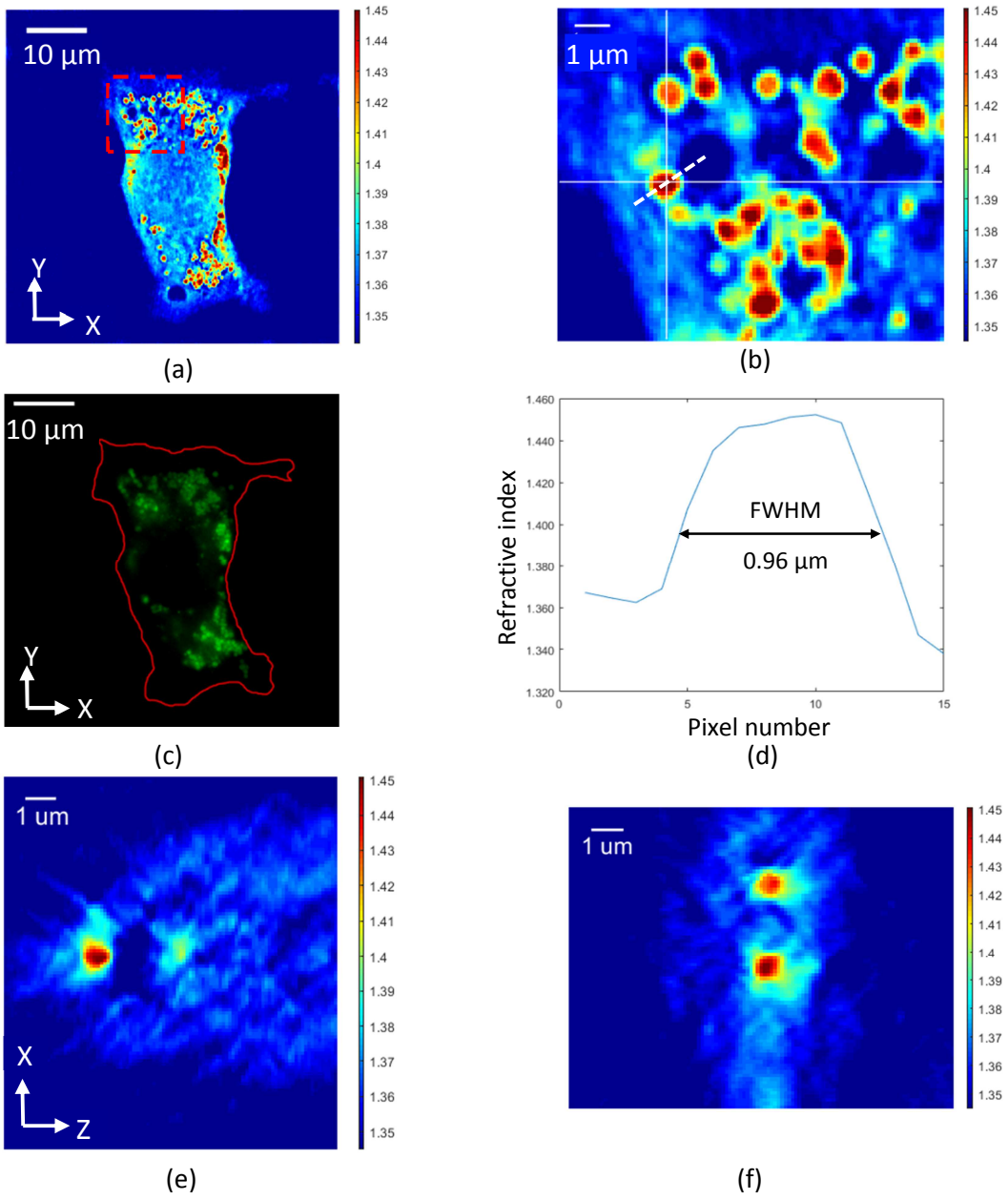

Figure 4.19 Results of a 3T3-L1 cell imaged 20 hours after feeding with 0.5 mM oleic acid: (a) 2D refractive index map of the cell; (b) zoom-in view of the highlighted area in (a); (c) projected fluorescence image of the cell with BODIPY dye for lipid droplet staining; (d) refractive index profile along the dashed line in (b); (e) and (f) are the cross-sectional 2D refractive index map in the X-Z plane and Y-Z plane, respectively, along the horizontal and vertical lines in (b).

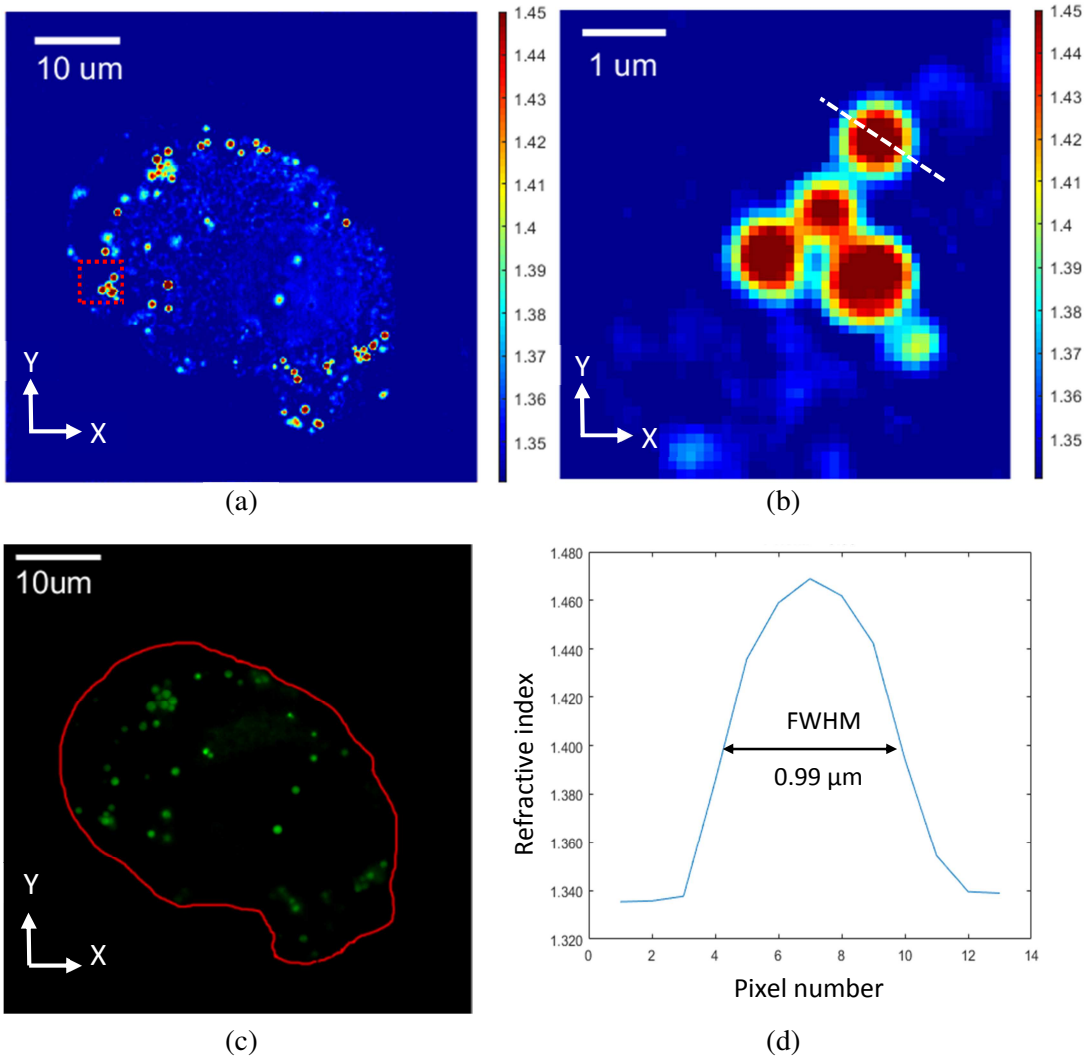

Figure 4.20 Experimental results of a live 3T3-L1 cell imaged 20 hours after feeding with 1.0 mM oleic acid: (a) 2D refractive index map of the cell near the focal plane; (b) zoom-in view of the highlighted area in (a); (c) projected fluorescence image of the cell with BODIPY dye for lipid droplet staining; and (d) refractive index profile along the dashed line in (b).

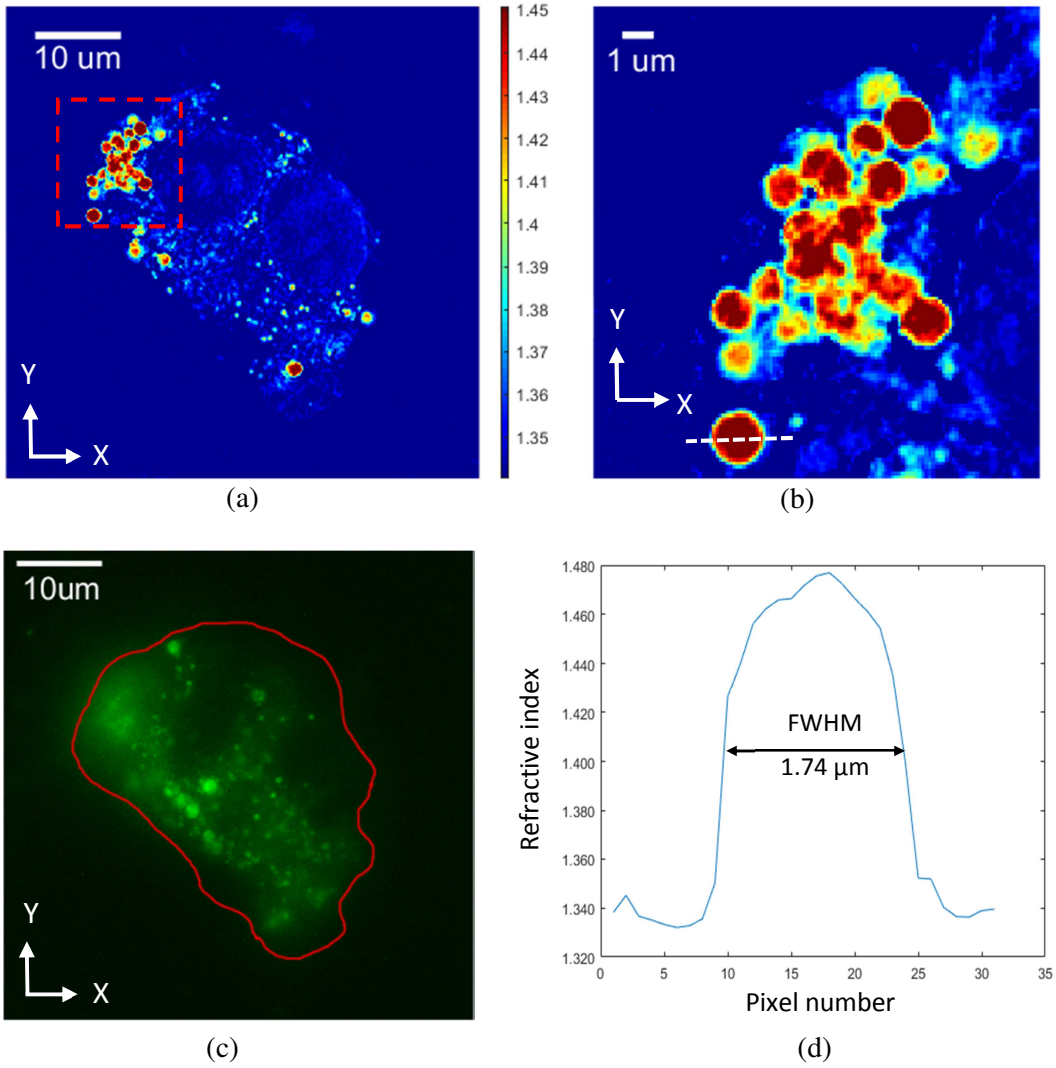

Figure 4.21 Experimental results of a live 3T3-L1 cell imaged 20 hours after feeding with 2.0 mM oleic acid: (a) 2D refractive index map of the cell near the focal plane; (b) zoom-in view of the highlighted area in (a); (c) projected fluorescence image of the cell with BODIPY dye for lipid droplet staining; and (d) refractive index profile along the dashed line in (b).

Superposition of Refractive Index Map and Fluorescence Image

To identify and analyze the lipid droplets generated by the 3T3-L1 cells in natural culture condition and under the stimulation of 0.5, 1.0 and 2.0 mM oleic acid in the culture medium, the 2D refractive index maps near the focal plane are compared with the corresponding projected fluorescence images. It should be pointed out that the fluorescence image of the sample may be focused at the layer of the cell, which may not be the same layer of the 2D refractive index map. In addition, the fluorescence image is a projected 2D image, which includes the fluorescence of lipid droplets from all layers within the depth of view of the system. Therefore, the fluorescence image can only match with 2D refractive index maps in which the focal plane is near to that of the fluorescent image.

Figure 4.22 demonstrates the superposition of the 2D refractive index map with the fluorescence image of a 3T3-L1 cell without the addition of oleic acid in the culture medium. Figure 4.22a is the cross-sectional 2D refractive index map near the focal plane of the cell. Figure 4.22b is a unicolor/pseudo-color version of the same refractive index map in Figure 4.22a, which is basically a grey level refractive index level for easy visualization in the superposition image. From Figures 4.22a or 4.22b, we can see lipid droplets, which have higher refractive index. Figure 4.22c is the projected fluorescence image of the whole cell, showing

lipid droplets in different layers of the cell. Those not in the focal plane of the imaging system have lower fluorescence intensity and are dimmer. For those beyond the depth of view of the imaging system, their fluorescence will not be seen and captured at the focal plane. Figure 4.22d is the superimposed result of Figures 4.22b and c. The yellow color is the resultant color of the superposition lipid droplets appeared in both images. Green color granular particles are some hydrophobic elements thus without corresponding high refractive index counterparts. Note from both the highlighted areas in Figures 4.22c and d, it is interested to see that those lipid droplets deem in fluorescence image but still quite clear in the 2D refractive index map, which suggests that the 2D map sliced from 3D refractive index map with ODT technology is an effective method for lipid droplet study. Without any labeling/staining, we can retrieve 3D refractive index information of the lipid droplets in the cell, which is a measure of the dry mass and mass density. Figure 2.23 to Figure 2.25 show exactly the same types of images for different stimulation conditions of 0.5, 1.0 and 2.0 mM oleic acid. Except that at the condition of 2.0 mM, the quality of both the 2D map and the fluorescence images are worse.

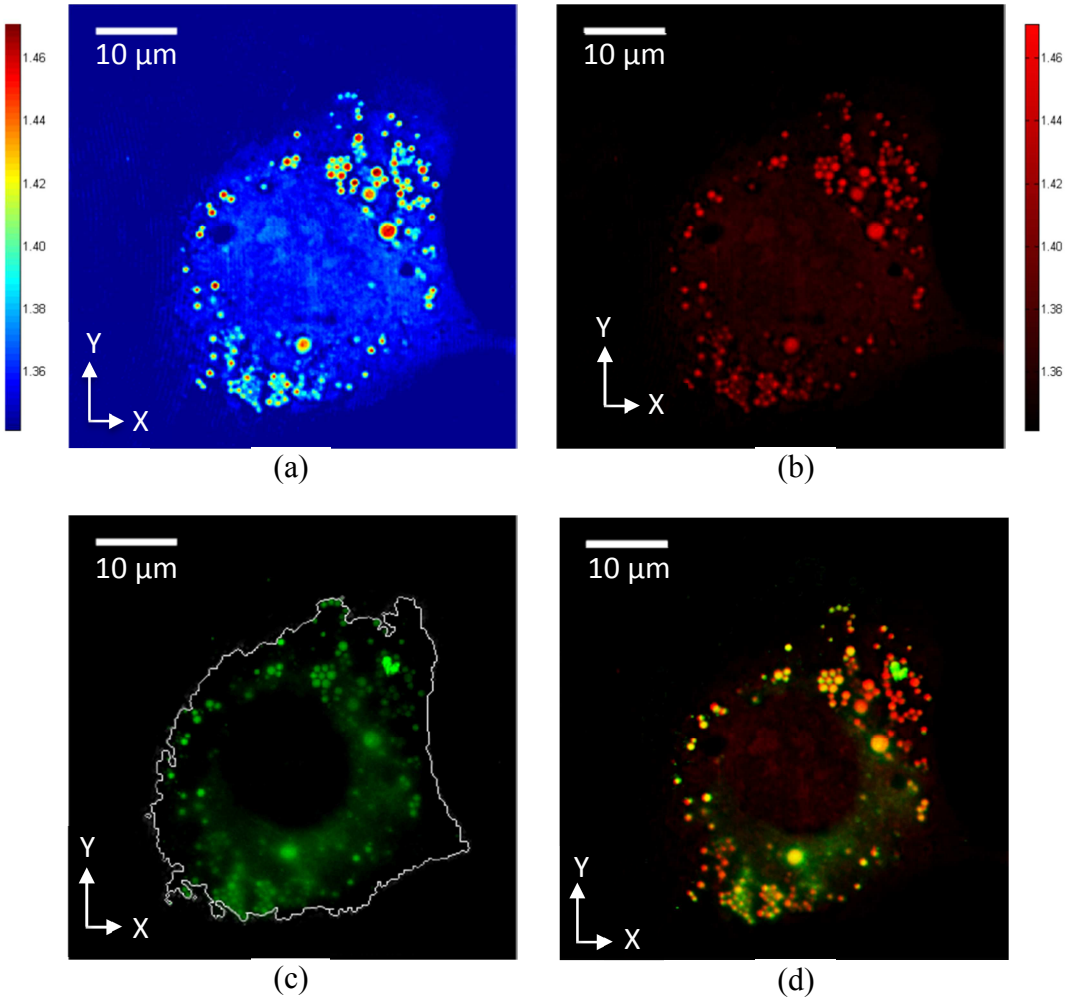

Figure 4.22 Superposition of the 2D refractive index map and the fluorescence image of a cultured 3T3-L1 cell without addition of oleic acid: (a) cross-sectional 2D refractive index map; (b) unicolor/pseudo-color version of the same refractive index map in (a); (c) the projected fluorescence image of the whole cell stained with BODIPY dye; and (d) superposition image of (b) and (c).

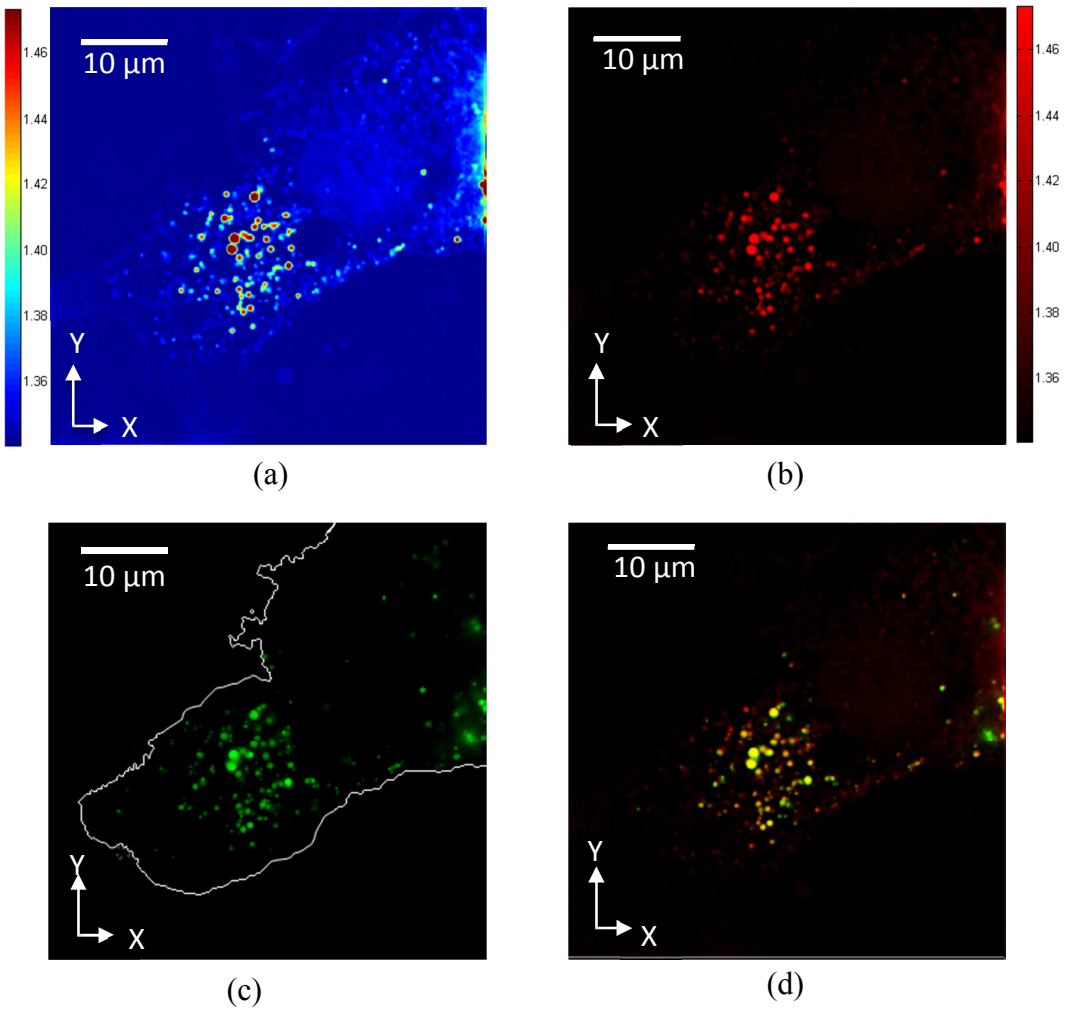

Figure 4.23 Superposition of the 2D refractive index map and the fluorescence image of a cultured 3T3-L1 cell imaged 20 hours after adding 0.5 mM oleic acid in the culture medium: (a) cross-sectional 2D refractive index map; (b) unicolor/pseudo-color version of the same refractive index map in (a); (c) the projected fluorescence image of the whole cell stained with BODIPY dye; and (d) superposition image of (b) and (c).

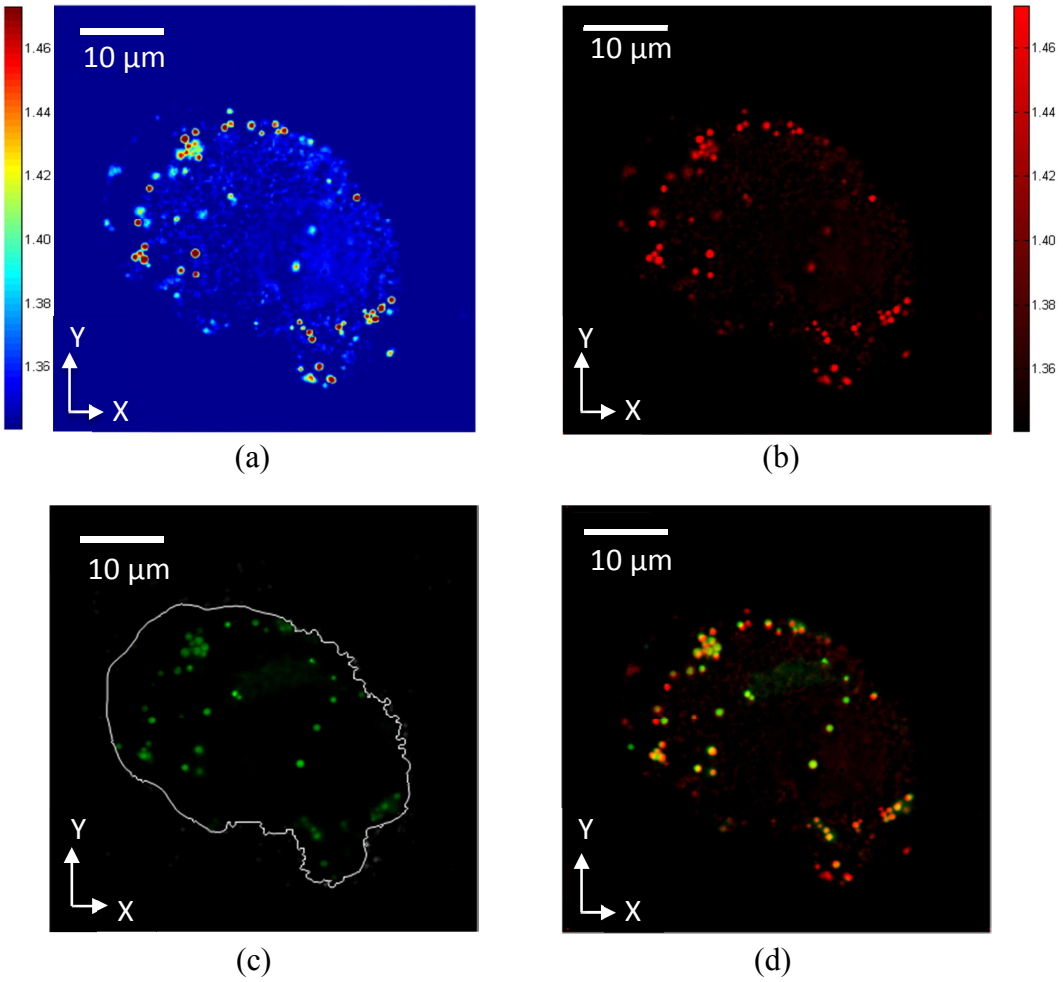

Figure 4.24 Superposition of the 2D refractive index map and the fluorescence image of a cultured 3T3-L1 cell imaged 20 hours after adding 1.0 mM oleic acid in the culture medium: (a) cross-sectional 2D refractive index map; (b) unicolor/pseudo-color version of the same refractive index map in (a); (c) the projected fluorescence image of the whole cell stained with BODIPY dye; and (d) superposition image of (b) and (c).

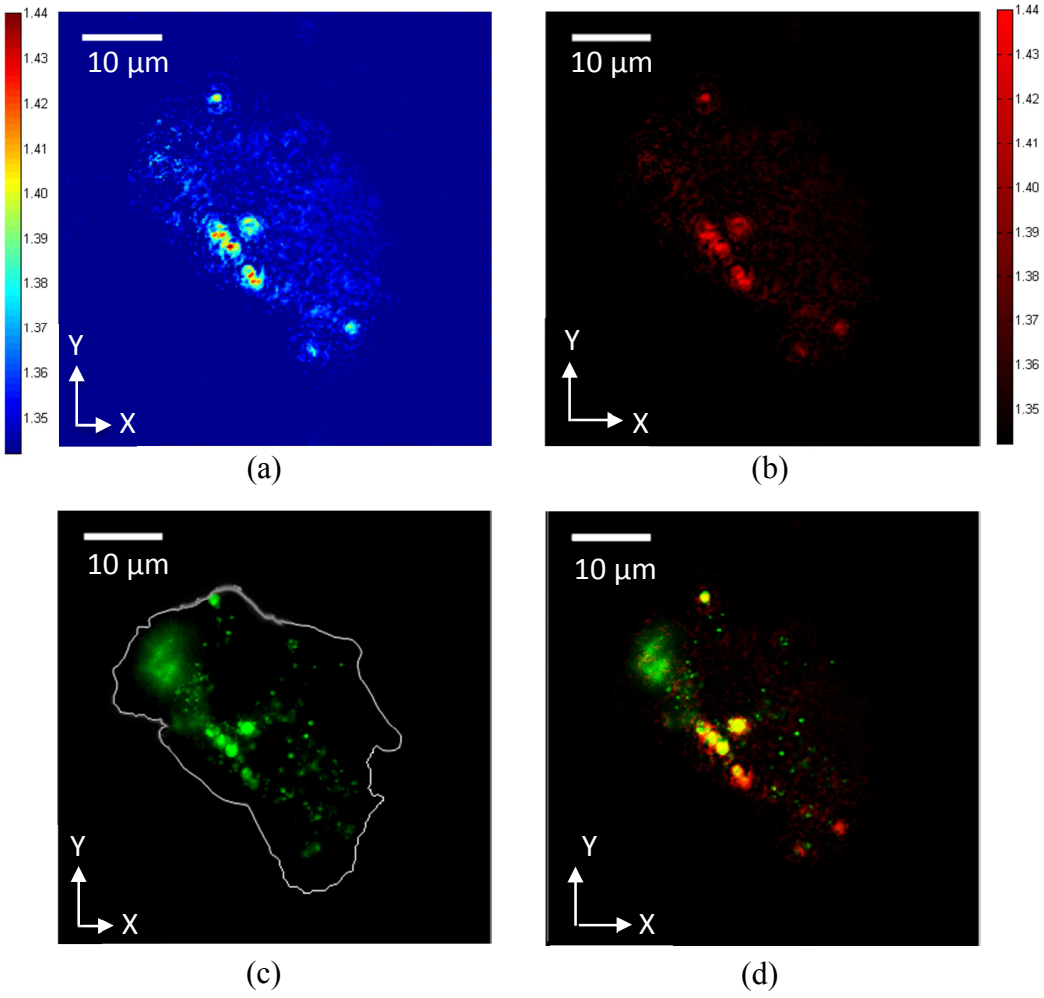

Figure 4.25 Superposition of the 2D refractive index map and the fluorescence image of a cultured 3T3-L1 cell imaged 20 hours after adding 2.0 mM oleic acid in the culture medium: (a) cross-sectional 2D refractive index map; (b) unicolor/pseudo-color version of the same refractive index map in (a); (c) the projected fluorescence image of the whole cell stained with BODIPY dye; and (d) superposition image of (b) and (c).

Analysis of Size Population and Refractive Index of Lipid Droplets

The lipid droplets in 3T3-L1 cells under excessive oleic acid stimulations are studied based on the refractive index distribution of the corresponding droplet populations, which is shown in Figure 4.26. It shows that the refractive indices of lipid droplets without addition of oleic acid cover a comparative wide range shown in Figure 4.26a. It indicates that the mass densities of lipid droplets have significant differences. Figures 4.26b, c and d are the refractive index distributions of lipid droplet populations for 3T3-L1 cells fed with excessive oleic acid with concentrations of 0.5, 1.0 and 2.0 mM, respectively. It can be seen that when oleic acid concentration increases, the refractive indices of the two highest droplet populations increase.

In order to present the increasing trend of the refractive index, the same batches of data are processed in another approach, i.e. bar charts in Figure 4.27 with interval of 0.005 RIU which matches the estimated sensitivity of the system, displayed. For the curve shown in Figure 4.27a, the refractive index with largest number of lipid droplets is about 1.425. With the addition of oleic acid concentration of 0.5, 1.0 and 2.0 mM, the refractive index with largest number of lipid droplets is about 1.445, 1.440 and 1.455, respectively. With the addition of oleic acid in the culture

Such correlation between refractive index and fatty acid concentration might be useful to establish the connection between refractive index of lipid droplets and changes in their mass density as well as composition, which can be further investigated with respect to their roles in metabolism and biological pathways.

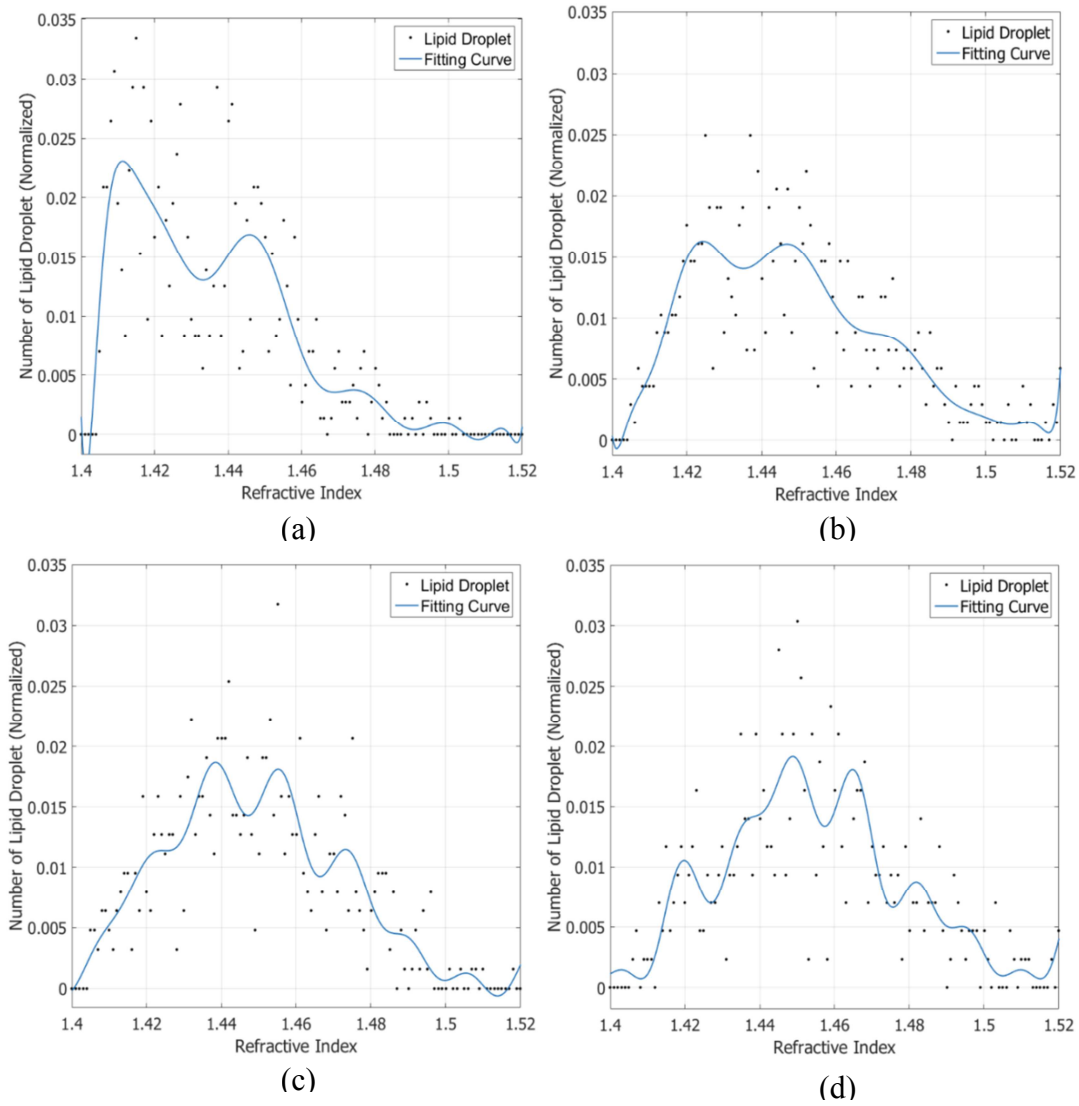

Figure 4.26 Refractive index distributions of lipid droplets in fully cultured live 3T3-L1 cells under different micro-environmental stimulation conditions: (a) at normal culture condition; 20 hours after adding oleic acid in the culture medium with the concentrations of (b) 0.5 mM; (c) 1.0 mM; and (d) 2.0 mM respectively.

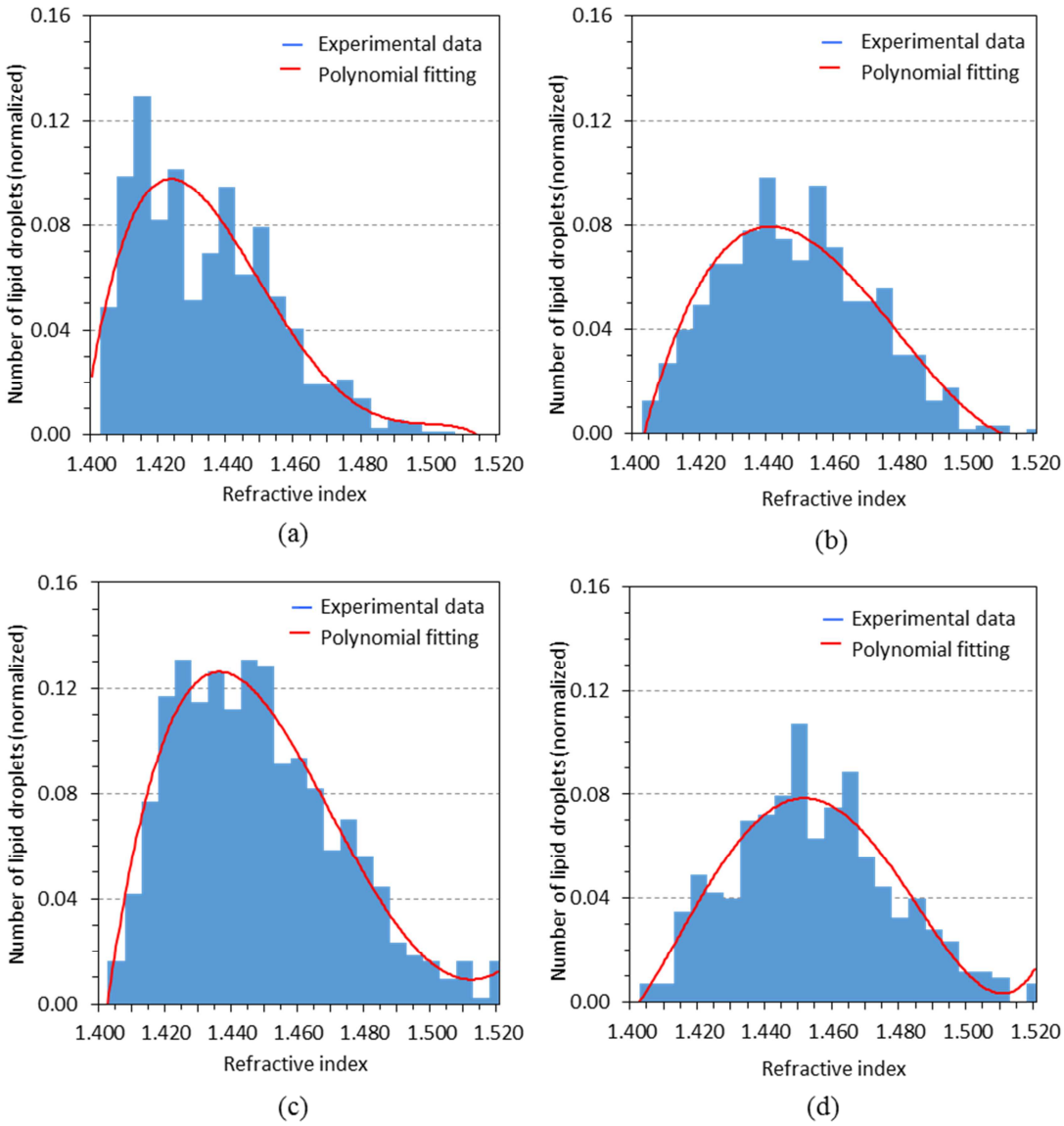

Figure 4.27 the same refractive index distributions of lipid droplets in 3T3-L1 cells versus droplets numbers. Considering the system's sensitivity is at ±0.005 RIU, the increment of the bar chart is selected at 0.005. The curves are generated with the same batches of data used in Figure 4.22 with concentrations of added oleic acid being: (a) 0 mM; (b) 0.5 mM; (c) 1.0 mM and (d) 2.0 mM respectively.

Figure 4.28 demonstrated the lipid droplet distribution in term of size and refractive index with the same four batches of data. The density contour plots in Figure 4.29 illustrate clearly the lipid droplet population distribution in precisely divided grids of size versus refractive indices of lipid droplets. The lipid droplets are grouped with a grid resolution of 0. 1 μm and 0.005 RIU. Comparing with the 2D density distributions shown in Figure 4.28, the density contour maps convey clearer information on the droplet population regarding to their sizes and refractive indices. Without the addition of oleic acid (Figure 4.29a), there are two sub-populations of lipid droplets. One is smaller in size (0.70 μm) with lower refractive index (1.420), and another is larger in size (0.85 μm) with higher refractive index (1.440). With the addition of oleic acid, the sub-populations are changed and ultimately merged into a single population (Figure 4.29d) with a peak size and refractive index of 0.70 μm and 1.445, respectively. The addition of oleic acid in the culture medium of 3T3-L1 cells, indeed, increases the refractive index of lipid droplets, which may be caused by the change in composition and density. Further analysis can be performed by analyzing the composition of lipid droplets by mass spectrometry and correlate it with the measured refractive index, which is important to understand the roles and functions of lipid droplets in various biological and biomedical mechanisms.

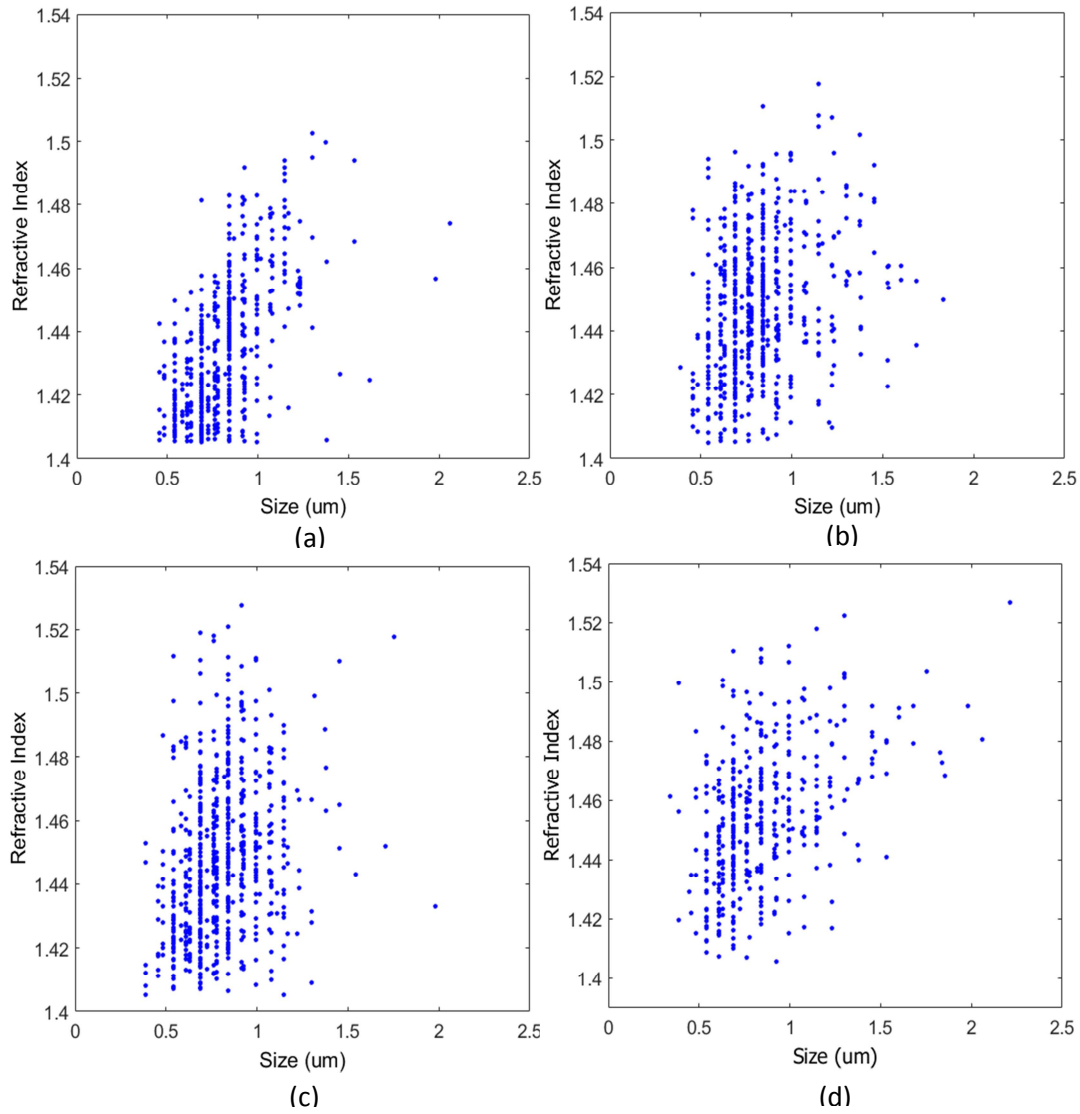

Figure 4.28 Size and refractive index population of lipid droplets in cultured live 3T3-L1 cells under different conditions: (a) at normal culture condition; 20 hours after adding oleic acid with concentrations of (b) 0.5 mM; (c) 1.0 mM; and (d) 2.0 mM oleic acid in the culture medium.

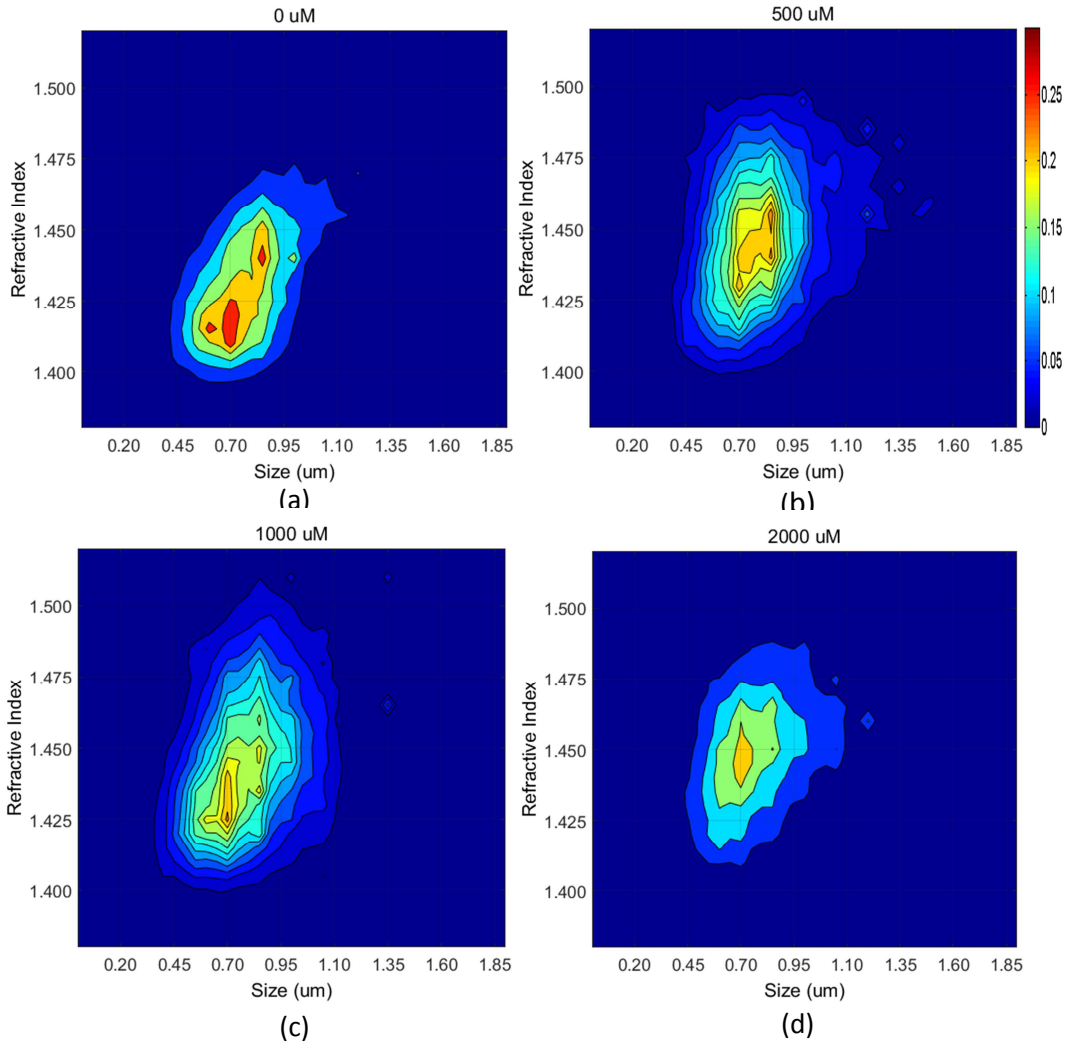

Figure 4.29 Lipid droplet density contours in terms of size and refractive index of cultured 3T3-L1 cells under different stimulation conditions: (a) at normal culture condition; 20 hours after adding oleic acid in the culture medium with concentration of (b) 0.5 mM; (c) 1.0 mM; and (d) 2.0 mM respectively.

Finally, to provide a general idea of the measured lipid droplets for their refractive indices, mean refractive index values of large numbers of lipid droplets are

included in Table 4.2 together with their standard deviation. For each lipid droplet, volumetric average value of is used as its refractive index.

Table 4.2 Average refractive index of lipid droplets when different concentrations of oleic acid are added into the culture medium

Oleic acid concentration (mM)	Refractive index (mean ± standard deviation)	Lipid droplet number
0.0	1.433 ± 0.020	718
0.5	1.448 ± 0.022	630
1.0	1.448 ± 0.025	682
2.0	1.454 ± 0.023	428

4.4.4 Discussions

With the customized ODT system, the quantification of refractive index distribution of live cells with sub-cellular resolution is demonstrated. By combining the high resolution of 3D refractive index mapping using the ODT system with integrated function of fluorescence imaging, it is possible to study both the refractive index of lipid droplets and the dynamic cellular structures that lipid droplets reside in. More in-depth studies can be done to investigate the

dynamic changes that occur in morphology and traits of lipid droplets in diseased cells or by altering the external conditions.

Refractive index is a fundamental biophysical parameter that is related to fatty chain, chain length and degree of unsaturation. Based on this relationship, refractive index correlates to fatty acid composition, which is a new biophysical parameter for biological and disease studies. On the other hand, the ODT system with integrated fluorescence imaging is not limited to the study of lipid droplets, it is applicable for other intracellular organelles that have potential to establish the fundamental investigation of refractive index of various intracellular organelles and correlate with their morphological and biological dynamics.

4.5 Summary

The originality of this work lies in investigation of the refractive index distribution in a single cell, especially in determining the refractive indices of various intracellular organelles. The 3D refractive index maps of mitochondria, nucleus and lipid droplets are determined. The refractive index map/distributions are obtained using a customized ODT system with the exclusive function of fluorescence imaging. Cross section 2D refractive maps of the cell show different organelle has different refractive indices and their geometrical positions are

validated by corresponding fluorescence images, using fluorescence dyes of mitotracer green, SyBr green and BODIPY respectively.

In addition, the refractive indices of lipid droplets under chemical stimulation by adding different concentrations of oleic acid into the culture of 32T3-L1cells are investigated. A large number of lipid droplets are analyzed regarding their refractive indices and sizes. A general trend is that refractive indices of lipid droplets increase when higher concentration of oleic acid is added to the culture medium. It suggests that lipid droplets' mass density is changed under such type of stimulation. This shows that the 3D refractive index mapping obtained with ODT technology has a high potential for biological and biomedical studies to provide 3D intracellular morphological structure as well as mass densities of different organelles.

Chapter 5 Conclusions and Recommendations

5.1 Conclusions

The vast achievements and insights in biology and life sciences in the last century can be attributed to rapid development of modern optical microscopy and fluorescent microscopy. Bioimaging has become the dominant method in biomedical and life sciences, whereby one of the most important physical parameter governing the light-reaction behaviors of cells and other microorganisms is the refractive index. Refractive index can be used to determine other important biophysical parameters and correlate cell metabolic activities such as cell infection and different stages of the cell cycle. Changes of refractive index profile corresponding to changes in fatty acid concentration can also be detected, which might reveal the correlation between the refractive index of cells/bacteria with cell abnormality or preliminary disease detection.

The extensive literature study of refractive index measurement methodologies and findings related to biological and biomedical behaviors of various cell lines and malfunctioned cells have been reported for potential disease diagnosis and other

applications. As the linkage between the refractive index and intracellular functions of organelles is far less clear, this PhD research is targeted to develop new approaches to measure refractive index of individual cells and bacteria so that to build up a database for potential identification method, and cells to study their effects under chemical stimulations.

In this PhD research work, two different approaches have been studied with experimental demonstrations. First approach is the development of an integrated microfluidic immersion refractometer to measure the biophysical parameters specifically, the size, shape and refractive indices of three bacteria species, namely *Echerichia coli, Shigella flexneri* and *Vibrio cholera*. The multifunctional microfluidic device has been realized with soft lithography technology using PDMS material. Together with a phase contrast microscope, effective refractive indices of all three bacteria species are measured. The results show the potential in developing an early-warning system in water monitoring industry based on the biophysical parameters of different bacteria species. The significance of this research work lies not only in establishing a rapid, label-free and low-cost system for detection of single bacteria in drinking water, but also providing a database of dimensions and refractive indices of the bacteria species for further/other optical studies.

The second approach is the experimental study of the refractive index distribution of single cells with focus on intracellular lipid droplets and their responses towards environmental stimulation of increasing fatty acids concentration. This work is achieved using an optical diffraction tomography (ODT) with an integrated function of fluorescence imaging. The 3D refractive index profile of lipid droplets inside an entire cell is measured under the presence of oleic acid with different concentrations. A correlation trend between increasing in fatty acids concentrations and in the mean refractive index value of lipid droplets can be found by intensive data analysis. To the best knowledge of the author, such quantitative 3D biophysical study of lipid droplets has not been reported before. The investigation methodologies are ready for in-depth study of 3D refractive index distributions of other microorganisms and organelles.

5.2 Recommendations for Future Works

For the microfluidic immersion refractometer, more research can be done in the following aspects:

- Increase the measurement speed by upgrading the recording CCD and establishing a recognition software to capture the image where the contrast

between the bacteria/cell and the liquid medium becomes the minimum even when the bacteria is in flow and unstable.

- Design and build a simplified tube or handheld phase contrast microscope to realize the phase contrast function and further reduce the cost and increase the portability.
- Extend the biophysical database by measuring the biophysical parameters of other bacteria species.
- Apply the microfluidic immersion refractometer to other biological samples for other biological and biomedical studies, especially in hematology.
- Integrate the optical system with fluorescent imaging to add another dimension of analysis for more complete and in-depth biological and biomedical studies.

For the methodology 3D cell refractive index distribution measurement, more research work can be done in the following aspects:

- Increase the sensitivity and accuracy of the ODT system by reducing the noise and instability errors of the scanning mirrors and the PZT, the thermal noise of the CCD – replaced with a cool CCD, and the laser speckle induced noise.
- Increase the capturing speed by using a camera with higher speed.
- Increase the reconstruction speed for 2D phase images and 3D refractive index distributions by using FPGA programing and an electronic card with on board parallel image processing.

- The quantitative study of the 3D refractive index profile of intracellular lipid droplets and their variations under microenvironmental stimulation here is only the beginning work along this direction. More detailed measurements and monitoring work can be carry out to unravel the complicated roles of lipid droplets in metabolism and disease processes, and the possible correlation between the composition as well as morphology of lipid droplets and obesity. For example, further research on dysfunctional cells from obese individuals and hepatic steatosis patients can yield more comprehension in the refractive index diference between a normal cell and an unhealthy cell.

In general, with a wide variety of species and the complicity of microorganisms, there will be plenty of feasible and meaningful research work related to quantitative 3D cell refractive index measurements which could be initiated from the literature study and the demonstrated experimental methodology reported in this dissertation.

References

1. P. Y. Liu, L. K. Chin, W. Ser, H. F. Chen, C. M. Hsieh, C. H. Lee, K. –B. Sung, T. C. Ayi, P. H. Yap. B. Liedberg, K. Wang, T. Bourouina and Y. Leprince-Wang,"Cell refractive index for cell biology and disease diagnosis: past, present and future,"*Lab on a Chip*, **16**(4), pp. 634-644, (2016).

2. R. Barer, "Refractometry and interferometry of living cells," *Journal of the Optical Society of America*, **47**, pp. 545-556, (1957).

3. K. Lee, K. Kim, J. Jung, J. Heo, S. Cho, S. Lee, G. Chang, Y. Jo, H. Park and Y. Park, "Quantitative phase imaging techniques for the study of cell pathophysiology: from principles to applications," *Sensors*, **13**(4), pp. 4170-4191, (2013).

4. G. Popescu, "Quantitative phase imaging of cells and tissues." *McGraw Hill Professional*, (2011).

5. B. Bhaduri, C. Edwards, H. Pham, R. Zhou, T. H. Nguyen, L. L. Goddard and G. Popescu, "Diffraction phase Microscopy: principles and applications in materials and life sciences," *Advances in Optics and Photonics*, **6**(1), pp. 57-119, (2014).

6. M. K. Kim, “Principles and techniques of digital holographic Microscopy,” *Journal of Photonics for Energy*, **1**(1), pp. 018005-10~50, (2010).

7. J. W. Su, W. C. Hsu, C. Y. Chou, C. H. Chang and K. B. Sung, “Digital holographic microtomography for high-resolution refractive index mapping of live cells,”*Journal of Biophotonics*, **6**(5), pp. 416-424, (2013).

8. J. B. Bateman, J. Wagman and E. L. Carstensen, “Refraction and absorption of light in bacterial suspensions,” *Kolloid-Zeitschrift und ZeitschriftfürPolymere*, **208**(1), pp. 44-58, (1966).

9. R. Barer and S. Joseph, “Refractometry of living cells part I. basic principles,” *Quarterly Journal of Microscopical Science*, **95**, pp.399-423, (1954).

10. B. Rappaz, P. Marquet, E. Cuche, Y. Emery, C. Depeursinge and P. J. Magistretti, “Measurement of the integral refractive index and dynamic morphometry of living cells with digital holographic Microscopy,” *Optics Express*, **13**, pp. 9361-9373, (2005).

11. G. Popescu, Y. Park, N. Lue, C. Best-Popescu, L. Deflores, R. R. Dasari, M. S. Feld, K. Badizadegan, “Optical imaging of cell mass and growth dynamics,” *American Journal of Physiology - Cell Physiology*, **295**(2), pp. 538-544, (2008).

12. W. Choi, C. Fang-Yen, K. Badizadegan, S. Oh, N. Lue, R. R. Dasari and M. S. Feld "Tomographic phase microscopy," *Nature methods*, **4**, pp.717-719, (2007).

13. K. Haseda, K. KAnematcu, K. Noguchi, H. Saito, N. Umeda and Y. Ohta, "Significant correlation between refractive index and activity of mitochondria: single mitochondrion study," *Biomedical Optics Express*, **6**(3), pp. 859-869, (2015).

14. J. D. Wilson, W. J. Cottrell and T. H. Foster, "Index-of-refraction-dependent subcellular light scattering observed with organelle-specific dyes," *Journal of Biomedical Optics*, **12**(1), pp. 014010-014010, (2007).

15. J. A. Valkenburg and C. L. Woldringh, "Phase separation between nucleoid and cytoplasm in Escherichia coli as defined by immersive refractometry," *Journal of Bacteriology*, **160**(3), pp. 1151-1157, (1984).

16. K. F. A. Ross and E. Billing, "The water and solid content of living bacterial spores and vegetative cells as indicated by refractive index measurements," *Microbiology*, **16**(2), pp. 418-425, (1957).

17. R. K. Bista, S. Uttam, P. Wang, K. Staton, S. Choi, C. J. Bakkenist, D. J. Hartman, R. E. Brand and Y. Liu, "Quantification of nanoscale nuclear refractive index changes during the cell cycle," *Journal of Biomedical Optics*, **16**(7), pp. 070503-070503, (2011).

18. M. Mira, Z. Wang, Z. Shen, M. Bednarz, R. Bashira, I. Golding, S. G. Prasant and G. Popescu, "Optical measurement of cycle-dependent cell growth," *Proceedings of the National Academy of Sciences*, **108**(32), pp. 13124-13129, (2011).

19. D. J. Mason and D. M. Powelson, "Nuclear division as observed in live bacteria by a new technique," *Journal of Bacteriology*, **71**(4), 474, (1956).

20. K. G. Phillips, S. L. Jacques and O. J. T. McCarty, "Measurement of single cell refractive index, dry mass, volume, and density using a transillumination microscope," *Physical Review Letters*, **109**(11), 118105, (2012).

21. A. S. Popel and P. C. Johnson "Microcirculation and Hemorheology," *Annu Rev Fluid Mech*, **37**, pp. 43–69,(2005).

22. I. V. Kolesnikova, S. V. Potapov, M. A. Yurkin, A. G. Hoekstra, V. P. Maltsev and K. A. Semyanov, "Determination of volume, shape and refractive index of individual blood platelets," *Journal of Quantitative Spectroscopy and Radiative Transfer*, **102**(1), pp. 37-45, (2006).

23. D. D. McManus and J. E. Freedman, "MicroRNAs in platelet function and cardiovascular disease," *Nature Reviews Cardiology*, **12**(12), pp. 711-717, (2015).

24. L. Vizioli, S. Muscari and A. Muscari, "The relationship of mean platelet volume with the risk and prognosis of cardiovascular diseases,"*International Journal of Clinical Practice*, **63**(10), pp.1509-1515, (2009).

25. J. T. Daugirdas and A. A. Bernardo, "Hemodialysis effect on platelet count and function and hemodialysis-associated thrombocytopenia," *Kidney International*, **82**(2), pp. 147-157, (2012).

26. A. E. Moskalensky, M. A. Yurkin, A. I. Konokhova, D. I. Strokotov, V. M. Nekrasov, A. V. Chernyshev, G. A. Tsvetovskaya, E. D. Chikova and V. P. Maltsev, "Accurate measurement of volume and shape of resting and activated blood platelets from light scattering," *Journal of Biomedical Optics*, **18**(1), pp. 017001-017001, (2013).

27. J. Yoon, K. Kim, H. Park, C. Choi, S. Jang and Y. Park, "Label-free characterization of white blood cells by measuring 3D refractive index maps," *Biomedical Optics Express*, **6**(10), pp. 3865-3875, (2015).

28. V. P. Maltsev, A. G. Hoekstra and M. A. Yurkin, "Optics of white blood cells: optical models, simulations, and experiments," *Advanced Optical Flow Cytometry: Methods and Disease Diagnoses, First Edition*, Wiley-VCH Verlag GmbH & Co, 2011.

29. K. W. Keohane and W. K. Metcalf, "The cytoplasmic refractive index of lymphocytes, its significance and its changes during active immunization,"

Quarterly Journal of Experimental Physiology and Cognate Medical Sciences, **44**(4), pp. 343-350, (1959).

30. J. G. Wilde and W. K. Metcalf, "Changes in the lymphocyte cytoplasmic refractive index following typhoid vaccination," *Annals of Clinical & Laboratory Science*, **5**(1), pp. 23-26, (1975).

31. K. W. Keohane and W. K. Metcalf, "Changes in lymphocytes during antibody production," *Nature*, **43**(4), pp. 408-418(1959).

32. N. Ghosh, P. Buddhiwant, A. Uppal, S. K. Majumder, H. S. Patel and P. K. Gupta, "Simultaneous determination of size and refractive index of red blood cells by light scattering measurements," *Applied Physics Letters*, **88**(8), 084101, (2006).

33. N. T. Shaked, L. L. Satterwhite, M. J. Telen, G. A. Truskey and A. Wax, "Quantitative Microscopy and nanoscopy of sickle red blood cells performed by wide field digital interferometry," *Journal of Biomedical Optics*, pp. **16**(3), 030506-030506, (2011).

34. K. Haldar, S. Kamoun, N. L. Hiller, S. Bhattacharje and C. van Ooij, "Common infection strategies of pathogenic eukaryotes," *Nature Reviews Microbiology*, **4**(12), pp. 922-931, (2006).

35. I. Weissbuch and L. Leiserowitz, "Interplay between malaria, crystalline hemozoin formation, and antimalarial drug action and design," *Chemical Reviews*, **108**(11), pp. 4899-4914, (2008).

36. Y. Park, M. Diez-Silva, G. Popescu, G. Lykotrafitis, W. Choi, M. S. Feld and S. Suresh, "Refractive index maps and membrane dynamics of human red blood cells parasitized by Plasmodium falciparum," *Proceedings of the National Academy of Sciences*,**105**(37), pp. 13730-13735, (2008).

37. S. Suresh, "Biomechanics and bioPhysics of cancer cells," *ActaMaterialia*, **55**(12), pp. 3989-4014, (2007).

38. J. D. Wilson, W. J. Cottrell and T. H. Foster, "Index-of-refraction-dependent subcellular light scattering observed with organelle-specific dyes," *Journal of Biomedical Optics*, **12**(1), pp. 014010-014010, (2007).

39. W. J. Choi, D. I. Jeon, S.-G.Ahn, J.-H. Yoon, S. Kim and B. H. Lee, "Full-field optical coherence Microscopy for identifying live cancer cells by quantitative measurement of refractive index distribution," *Optics Express*, **18**(22), pp. 23285-23295, (2010).

40. P. Wang, R. Bista, R. Bhargava, R. E. Brand and Y. Liu, "Spatial-domain low-coherence quantitative phase microscopy for cancer diagnosis," *Optics Letters*, **35**(17), pp. 2840-2842, (2010).

41. B. H. Zimm and W. B. Dandliker, "Theory of light scattering and refractive index of solutions of large colloidal particles," *The Journal of Physical Chemistry*, **58**(8), 644-648, (1954).

42. R. A. Flynn, B. Shao, M. Chachisvilis, M Qzkan and S. C. Esener, "Two-beam optical traps: Refractive index and size measurements of microscale objects," *Biomedical Microdevices*, **7**(2), pp. 93-97, (2005).

43. P. S. Tuminello, E. T. Arakawa, B. N. Khare, J. M. Wrobel, M. R. Querry, and M. E. Milham, "Optical properties of Bacillus subtilis spores from 0.2 to 2.5 μm." *Applied Optics*, **36**(13), pp. 2818-2824, (1997).

44. S. Joseph, "Refractometry of fungi," *Journal of Microscopy*, **131**(2), pp. 163-172, (1983).

45. P. Y. Liu, L. K. Chin, W. Ser, T. C. Ayi, P. H. Yap, T. Bourouina and Y. Leprince-Wang, "An optofluidic imaging system to measure the biophysical signature of single waterborne bacteria," *Lab on a Chip*, **14**(21), pp. 4237-4243, (2014).

46. X. J. Liang, A. Q. Liu, C. S. Lim, T. C. Ayi and P. H. Yap, "Determining refractive index of single living cell using an integrated microchip," *Sensors and Actuators A: Physical*, **133**(2), pp. 349-354, (2007).

47. W. Z. Song, X. M. Zhang, A. Q. Liu, C. S. Lim, P. H. Yap and H. M. M. Hosseini, "Refractive index measurement of single living cells using on-chip Fabry-Pérot cavity," *Applied Physics Letters*, **89**(20), 203901, (2006).

48. L. K. Chin, A. Q. Liu, X. M. Zhang, C. S. Lim, J. H. Ng, J. Z. Hao and S. Takahashi, "Differential single living cell refractometry using grating resonant cavity with optical trap," *Applied Physics Letters*, **91**(24), 243901, (2007).

49. H. Pham, H. Ding, N. Sobh, M. Do, S. Patel and G. Popescu, "Off-axis Quantitative phase imaging processing using CUDA: towards real-time applications," *Biomedical Optics Express*, **2**, pp. 1781-1793, (2011).

50. L. Z. Cai, Q. Liu and X. L. Yang, "Generalized phase-shifting interferometry with arbitrary unknown phase steps," *Optical Letters*, **29**(2), pp. 183-185, (2004).

51. Y.-C. Chua, W.-Y.Chang, K.-H.Chen, J.-H.Chen, B.-C.Tsai and K. Y. Hsu, "Full-field refractive index measurement with simultaneous phase-shift interferometry," *Optik-International Journal for Light and Electron Optics*, **125**(13), pp. 3307-3310, (2014).

52. G. Garcia-Sicerquia, W. Xu, S. K. Jericho, P. Klages, M. H. Jericho and H. J. Kreuzer, "Digital in-line holographic microscopy," *Applied Optics* , **45**(5), pp. 836-850, (2006).

53. G. Popescu, Y. Park, W. Choi, R. R. Dasari, M. S. Feld and K. Badizadegan, "Imaging red blood cell dynamics by quantitative phase microscopy," *Blood Cells, Molecules, and Diseases*, **41**, pp. 10-16, (2008).

54. H. V. Pham, B. Bhaduri, K. Tangella, C. Best-Popescu and G. Popescu, "Real-time blood testing using quantitative phase imaging," *PLOS ONE*, **8**(2), p. e55676 (2013).

55. Y. Jo, J. Jung, M. Kim, H, Park, S.-J. Kang and Y. Park. "Label-free identification of individual bacteria using Fourier transform light scattering," *Optics Express*, **23**(12), pp. 15792-15805, 2015.

56. N. Lue, W. Choi, G. Popescu, Z. Yaqoob, K. Badizadegan, R. R. Dasari and M. S. Feld, "Cell Refractometry Using Hilbert Phase Microscopy and Confocal Reflectance Microscopy,"*The Journal of Physical Chemistry A*,**113**(47), pp. 13327-13330, (2009).

57. K. Kim, J. Yoon, S. Shin, S. Y. Lee, S. Yang and Y. Park, "Optical diffraction tomography techniques for the study of cell pathophysiology," *Journal of Biomedical Photonics & Engineering*, **2**(2), 020201-1~15, (2016).

58. J. Bailleul, B, Simon, M. Debailleul, H. Liu and O. Haeberlé "GPU acceleration towards real-time image reconstruction in 3D tomographic diffractive microscopy," *Proceedings of SPIE*, **8437**, p. 843707, (2012).

59. W.-C. Hsu, J.-W.Su, T.-Y.Tseng and K.-B. Sung, "Tomographic diffractive microscopy of living cells based on a common-path configuration," *Optics Letters*, **39**(7), pp. 2210-2213, (2014).

60. Y. Kim, H. Shim, K. Kim, H. Park, J. H. Heo, J. Yoon, C. Choi., S. Jang and Y. Park, "Common-path diffraction optical tomography for investigation of three-dimensional structures and dynamics of biological cells," *Optics Express*, **22**, pp. 10398-10407, (2015).

61. K. Kim, Z. Yaqoob, K Lee, J. W. Kang, Y. C. Hosseini, P. T. C. So and Y Park, "Diffraction optical tomography using a quantitative phase imaging unit," *Opt. Letters*, **39**, pp. 6935-6938, (2014).

62. Y. Sung, W. Choi, C. Fang-Yen, K. Badizadegan, R. R. Dasari and M. S. Feld, "Optical diffraction tomography for high resolution live cell imaging," *Optics Express*, **17**(1), pp. 266-277, (2009).

63. W. Choi, "Tomographic phase microscopy and its biological applications," *3D Research*, **3**(4), pp. 1-11, (2012).

64. F. Charrière, A. Marian, F. Montfort, J. Kuehn and T. Colomb, "Cell refractive index tomography by digital holographic microscopy," *Optical Letters*, **31**(2), pp. 178-180, (2006).

65. K. Kim, K. S. Kim, H. Park, J. C. Ye and Y. Park, " Real-time visualization of 3D dynamic microscopic objects using optical diffraction tomography," *Optics Express*, **21**, pp. 32269-32278, (2013).

66. N. Lue, W. Choi, G. Popescu, K. Badizadegan, R. R. Dasari and M. S. Feld, "Synthetic aperture tomographic phase microscopy for 3D imaging of live cells in translational motion," *Optics Express*, **16**, pp. 16240-16246, (2008).

67. Y. Sung, N. Lue, B. Hamza, J. Martel, D. Irimia, R. R. Dasari, W. Choi, Z. Yaqoob, P. So, "Three-dimensional holographic refractive-index measurement of continuously flowing cells in a microfluidic channel," *Physical Review Applied*, **1**, p.014002, (2014).

68. X. Fan and I. M. White, "Optofluidic microsystems for chemical and biological analysis," *Nature Photonics*, **5**, pp. 591-597, (2011).

69. E. K. Sackmann, A. L. Fulton and D. J. Beebe, "The present and future role of microfluidics in biomedical research," *Nature*, **507**, pp. 181-189, (2014)

70. Y. K. Suh and A. Kang, "A review on mixing in microfluidics," *Micromachines*, **1**, pp. 82-111, (2010).

71. C. W. Shields IV, C. D. Reyes and G. P. López, "Microfluidic cell sorting: a review of the advances in the separation of cells from debulking to rare cell isolation," *Lab on a Chip*, **15**, pp. 1230-1249, (2015)

72. N. T. Huang, H. L. Zhang, M. T. Chung, J. H. Seo and K. Kurabayashi "Recent advancements in optofluidics-based single-cell analysis: optical on-chip cellular manipulation, treatment, and property detection," *Lab on a Chip*, **14**, pp. 1230-1245, (2014).

73. J. Seo and L. P. Lee, "Disposable integrated microfluidics with self-aligned planar microlenses," *Sensors & Actuators B*, **99**, pp. 615-622, (2004).

74. N. C. H. Le, D. V. Dao, R. Yokokawa, J. Wells, and S. Sugiyama, "Design, simulation and fabrication of a total internal reflection (TIR)-based chip for highly sensitive fluorescent imaging," *Journal of Micromechanics & Microengineering*, **17**, pp. 1139-1146, (2007).

75. A. Werber and H. Zeppe, "Tunable microfluidic microlenses," *Applied Optics*, **44**, pp. 3238-3245, (2005).

76. T. A. Zangle and M. A. Teitell, "Live-cell mass profiling: an emerging approach in quantitative biophysics," *Nature Methods*, **11**(12), pp. 1221-1228, 2014.

77. P. Shah, X. Zhu, C. Chen, Y. Hu, C. Z. Li, "Lab-on-chip device for single cell trapping and analysis," *Biomedical Microdevices,* **16**(1), pp. 35-41, (1965).

78. Y. F. Chen, L. Jiang, M. Mancuso, A. Jain, V. Oncescu, D. Erickson "Optofluidic opportunities in global health, food, water and energy," *Nanoscale*, **4**(16), pp. 4839-4857, (2012).

79. MLA style: "The Nobel Prize in Physics 1953, "*Nobelprize.org*., Nobel Media AB , 2016. <http://www.nobelprize.org/educational/physics/microscopes/phase>

80. R. Barer, K. F. A. Ross and S. Tkaczyk, "Refractometry of living cells," *Nature*, **171**, pp. 720-724, (1953).

81. R. Barer, "Interference Microscopy and mass determination," *Nature*, **169**, pp. 366-367, (1952).

82. W. Z. Song, A. Q. Liu, S. Swaminathan, C. S. Lim, P. H. Yap and T. C. Ayi, "Determination of single living cell's dry/water mass using optofluidic chip," *Applied Physics Letters*, **91**(22), 223902, (2007).

83. M.-C. Kim, B.-C. Isenberg, J. Sutin, A. Meller, J. Y. Wong and C. M. Klapperich, "Programmed trapping of individual bacteria using micrometre-size sieves," *Lab on a Chip*, **11**(6), pp. 1089-1095, (2011).

84. H. M. Xia, S. Y. M. Wan, C. Shu and Y. T. Chew, "Chaotic micromixers using two-layer crossing channels to exhibit fast mixing at low Reynolds numbers*," Lab on a Chip*, **5**(7), pp. 748-755, (2005).

85. L. K. Chin, A. Q. liu, Y. C. Soh, C. S. Lim and C. L. Lin, "A reconfigurable optofluidic Michelson interferometer using tunable droplet grating," *Lab on a Chip*, **10**(8), pp. 1072-1078, (2010).

86. F. D. Bryant, B. A. Seiber, P. Latimer, "Absolute optical cross sections of cells and chloroplasts," *Archives of Biochemistry and Biophysics*, **135**, pp. 97-108, (1969).

87. L. Heijnen and G. Medema, "Method for rapid detection of viable Escherichia coli in water using real-time NASBA," *Water Research*, **43**(12), pp. 3124-3132, (2009).

88. C. J. Mann, L. Yu, C. M. Lo and M. K. Kim, "High-resolution quantitative phase contrast Microscopy by digital holography," *Optics Express*, **13**, pp. 8693-8697, (2005).

89. D. M. Gill, W. M. J. Green, C. Xiong, A. Rylyakov, C. Schow, J. Proesel, J. C. Rosenberg, T. Barwicz, M. Khater, S. Assefa, S. M. Shank, c. Reinholm, E. Kiewra, S. Kamlapurkar and Y. A. Vlasov, "Distributed electrode Mach-Zehnder modulator with double-pass phase shifters and integrated inductors," *Optics Express*, **23**(13), pp. 16857-16865, (2015).

90. G. R. Toker, "Holographic Interferometry: A Mach–Zehnder Approach," *CRC Press*, (2012).

91. S. Verma, Y. M. Joshi and K. Muralidhar, "Optical Interferometers: Principles and applications in transport phenomena," Interferometry-Principles and Applications, Edited by Mark E. Russo, *Nova Publishers*, USA. ISBN, 978-1.

92. D. Gabor and W. P. Goss, "Interference microscope with total wavefront reconstruction," *Journal of Optical Society of America*, **56**(7), pp. 849-858, (1966).

93. T. Kim and H. Kim, "Phase sensitivity of a quantum Mach-Zehnder interferometer for a coherent state input," *Journal of Optical Society of America*, **26**(4), pp. 671-675, (2009).

94. M. G. A. Paris, "Entanglement and visibility at the output of a Mach-Zehnder interferometer," *Physical Review A*, **59**(2), 1615, (1999).

95. D. Gabor, G. W. Stroke, D. BrummA. , Funkhouser and A. Labeyrie, "Reconstruction of phase objects by holography," *Nature*, **208**, pp. 1159-1162 (1965).

96. L. Ying, "Phase unwrapping," *Wiley Encyclopedia of Biomedical Engineering*, **6**, Ed. *MetinAkay, Wiley*, (2006).

97. D. C. Ghiglia and M. D. Pritt, "Two-dimensional phase unwrapping: Theory, algorithms and software," *John Wiley & Sons*, New York, (1998).

98. B. Qi, L. Qian, A. Tausz and H. K. Lo, "Frequency-shifted Mach-Zehnder interferometer for locating multiple weak reflections along a fiber link," *IEEE Photonics Technology Letters*, **18**(1), pp. 295-297, (2006).

99. Y. Surrel, "Design of algorithms for phase measurements by the use of phase stepping," *Applied Optics*, **35**(1), pp. 51-60, (1996).

100. S. Lai, B. King and M. A. Neifeld, "Wave front reconstruction by means of phase-shifting digital in-line holography," *Optics Communications*, **173**, pp. 155-160, (2000).

101. J. E. Greivenkamp, "Generalized data reduction for heterodyne interferometry," *Optical Engineering*, **23**(4), pp. 234350-234350, (1984).

102. G. Stoilov and T. Dragostinov, "Phase-stepping interferometry: five-frame algorithm with an arbitrary step," *Optics and Lasers in Engineering*, **28**(1), pp. 61-69, (1997).

103. J. Navák, P. Navák and A. Mikš, "Multi-step phase-shifting algorithms insensitive to linear phase shift errors," *Optics Communications*, **281**, pp. 5302-5309, (2008).

104. L. Z. Cai, Q. Liu and X. L. Yang, "Phase-shift extraction and wave-front reconstruction in phase-shifting interferometry with arbitrary phase steps," *Optics Letters*, **28**(19), pp. 1808-1810, (2003).

105. Z. Wang and B. Han, "Advanced iterative algorithm for phase extraction of randomly phase-shifted interferograms," *Optics Letters*, **29**(14), pp. 1671-1673, (2004).

106. E. Wolf, "Three-dimensional structure determination of semi-transparent objects from holographic data," *Optics Communications*, **1**, pp. 153-156, (1969).

107. R. Dändliker and K. Weiss, "Reconstruction of the three-dimensional refractive index from scattered waves," *Optics Communications*, **1**(7), pp. 323-328, (1970).

108. I. Bergoënd, C. Arfire, N. Pavilon and C. Depeursinge, "Diffraction tomography for biological cells imaging using digital holographic Microscopy," *Proceedings of SPIE*, **7376**, p. 737613. (2010).

109. R. Wang, H. Ding, M. Mir, K. Tangella and G. Popescu, "Effective 3D viscoelasticity of red blood cells measured by diffraction phase Microscopy," *Biomedical Optics Express*, **2**(3), pp. 485-490. (2011).

110. B. Simon, M. Debailleul, V. Georges, V. Lauer and O. Haeberlé, "Tomographic diffractive Microscopy of transparent samples," *European Physical Journal applied Physics*, **44**, pp. 29-35, (2008).

111. S. Shin, K. Kim, T. Kim, J. Yoon, K. Hong, J. Park and Y. Park, "Optical diffraction tomography using a digital micromirror device for stable

measurements of 4D refractive index tomography of cells,"*International Society for Optics and Photonics*, p. 971814, (2016).

112. A. C. Kak and M. Slaney, "Principles of computerized tomographic imaging." *IEEE Press*, New York, (1987).

113. P. Müller, M. S. Schürmann, and J. Guck, "The Theory of Diffraction Tomography," *arXiv preprint arXiv*: 1507.00466, (2015).

114. T. Fujimoto and R. G. Parton, "Not just fat: the structure and function of the lipid droplet,"*Cold Spring Harbor Perspectives in Biology*, **3**(3), a004838, (2011).

115. M. Nagayama, T. Uchida and K. Gohara, "Temporal and spatial variations of lipid droplets during adipocyte division and differentiation," *Journal of Lipid Research,* **48**(1), pp. 9-18, (2007).

116. T. C. Walther and R. V. Farese Jr, "Lipid droplets and cellular lipid metabolism," *Annual Review of Biochemistry*, **81**, p. 687, (2012).

117. F. Boschi, V. Rizzatti, M. Zamboni and A. Sbarbati, "Models of lipid droplets growth and fission in adipocyte cells," *Experimental Cell Research*, **336**(2), pp. 253-262, (2015).

118. A. R. Thiam, R. V. Farese Jr and T. C. Walther, "The biophysics and cell biology of lipid droplets," *Nature Reviews Molecular Cell Biology*, **14**(12), pp. 775-786, (2013).

119. Q.Gao and J. M. Goodman, "The lipid droplet—a well-connected organelle," *Frontiers in Cell and Developmental Biology*,**3**, pp. 49(2015).

120. L. M. Burke, B. Kiens and J. L. Ivy, "Carbohydrates and fat for training and recovery," *Journal of Sports Sciences*, **22**(1), pp. 15-30, (2004).

121. J. Hu, Z. Zhang, W. J. Shen and S. Azhar, "Cellular cholesterol delivery, intracellular processing and utilization for biosynthesis of steroid hormones,"*Nutrition & Metabolism*, **7**(1), 1, (2010).

122. T. Fujimoto, Y. Ohsaki, J. Cheng, M. Suzuki and Y. Shinohara, "Lipid droplets: a classic organelle with new outfits," *Histochemistry and Cell Biology*, **130**(2), pp. 263-279, (2008).

123. E. L. Arrese, F. Z. Saudale and J. L. Soulages, "Lipid droplets as signalling platforms linking metabolic and cellular functions," *Lipid Insights*, **7**, pp. 7-16(2014).

124. V. L. Clark and J. A. Kruse, "Clinical methods: the history, physical, and laboratory examinations," *Journal of the American Medical Association*, **264**(21), pp. 2808-2809, (1990).

125. G. van Meer, "Caveolin, cholesterol, and lipid droplets." *The Journal of Cell Biology*, **152**(5), pp. F29-F34, (2001).

126. K. Reue, "A thematic review series: lipid droplet storage and metabolism: from yeast to man," *Journal of Lipid Research,* **52**(11), pp. 1865-1868, (2011).

127. M. B. Rone, J. Fan and V. Papadopoulos, "Cholesterol transport in steroid biosynthesis: role of protein–protein interactions and implications in disease states,"*Biochimica et Biophysica Acta (BBA)-Molecular and Cell Biology of Lipids*, **1791**(7), pp. 646-658, (2009).

128. R. C. Melo and A. M. Dvorak, "Lipid body–phagosome interaction in macrophages during infectious diseases: host defense or pathogen survival strategy," *PLOS Pathogens*, **8**(7), e1002729, (2012).

129. U. J. Jung and M. S. Choi, "Obesity and its metabolic complications: the role of adipokines and the relationship between obesity, inflammation, insulin resistance, dyslipidemia and nonalcoholic fatty liver disease," *International Journal of Molecular Sciences*, **15**(4), pp. 6184-6223, (2014).

130. J. Finkelstein, M. T. Heemels, S. Shadan and U. Weiss, "Lipids in health and disease," *Nature*, **510**(7503), pp. 47-47, (2014).

131. E. M. Brunt, "Pathology of fatty liver disease," *Modern Pathology*, **20**, pp. S40-S48, (2007).

132. N. Krahmer, R. V. Farese and T. C. Walther, “Balancing the fat: lipid droplets and human disease.” *EMBO Molecular Medicine*, **5**(7), pp. 973-983, (2013).

List of Publications

Journal Papers

1. P. Y. Liu, L. K. Chin, W. Ser, T. C. Ayi, P. H. Yap, T. Bourouina and Y. Leprince-Wang, "*An optofluidic imaging to measure the biophysical signature of single waterborne bacterium*," Lab on a Chip, **14**, pp. 4237-4243, 2014.

2. P. Y. Liu, L. K. Chin, W. Ser, H. F. Chen, C.-M. Hsieh, C.-H. Lee, K.-B. Sung T. C. Ayi, P. H. Yap, B. Liedberg, K. Wang, T. Bourouina and Y. Leprince-Wang, "*Cell Refractive Index for Cell Biology and Disease Diagnosis: Past, Present and Future*," Lab on a Chip, **16**, pp. 634-644, 2016. (**Invited paper and cover page**)

3. P. Y. Liu, C.-M. Hsieh, L. K. Chin, W. Ser, K. Wang, T. Bourouina and Y. Leprince-Wang, "*The refractive index measurements of lipid droplets under fatty acid stimulation using an optical diffraction tomographic system*," Lab on a Chip (In preparation).

Conference Papers

1. P. Y. Liu, L. K. Chin, W. Ser, T. C. Ayi, E. P. H. Yap, T. Bourouina and Y. Leprince-Wang, "Optofluidic detection for virus infection monitoring using effective refractive index," Conference on Lasers and Electro-Optics (CLEO 2015), San Jose, United States.

2. P. Y. Liu, L. K. Chin, W. Ser, T. C. Ayi, W. M. Ho, P. H. Yap, Y. Leprince-Wang and T. Bourouina, "A single living bacterium's refractive index measurement by using optofluidic immersion refractometry," 17th International Conference on Miniaturized Systems for Chemistry and Life Sciences (μTAS2013) Freigburg, Germany.

3. P. Y. Liu, L. K. Chin, W. Ser, T. C. Ayi, W. M. Ho, P. H. Yap, Y. Leprince-Wang and T. Bourouina, "Real-time measurement of living bacteria's refractive index using optofludic immersion refractometry," The 6th International Symposium on Microchemistry and Microsystems (ISMM 2014), Singapore. (Oral Presentation)

4. P. Y. Liu, L. K. Chin, W. Ser, T. C. Ayi, W. M. Ho, P. H. Yap, Y. Leprince-Wang and T. Bourouina, "Real-time measurement of single bacterium's refractive index using optofluidic immersion refractometry," The 28th European Conference on Solid-State Transducers (EUROSENSORS 2014), Brescia, Italy.

Résumé Long

Les grandes découvertes et les connaissances en biologie et en sciences de la vie engrangées au cours du siècle dernier peuvent être attribuées en grande partie à un développement rapide de la microscopie optique moderne et la microscopie à fluorescence. L'imagerie microscopique est devenue la méthode dominante dans les sciences biomédicales et de la vie. Dans ce contexte, le paramètre physique le plus important qui régit le comportement à la lumière la réaction de cellules et d'autres micro-organismes est l'indice de réfraction. Il peut être utilisé pour déterminer en tant que paramètre biophysique ou pour une mise en corrélation avec d'autres paramètres biophysiques importants tels que la masse sèche, la masse humide et l'élasticité. L'indice de réfraction peut être également utilisé pour étudier les activités métaboliques des cellules telles que l'infection de cellules et de différents stades du cycle cellulaire.

Comme le rôle de l'indice de réfraction et son lien avec les cellules/bactéries et les fonctions intercellulaires ne sont pas encore très bien comprises, cette thèse vise à développer de nouvelles approches pour la mesure de l'indice de réfraction des cellules individuelles et des bactéries. Tout d'abord, un dispositif de réfractométrie microfluidique sur puce a été conçu et réalisé ; il s'est avéré efficace pour la caractérisation rapide de bactéries/cellules isolées. Dans un

second temps, un système de tomographie par diffraction optique intégré avec l'imagerie par fluorescence a été appliqué pour déterminer la distribution 3D de l'indice de réfraction au sein d'une cellule biologique, celle de gouttelettes lipidiques au sein d'une cellule pour fournir un moyen précis d'étudier les organelles intracellulaires et leurs réponses à des changements environnementaux.

Cette thèse est organisée en cinq chapitres comme suit,

Chapitre 1 Introduction

Cette introduction porte sur la motivation, l'objectif et les principales contributions de ces travaux de thèse. Notre démarche est motivée par l'importance potentielle de l'indice de réfraction d'une seule cellule/bactérie ainsi que la distribution intracellulaire de ce paramètre, qui a de forts liens avec de nombreuses fonctions cellulaires ainsi que certains processus dynamiques de maladies. Une telle étude permettrait l'établissement de modèles percutants pour des pathologies, leur développement, leur diagnostic ainsi que leur détection à un stade précoce.

L'objectif principal de cette thèse est d'étudier et de déterminer l'indice de réfraction des cellules individuelles et des bactéries, en commençant par une valeur effective de l'indice, étendue ensuite à une cartographie intracellulaire de l'indice de réfraction. Tout d'abord, une plateforme microfluidique de réfractométrie par immersion est développé pour manipuler les cellules bactériennes / ciblées et

mesurer l'indice de réfraction effectif de cellules bactériennes / individuelles. Le dispositif microfluidique intègre différentes fonctions microfluidiques dans la puce pour faciliter la manipulation de l'échantillon comprenant d'une part, le piégeage des bactéries, et d'autre part, la modulation de la solution tampon grâce à un mélange de fluides permettant ainsi d'ajuster son indice de réfraction à celui des bactéries. L'objectif principal est de développer une plateforme ergonomique à faible coût, qui puisse fournir en un temps rapide une mesure d'indice de réfraction des cellules / bactériennes avec une meilleure sensibilité et précision par rapport à des mesures obtenues à partir de milieux de cellules en suspension. D'autre part, les cartographies de l'indice de réfraction et les distributions qui en résultent pour les organites intracellulaires, en particulier les gouttelettes lipidiques dans une cellule unique, sont mesurées en recourant à une technique de tomographie par diffraction optique avec imagerie par fluorescence. Un tel système est apte à obtenir la distribution de l'indice de réfraction et la carte de différents organites intracellulaires tels que les mitochondries et le noyau. Les résultats de cette recherche fournissent une connaissance approfondie de la morphologie des gouttelettes lipidiques dans les cellules et leurs réactions face à des stimulants externes notamment lors de l'augmentation de la concentration en acides gras.

Les principales contributions de cette thèse se situent dans trois aspects. La première contribution porte sur la mise au point d'une plateforme microfluidique intégrée de réfractométrie pour les mesures des indices de réfraction effectifs de

trois espèces de bactéries, à savoir *Escherichia coli*, *Shigella flexneri* et *Vibrio cholerae*. Leurs longueurs physiques / géométriques, largeurs et rapports d'aspect ont été également déterminés permettant ainsi d'arriver à une signature spécifique à chaque type de bactérie. L'importance de ce travail de recherche ne réside pas seulement dans l'établissement d'un système rapide, sans marqueur optique et à bas coût pour la détection de bactéries simples dans l'eau potable, mais aussi de fournir une base de données biophysique des dimensions et d'indices de réfraction des espèces de bactéries pour d'autre études exploitant leurs propriétés optiques et morphologiques. Les résultats de la recherche ont été utilisés pour la surveillance de l'eau et des systèmes de détection d'alerte précoce destinés à être utilisés dans l'industrie de la gestion de la qualité de l'eau.

D'autre part, la distribution d'indice de réfraction des gouttelettes lipidiques intercellulaires et leurs réponses envers la stimulation de l'environnement (augmentation de la concentration en acides gras) ont été obtenus en recourant à une technique tomographie de diffraction optique avec imagerie par fluorescence. En établissant cette corrélation, l'augmentation de la concentration d'acides gras peut être déterminée de façon indirecte en mesurant l'indice de réfraction des gouttelettes lipidiques intracellulaires. A la connaissance de l'auteur, une telle étude biophysique n'a jamais été menée auparavant. Ces méthodes d'investigation sont prêtes pour l'étude approfondie basées sur la mesure de distributions en 3D de l'indice de réfraction de nombreux autres micro-organismes et des organites

intracellulaires correspondants. L'introduction de la dimension temporelle ouvre également la voie vers de nouvelles approches de l'étude du métabolisme cellulaire.

Troisièmement, l'étude approfondie des méthodes de mesure de l'indice de réfraction et les résultats liés à sa corrélation avec les comportements biologiques et biomédicales de diverses lignées cellulaires et de cellules dysfonctionnelles ont été explorées à des fins de diagnostic de pathologies et différentes autres applications.

Chapitre 2 Etat de l'Art

Dans ce chapitre, des informations de base relatives à ce projet de thèse sont examinées et la littérature établissant un lien entre les indices de réfraction des micro-organismes et certains agents pathogènes est également examinée. Le chapitre se compose de trois parties. La section 2.1 présente différents modèles d'indice de réfraction des cellules qui ont été proposés et l'importance et la signification de l'indice de réfraction pour la biologie cellulaire et pour le diagnostic. Plusieurs modèles sont développés, tels que l'indice de réfraction moyen d'une population de cellules dans un milieu, l'indice de réfraction effectif de Barer d'une seule cellule, ainsi que le modèle plus avancé, du profil et distribution de l'indice de réfraction d'une seule cellule. Sur la base de ces modèles, d'autres aspects de la cellule et la façon dont l'indice de réfraction est en relation avec la

fonction des cellules ainsi que le développement de pathologies sont étudiés, y compris des études biologiques, des études sur des maladies telles que la malaria, le cancer et les infections.

La section 2.2 décrit plusieurs systèmes de microscopie optique spécialisés qui ont été développés pour mesurer l'indice de réfraction de cellules. De tels systèmes sont basés sur la diffusion de la lumière, de l'interférométrie, les cavités résonnantes optiques, les systèmes holographiques numériques, les systèmes différentiels de phase numérique et les systèmes tomographiques holographiques. La section 2.3 présente brièvement les systèmes optofluidiques, résultant de la combinaison d'une plate-forme micro-fluidique avec un dispositif optique pour la détection. Les systèmes optofluidiques fournissent des méthodes robustes pour la manipulation à haut débit, de cellules dans un milieu de culture, au sein de plates-formes microfluidiques compactes ; ils permettent la détection d'une cellule unique en un temps rapide et sans procédures laborieuses. Ces systèmes servent en tant que plate-forme pour la culture cellulaire, le traitement des cellules, la lyse des cellules et des analyses cellulaires. L'intégration des techniques d'imagerie optique de pointe dans la plate-forme microfluidique simplifie les études dynamiques de cellules cultivées. Avec les avancées actuelles rapides de la recherche en matière de systèmes optiques et microfluidique intégrés, les systèmes de type Laboratoire-Sure-Puce '*Lab-On-Chip*' seront intensivement mis en œuvre pour développer des

systèmes de détection optique portable à faible coût pour de nombreuses applications détection / surveillance bio-chimique et de diagnostic biomédical.

Chapitre 3 Réfractomètre à Immersion Microfluidique

Ce chapitre présente un réfractomètre microfluidique à immersion pour la mesure de paramètres biophysiques (taille, forme et indice de réfraction) de bactéries isolées dans l'eau.

La section 3.1 présente les principes de l'imagerie par contraste de phase et de la réfractométrie par immersion. Le système optique utilisé dans la plate-forme optofluidique est la microscopie à contraste de phase. C'est de la microscopie sans marqueur optique, exploitant l'amélioration de contraste basée sur une technique d'interférences, en modifiant l'onde optique pour augmenter le contraste entre les échantillons transparents (cellules vivantes, par exemple) et l'arrière-plan, par le biais d'une augmentation de la différence de phase entre la lumière transmise (fond) et la lumière diffractée (échantillon). Cette méthode génère la différence de phase entre la lumière transmise à partir de l'arrière-plan et la lumière diffractée par l'échantillon biologique, et convertit les différences de longueur de chemin optique en des différences d'amplitude de l'image. Grâce à la superposition interférométrique des deux faisceaux lumineux, la distribution de phase est

visualisée sous la forme d'une distribution d'intensité, qui peut être détectée par des yeux humains et capturés par tous types de détecteurs optiques.

La réfractométrie par immersion peut ensuite être utilisée, en guise de méthode d'appairage, pour mesurer l'indice de réfraction effectif d'une seule bactérie par immersion dans un milieu liquide tout en observant le contraste optique entre la bactérie et le milieu liquide au fur et à mesure que son indice de réfraction est ajusté (en effectuant un mélange). Dès que le milieu liquide externe possède un indice de réfraction identique à celui de la bactérie ($n_{bac} = n_{med}$), la bactérie semble être invisible. Par conséquent, cette méthode dite de zéro peut être utilisée pour mesurer l'indice de réfraction de la bactérie. Cependant, il y a des limites de la réfractométrie d'immersion conventionnelle du fait de la difficulté d'assurer un contrôle précis de la modulation de l'indice de réfraction du milieu, d'une part, et la difficulté de piégeage sans-contact de la cellule ce qui se traduit par des l'artefacts de bruit et des difficultés à incorporer d'autres techniques biologiques dans l'expérience. Ce sont ces difficultés qui ont motivé le développement d'une plate-forme microfluidique basée sur la réfractométrie par immersion avec les capacités accrues de manipulation des cellules et le mélange liquide du milieu ambiant.

La section 3.2 traite de la conception du réfractomètre par immersion microfluidique, qui est constitué d'une chambre de piégeage de bactérie et d'un

micro-mélangeur pour assurer un contrôle efficace de l'indice du milieu grâce à un mélange de deux liquides. Les échantillons bactériens sont injectés dans le micro-canal et piégés dans la zone de capture d'échantillon au sein de la chambre de piégeage qui comprend un réseau de plusieurs sites de piégeage. Quant à la zone de micro-mélange chaotique des deux liquides, elle est composée d'un motif en zigzag sur trois niveaux pour assurer un bon mélange. La section 3.3 inclut le processus de fabrication de la puce microfluidique à base de PDMS. Cette section traite également de l'installation expérimentale, le protocole de culture des bactéries et les processus de préparation des échantillons.

Dans la section 3.4, les résultats expérimentaux sont présentés, de l'efficacité du micro-mélangeur et les paramètres biophysiques des trois espèces de bactéries différentes. L'efficacité de mélange du mélangeur chaotique est démontrée par l'injection d'eau déminéralisée et la solution de *Ficoll* pré-mélangée avec de la fluorescéine et en surveillant l'intensité de fluorescence en sortie du mélangeur chaotique. Le profil d'intensité de fluorescence a montré que les liquides ont été bien mélangés avec des variations < 1%. Trois espèces différentes de bactéries ont été étudiées, à savoir *E. coli*, *Shigella flexneri* et *Vibrio cholerae*. Aussi bien *E. coli* que *Shigella flexneri* ont une morphologie similaire par laquelle ils sont des bactéries en forme de tige. Sur la base des résultats expérimentaux, *E. coli* a une longueur et une largeur moyenne de 2,83 µm et 0,86 µm, respectivement, et un rapport d'aspect moyen de 3,87. D'autre part, *Shigella flexneri* a une longueur

et une largeur moyenne de 2,74 µm et 0,77 µm, respectivement, et un rapport d'aspect moyen de 3,48. *Vibrio cholerae* est modérément plus petite par rapport aux deux autres bactéries et a une forme de virgule. *Vibrio cholerae* a une longueur moyenne et une largeur de 1,21 µm et 0,43 µm, respectivement, et un rapport d'aspect moyen de 2,84.

L'indice de réfraction du dispositif microfluidique en PDMS est mesuré avec la valeur de 1,412. L'indice de réfraction effectif d'une seule bactérie est mesuré en le comparant à celui de l'indice de réfraction du milieu extérieur, en faisant varier ce dernier au moyen du micro-mélangeur en ajoutant de l'eau déminéralisée à la solution de *Ficoll*, jusqu'à ce qu'à l'obtention d'un ajustage avec l'indice de réfraction effectif de la bactérie. L'indice de réfraction effectif d'une seule bactérie *E. coli* est mesuré à 1,388, tandis que la bactérie *Shigella flexneri* a un indice de réfraction plus élevé, de 1,422. La bactérie *Vibrio cholerae* a l'indice de réfraction efficace le plus faible parmi les trois bactéries et dont la valeur est de 1.365. Il est à souligner que ces valeurs d'indices ont été obtenues par des statistiques issues de mesures effectuées sur un grand nombre de bactéries.

Enfin, la section 3.5 conclut le chapitre avec des perspectives pour la plate-forme de réfractométrie par immersion microfluidique dans le réseau de surveillance de l'eau. Avec la connaissance des paramètres de la taille et la forme de bactéries ainsi que leurs indices de réfraction effectifs, la signature biophysique

de chaque espèce de bactérie a été générée. Cette information permet la détection et la reconnaissance rapide des bactéries nocives dans l'eau potable échantillon d'eau. Ces informations peuvent également servir de base de référence / données pour les différentes techniques de détection de bactéries pour la détection des bactéries d'origine hydrique, telles que la technique de reconnaissance de motif de diffraction optique.

Chapitre 4 Cartographie de l'indice de réfraction d'une cellule unique et de gouttelettes lipidiques par Tomographie à Diffraction Optique

Ce chapitre présente le principe, la méthodologie et les résultats de la cartographie / distribution de l'indice de réfraction au sein d'une cellule unique mesure obtenus par une technique tomographie par diffraction optique associée à l'imagerie de fluorescence. La section 4.1 présente les principes de l'interférométrie de Mach-Zehnder, de l'interférométrie à décalage de phase et de la tomographie à diffraction optique. L'interférométrie de Mach-Zehnder est un concept simple mais très important communément adapté pour différents capteurs et appareils de diagnostic utilisés en photonique, en optique intégrée et dans des applications biochimiques. La capacité d'un contrôle aisé des fonctions et de la différence de phase de la

lumière dans le canal de référence, sans perturber la lumière dans le canal de l'objet, fait de l'interférométrie Mach-Zehnder une configuration populaire en interférométrie holographique, qui nécessite l'ajout d'un module de décalage de phase dans le faisceau de référence. L'interférométrie à décalage de phase se réfère à une technique optique pour laquelle deux faisceaux d'ondes se superposent pour créer une série d'interférogrammes, tout en appliquant un décalage de phase variable entre ces deux faisceaux d'ondes. La distribution de phase du front d'onde est codée sur la variation de l'éclairement énergétique (ou irradiance), tandis que la différence de phase du front d'onde entre les deux faisceaux d'interférence peut être obtenue en analysant l'irradiance point-par-point sur au moins trois interférogrammes correspondants à des états différents de la différence de phase décalée.

La section 4.2 présente brièvement la biologie afférant aux gouttelettes lipidiques intracellulaires ainsi que les techniques conventionnelles utilisées pour l'étude de ces gouttelettes lipidiques. La structure et les fonctions des gouttelettes lipidiques sont d'abord présentées. Les gouttelettes lipidiques se composent principalement d'esters lipidiques et sa surface est revêtue d'une monocouche phospholipidique. La structure lipidique des gouttelettes se distingue par rapport à d'autres organites cellulaires, par exemple le fait qu'elle soit entourée par une monocouche de phospholipides, qui possèdent à la fois des éléments hydrophobes et hydrophiles, et des protéines. Le foie est l'organe qui a le plus grand volume pour stocker des

lipides sous forme de gouttelettes lipidiques. Un autre organe qui stocke des gouttelettes lipidiques est l'intestin grêle. Le muscle squelettique est également impliqué dans le métabolisme oxydatif et comprend une grande quantité de mitochondries et de gouttelettes lipidiques. Les gouttelettes lipidiques jouent un rôle important pour la production des phospholipides et du cholestérol, le métabolisme et la création de stéroïdes. Ils sont les éléments fondamentaux des membranes cellulaires et une source qui fournit de l'énergie. Il est crucial de parvenir à un équilibre dans le maintien de la disponibilité de gouttelettes lipidiques stockés dans les cellules et les exigences de l'activité de l'énergie métabolique parce que la capacité de stockage des lipides excessive conduira à des maladies telles que l'obésité, le diabète de type II, la stéatohépatite et les maladies coronariennes. Par conséquent, il est important dans la recherche d''étudier les mécanismes impliquant ces gouttelettes lipidiques et comment ils contribuent aux maladies, ce qui permet une meilleure compréhension et peut-être envisager des façons de traiter ces maladies.

La section 4.3 traite de la conception du système de tomographie par diffraction optique intégré avec imagerie par fluorescence et son principe de fonctionnement pour obtenir une carte de l'indice de réfraction d'une seule cellule. Un système optique tomographique d'interférence à chemin commun (*common-path interferometry*) est construit, qui est basé sur une imagerie à déphasage unique

mais à des angles d'éclairage variables pour reconstruire la carte d'indice de réfraction d'une seule cellule.

Dans la section 4.4, nous présentons la préparation expérimentale, la caractérisation du système, des mesures des organites intracellulaires et les résultats de mesure des gouttelettes lipidiques dans des cellules 3T3-L1 sous stimulation chimique. En utilisant le système tomographique optique, les indices de réfraction de la mitochondrie, du noyau et des gouttelettes lipidiques sont mesurés, ce qui est validée à l'aide de colorants fluorescents correspondants, à savoir le MitoTracker Green, le SyBr Green et le BODIPY, respectivement. La mitochondrie est mesurée avec une valeur d'indice de réfraction dans la gamme de 1,354 à 1,368. Le noyau a un indice de réfraction de 1,358 ± 0,007, tandis que le noyau a un indice de réfraction de 1,373 ± 0,009. Les gouttelettes lipidiques ont un indice de réfraction de 1,420.

En outre, l'indice de réfraction des gouttelettes lipidiques sous stimulation chimique, à savoir l'addition de différentes concentrations d'acide oléique dans la culture de cellules 3T3-L1, a été également étudiée. Lorsqu'on ajoute 0,5 mM d'acide oléique à la culture, l'indice de réfraction moyen des gouttelettes lipidiques est de 1,439 (mesuré sur un échantillon de 512 unités). Lorsqu'on ajoute 1,0 mM d'acide oléique à la culture, l'indice de réfraction moyen des gouttelettes lipidiques est augmenté à 1,444. Lorsque la concentration en acide oléique de la culture passe

à 2,0 mM, l'indice de réfraction augmente à 1,460. Ces résultats montrent que la composition des gouttelettes lipidiques est modifiée sous cette stimulation d'acide oléique dilué dans le milieu de culture ; ceci est en effet validé par l'augmentation de la valeur d'indice de réfraction des gouttelettes lipidiques. Enfin, la section 4.5 conclut le chapitre avec des perspectives d'applications futures pour la tomographie par diffraction optique dans les études biologiques et biomédicales.

Chapitre 5 Conclusion and Recommandations

Ce chapitre fournit les conclusions de cette thèse ainsi que diverses recommandations pour les travaux futurs. Dans la section 5.1, nous commençons par présenter une conclusion des travaux de recherche que nous avons menés. Dans notre recherche, deux approches différentes ont été étudiées avec les démonstrations expérimentales correspondantes. Une première approche est le développement d'un réfractomètre par immersion microfluidique, intégré pour mesurer les paramètres biophysiques (taille, forme géométrique et indice de réfraction) de trois espèces de bactéries, à savoir *Escherichia coli*, *Shigella flexneri* et *Vibrio cholera*. Le dispositif microfluidique multifonctionnel a été réalisé avec une technologie de lithographie douce en utilisant le PDMS comme matériau de base. Conjointement avec un microscope à contraste de phase, les indices de réfraction effectifs de ces trois espèces de bactéries ont pu être mesurés. L'importance de ce travail de recherche ne réside pas seulement dans

l'établissement d'un système rapide, sans marqueur optique et à faible coût pour la détection de bactéries simples dans l'eau potable, mais c'est aussi un moyen d'alimenter une base de données des dimensions et des indices de réfraction des espèces de bactéries pour la communauté de chercheurs intéressés par ces paramètres biophysiques des bactéries. Les résultats de la recherche ont été utilisés pour la surveillance de l'eau et des systèmes d'alerte et de détection précoce de contamination bactérienne.

L'autre approche consiste en une étude expérimentale de la distribution de l'indice de réfraction dans les gouttelettes lipidiques intracellulaires et leurs réponses à une stimulation de l'environnement de culture cellulaire, en l'occurrence par l'augmentation de la concentration en acides gras. Les mesures ont été effectuées en utilisant une technique de tomographie de diffraction optique avec imagerie par fluorescence. En établissant ce lien de corrélation, des acides gras à différentes concentrations ont été rajoutés au milieu de culture, ce qui modifie l'environnement cellulaire. L'imagerie interférométrique a été effectuée 20 heures après l'addition des acides gras. A la connaissance de l'auteur, une telle étude biophysique n'a jamais été menée auparavant. Ces méthodes d'investigation sont prêtes pour l'étude approfondie basées sur la mesure de distributions en 3D de l'indice de réfraction de nombreux autres micro-organismes et des organites intracellulaires correspondants. L'introduction de la dimension temporelle ouvre également la voie vers de nouvelles approches de l'étude du métabolisme cellulaire.

L'étude approfondie des méthodes de mesure de l'indice de réfraction et les résultats liés à sa corrélation avec les comportements biologiques et biomédicaux de diverses lignées cellulaires et de cellules dysfonctionnelles ont été explorés en vue de l'établissement de diagnostics de différentes pathologies ainsi que pour d'autres applications.

Dans la section 5.2, nous formulons plusieurs recommandations pour les travaux futurs qui peuvent être développés sur la base des résultats de la présente thèse. Tout d'abord, pour la réfractométrie en immersion microfluidique, plus de recherche peuvent être effectuées sur les aspects suivants:

- Augmenter la vitesse de mesure en mettant à niveau le capteur CCD d'enregistrement et l'établissement d'un logiciel de reconnaissance de forme pour capturer l'image et/ou le contraste entre la bactérie / cellule et le milieu liquide d'immersion devient le plus petit, même lorsque la bactérie est en écoulement et instable.
- Concevoir et construire un tube simplifié ou un microscope à contraste de phase portable pour réaliser la fonction de contraste de phase afin de réduire davantage les coûts et augmenter la portabilité.
- Elargir la base de données biophysiques en mesurant les paramètres biophysiques d'autres espèces de bactéries.

- Appliquer la réfractométrie par immersion microfluidique à d'autres échantillons biologiques pour exploiter l'indice de réfraction pour d'autres études biologiques et biomédicales, notamment en hématologie.

Pour ce qui est de la méthodologie relative à la mesure de la distribution 3D de l'indice de réfraction au sein d'une cellule, des recherches plus approfondies peuvent être menées sur les aspects suivants:

- Augmenter la sensibilité et la précision en réduisant le bruit et l'instabilité des erreurs des miroirs de balayage et l'actioinneur PZT, en réduisant le bruit thermique de la caméra CCD en utilisant un CCD refroidi, et le bruit induit par le speckle du laser.

- Augmenter la vitesse de capture en utilisant une caméra à vitesse plus élevée.

- Augmenter la vitesse de reconstruction des images de phase 2D et des distributions d'indice de réfraction 3D en utilisant un circuit FPGA programmable et une carte électronique intégrant un traitement d'image parallèle.

- L'étude quantitative de la distribution 3D de l'indice de réfraction de gouttelettes lipidiques intracellulaires ainsi que leurs variations sous l'effet de différentes stimulations environnementales n'est ici que le début d'un travail dans cette direction. La mesure et le suivi des travaux plus détaillés peuvent être menés en vue de démêler les rôles complexes des gouttelettes lipidiques dans les

processus de métabolisme et de pathologies, et la corrélation possible entre la composition des gouttelettes lipidiques et l'obésité. Par exemple, des recherches plus approfondies sur les cellules dysfonctionnelles des individus obèses et les patients atteints de stéatose hépatique peuvent donner plus de connaissances en vue de la compréhension des changements d'indice de réfraction entre une cellule lipidique normal de gouttelettes en comparaison avec la cellule malsaine.

En général, avec une grande variété d'espèces et la complicité des micro-organismes, il y aura beaucoup de travaux de recherche possibles de nature très significative en lien avec la mesures à plein champ et en 3D de la cartographie cellulaire de l'indice de réfraction, travaux qui pourraient être lancés à partir de l'étude de la littérature et de la méthodologie expérimentale présentés dans cette thèse.

Summary

Refractive index is one of the most important physical parameters governing the light-reaction behaviors of cells and other microorganisms. Its significance lies in the fact that it can be used to determine or correlate with other important biophysical parameters such as dry mass, wet mass, elasticity and used to study dynamic cell activities. The main objective of this research is to study and measure refractive indices of single bacterium and cell as well as cell's response to microenvironment stimulations.

The experimental study includes two approaches. One approach is the development of an integrated microfluidic immersion refractometer platform to measure the biophysical parameters (the size, shape and refractive index) of three bacteria species, namely *Echerichia coli, Shigella flexneri* and *Vibrio cholera*. These parameters could provide biophysical signatures of the targeted bacteria. The significance of this research work lies in establishing a rapid, label-free and low-cost system for detection of minute amount of harmful waterborne bacteria in drinking water.

The other experimental approach is to obtain the 3D refractive index mapping of a single cell with the focus on studying intracellular lipid droplets and their response towards microenvironmental stimulation using an optical diffraction tomographic system integrated with fluorescence imaging. The investigation of refractive indices of cellular lipid droplets initiates a novel approach for deeper understanding of lipid droplets and their critical roles in metabolism and related diseases.

Résumé

L'indice de réfraction est l'un des paramètres physiques les plus importants qui régissent les comportements à la lumière de cellules et d'autres micro-organismes. Son importance réside dans le fait qu'il peut être utilisé pour déterminer ou mettre en corrélation avec d'autres paramètres biophysiques importants de la cellule tels que la masse sèche, la masse humide, l'élasticité et est utilisé pour étudier les activités dynamiques cellulaires. L'objectif principal de cette recherche est d'étudier et de mesurer les indices de réfraction de bactérie et de cellules unitaires ainsi que leur réponse à des stimulations micro-environnementales.

Notre étude expérimentale comprend deux approches. La première consiste en une plate-forme microfluidique intégrée de réfractométrie par immersion pour mesurer les paramètres biophysiques (taille, forme et indice de réfraction) de trois espèces de bactéries, à savoir *Escherichia coli*, *Shigella flexneri* et *Vibrio cholerae*. Ces paramètres peuvent fournir des signatures biophysiques des bactéries ciblées. L'importance de ce travail de recherche réside dans l'établissement d'un système rapide, sans label fluorescent et à bas coût pour la détection d'une quantité infime de bactéries nocives dans l'eau potable.

L'autre approche consiste à obtenir la distribution de l'indice de réfraction au sein d'une seule cellule avec l'accent mis sur l'étude des gouttelettes lipidiques intracellulaires ainsi que leur réponse à une stimulation micro-environnementale. A cet effet, nous avons recouru à un système de diffraction tomographique optique intégré avec imagerie par fluorescence. Ce type d'étude sur l'indice de réfraction de gouttelettes lipidiques cellulaires initie une nouvelle approche pour une meilleure compréhension des gouttelettes lipidiques et leurs rôles essentiels dans le métabolisme cellulaire.